

AD-A100 979

CALIFORNIA UNIV LOS ANGELES DEPT OF PHYSICS  
CHARACTERIZATION OF INFRARED OPTICAL PROPERTIES OF TRANSPARENT —ETC(U)

MAY 81 R BRAUNSTEIN  
AFOSR-78-3665

F/6 20/6

NL

UNCLASSIFIED

1 OF 2  
AD A  
00979

AFOSR-TR-81-0545



AEOSR-TR- 81-0545 UCLA

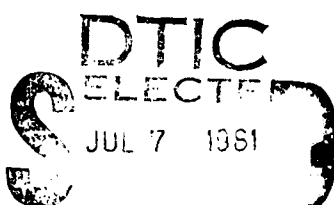
• Department of Physics •

29



ADA100979

DMG FILE COPY



LOS ANGELES 90024  
CALIFORNIA

Approved for public release;  
distribution unlimited.

81706005

SECURITY CLASSIFICATION OF THIS PAGE (When Data Entered)

REPORT DOCUMENTATION PAGE		READ INSTRUCTIONS BEFORE COMPLETING FORM
1. REPORT NUMBER	2. GOVT ACCESSION NO.	3. RECIPIENT'S CATALOG NUMBER
AFOSR-TR- 81 -0545 AD-A100 979		
4. TITLE (and Subtitle)	5. TYPE OF REPORT & PERIOD COVERED INTERIM 1/1/80 - 3/31/81	
Characterization of Infrared Optical Properties of Transparent Materials		6. PERFORMING ORG. REPORT NUMBER
AUTHOR(s)	7. CONTRACT OR GRANT NUMBER(s) AFOSR 78-3665	
8. PERFORMING ORGANIZATION NAME AND ADDRESS Department of Physics University of California Los Angeles, California 90024	10. PROGRAM ELEMENT, PROJECT, TASK AREA & WORK UNIT NUMBERS 61102F 2306/C2	
9. CONTROLLING OFFICE NAME AND ADDRESS Air Force Office of Scientific Research Bolling Air Force Base, D. C. 20332	12. REPORT DATE 5/15/81	
14. MONITORING AGENCY NAME & ADDRESS (if different from Controlling Office)	13. NUMBER OF PAGES 134	
15. SECURITY CLASS. (of this report) Unclassified		
15a. DECLASSIFICATION/DOWNGRADING SCHEDULE		
16. DISTRIBUTION STATEMENT (of this Report) APPROVED FOR PUBLIC RELEASE; DISTRIBUTION UNLIMITED		
17. DISTRIBUTION STATEMENT (of the abstract entered in Block 20, if different from Report)		
18. SUPPLEMENTARY NOTES		
19. KEY WORDS (Continue on reverse side if necessary and identify by block number) Infrared Wavelength Modulation      CaF <sub>2</sub> ; LiF; NaCl; NaF; LaF <sub>3</sub> ; BaF <sub>2</sub> ; Absorption in Highly Transparent Solid      MgF <sub>2</sub> ; SrF <sub>2</sub> ; MgO, GaAs, Si, HgCd Te Rayleigh-Brillouin Scattering Fluoride Glasses      Laser Windows, Semiconductors		
20. ABSTRACT (Continue on reverse side if necessary and identify by block number) The spectral distribution of the absorption in the spectral region from 0.5-12μm was measured by infrared wavelength modulation technique on: CaF <sub>2</sub> ; LiF; NaCl; NaF; LaF <sub>3</sub> ; BaF <sub>2</sub> ; MgF <sub>2</sub> ; SrF <sub>2</sub> ; MgO. Both surface and volume contaminants were identified. Rayleigh-Brillouin scattering was measured on single and polycrystalline KCl. In addition, Rayleigh-Brillouin and Raman measurements were performed on fluoride glasses.		
(Continued on reverse side)		

UNCLASSIFIED

SECURITY CLASSIFICATION OF THIS PAGE (When Data Entered)

(20. (Cont'd)

Infrared optical derivative spectroscopy was employed to determine:  
Stress in Si on sapphire, strain in ion implanted GaAs, free carrier  
screening of hyperbolic excitons in GaAs, deep levels in Si and GaAs and vibra-  
tional modes in oxides of Si, GaAs and HgCdTe.

UNCLASSIFIED

SECURITY CLASSIFICATION OF THIS PAGE (When Data Entered)

AIR FORCE OFFICE OF SCIENTIFIC RESEARCH (AFSC)  
NOTICE OF TRANSMITTAL TO DDC  
This technical report has been reviewed and is  
approved for public release IAW AFR 190-12 (7D).  
Distribution is unlimited.  
M. D. BLOSE  
Technical Information Officer

Characterization of Infrared Optical  
Properties of Transparent Materials.

Contract: AFOSR-78-3665

1 Interim Technical Report for Period:

2 January 1980 - March 31, 1981

Submitted to:

Air Force Office of Scientific Research  
Bolling Air Force Base, D. C. 20332

Prepared by:

Rubin Braunstein  
University of California, Los Angeles

### Research Objectives

The broad objectives of this program are to further our understanding of the intrinsic and extrinsic properties of highly transparent solids in the infrared region of the spectrum. The identification of chemical and structural imperfections which occur in highly transparent insulators and semiconductors are investigated by the following experimental techniques: infrared optical derivative and light scattering techniques. The experimental results are used to develop theoretical models for the intrinsic and extrinsic interactions.

### Status Report Summary

The previous informal technical report covered the period 1 January 1980 to 31 August 1980. Since this interim report covers the period 1 January 1980 to 31 March 1981, some aspects of the former report are included for the purposes of continuity.

Our unique infrared wavelength modulated spectrometer is capable of detecting a change in absorption or reflection of a part in  $10^5$  on a relatively smooth background in the spectral region from 0.2-2-20  $\mu\text{ms}$ . With this instrumentation we have for the first time measured the continuous spectral distribution of the absorption in highly transparent solids at levels of  $10^{-5} \text{ cm}^{-1}$ . A detailed study has been completed on:  $\text{KC}\ddot{\text{o}}$ ,  $\text{KBr}$ ,  $\text{CaF}_2$ ,  $\text{LiF}$ ,  $\text{NaCl}$ ,  $\text{LaF}_3$ ,  $\text{BaF}_3$ ,  $\text{MgF}_2$ ,  $\text{SrF}_2$  and  $\text{MgO}$  in the spectral region 2.5-12.0  $\mu\text{m}$ . Previously, only measurements at discrete wavelengths by thermocouple laser calorimetry and photo-acoustic calorimetry were available. The richness of the absorption structures observed in all these crystals enabled us to identify volume and surface contaminants and allowed the identification of the type of bonding of the particular constituents present. The sensitivity of the infrared modulation systems indicates that it is capable of detecting a fraction of a monolayer surface species.

Stress in chemical vapor deposition layers of Si on sapphire were examined using our derivative spectrometer by measuring the shift and polarization dependence of the 3.4 eV critical point.

Strain in ion implanted GaAs was readily detected by our techniques by observing the shift of the  $\text{L}_{3\gamma} - \text{L}_{1\text{c}}$  critical point.

Free-carrier screening of hyperbolic excitons in GaAs was observed.

Deep levels in Si and GaAs were observed by deep level derivative absorption spectroscopy (DLDAS) with a sensitivity of  $10^{12}$ - $10^{14}$  impurities/cm<sup>3</sup> previously only obtained by electrical transient capacitance techniques (DLTS).

Oxides on the compound semiconductors GaAs and HgCdTe were observed in 700 Å layers using Raman scattering and optical derivative techniques; OH<sup>-</sup> can be observed in the former and TeO<sub>2</sub> in the latter materials. In addition, SiH was observed in 8Å layers of Si.

An initial study of Rayleigh-Brillouin scattering from single and polycrystalline alkali halides was completed indicating that dislocations, grain boundaries and the impurity-pinning at these sites are possible candidates for increased scattering in polycrystalline samples.

A series of infrared transmitting low loss fluoride glasses were prepared using reactive atmosphere processing techniques. In addition, Rayleigh-Brillouin and Raman scattering were performed on these glasses indicated that the HfF<sub>4</sub>-BaF<sub>2</sub>-ThF<sub>4</sub> system scatters more than the ZrF<sub>4</sub>-ThF<sub>4</sub>-BaF<sub>2</sub> system.

The study of surface polaritons on n<sup>+</sup> Silicon and Copper was completed showing that such studies should be conducted in the complex plane when either the damping is large or there exists interband transitions in the spectral region studied.

A multipass tandem Fabry-Perot interferometer was assembled to study surface excitations on semiconductors as well as the largely unexplored region of interface surface phonons between metal-conductor, metal-oxide-semiconductor and heterostructures using Rayleigh-Brillouin lack-scattering.

#### Infrared Wavelength Modulation Spectroscopy of Insulators

The infrared wavelength modulation spectrometer system that we have developed has enabled us to perform unique measurements on highly transparent solids at levels of absorption of  $10^{-5}$  cm. These techniques were previously employed on KBr and KC<sub>2</sub> and have now been extended to other crystalline systems which are of interest in light guiding applications. A detailed study has been completed for CaF<sub>2</sub>, LiF, NaCl, NaF, LaF<sub>3</sub>, BaF<sub>2</sub>, MgF<sub>2</sub>, SrF<sub>2</sub> and MgO. We have measured the continuous spectral distribution of the absorption in these materials in the spectral region from 2.5 to 12.0 μm. Previously, only measurements

at discrete wavelengths by thermocouple laser calorimetry and photo-acoustic calorimetry were available. Rich and varied adsorption structures were observed in all these crystals which enable us to identify volume and surface absorption. It is interesting to note that despite the diverse chemistry of these substances and the varied crystal growth techniques employed in the preparation of these materials, similar dominant bands are observed in most samples which are due to physisorption, volume and surface chemisorption. However, the various fine structures observed in different crystals are indicative of the individual characteristics of the chemistry of the crystal preparation. These measurements which were performed in the laboratory and dry  $N_2$  ambient readily show the physisorption and desorption of surface contaminants and allow the identification of the type of bonding of the particular constituents present. The surface character of some of the absorption at levels of  $10^{-4}$  to  $10^{-5} \text{ cm}^{-1}$  indicates the importance of performing measurements in the same ambient when comparing low level absorption measurements by various sensitive techniques.

The sensitivity of the infrared modulation techniques indicates that a fraction of a monolayer of surface adsorbed species can be detected. Experiments in controlled ambients on well characterized substrates using this technique can be rewarding for the physics and chemistry of surfaces.

This work has been presented at the Laser Damage Symposium, 1980, at Boulder, Colorado. A paper will appear in the NBS Proceedings of this Conference. A copy of the submitted manuscript is enclosed in the Appendix of this report.

The successful use of our infrared optical derivative system in the study of bulk and surface impurities in insulators at levels of  $10^{-5} \text{ cm}^{-1}$  indicates that much remains to be done in the area of laser windows. It is clear that our  $\lambda$ -modulation measurements should be used in conjunction with a systematic study with crystal synthesis groups.

In the latter part of this report period our attention was directed toward the use of our infrared  $\lambda$ -modulation techniques as well as Rayleigh-Brillouin scattering to semiconductor problems. We have demonstrated that  $\lambda$ -modulation can be used to study deep levels in GaAs and silicon at levels of sensitivity formerly only obtainable using DLTS electric measurements. In addition, we have shown that thin surface oxides can be studied by  $\lambda$ -modulation and optical scattering techniques.

### Wavelength Spectroscopy of Semiconductors

In the growth of semiconductors by various epitaxial techniques and the doping by ion implantation, an important technological problem is a means of detecting stress in the growth layers. We have used our wavelength modulation techniques to determine the shift of various band structure critical points as a function of doping. It has been possible to observe the stress in chemical vapor deposition layers (CVD) of Si on sapphire by examining the shift of the 3.4 eV critical point. In addition a polarization dependence of the shift was measured indicating an anisotropic strain exists in 4700 to 1900 Å layers on Si.

Strain in ion implanted GaAs was readily observed by our techniques. The shift in the  $L_3$ - $L_1$  critical point due to various ion implanted species such as Be, Sb, S, In and double implanted Sb + Be were observed; the implanting flux was of the order of  $10^{13}/\text{cm}^2$ . It is surprising that significant structural changes were observed for such low levels of implanting and attests to the sensitivity of our techniques. Compared to unimplanted GaAs, positive and negative shifts of the energy of the critical point indicates that we are able to distinguish contraction and expansion of the lattice. Previous attempts to study strain effects in semiconductors looked for changes in carrier mobility in implanted material proved futile. Since transport measurements involve averages over the distribution of Bloch functions, the local character of strain is not immediately obvious. Since our wavelength modulation reflectivity measurements samples the material within a penetration depth for the radiation, in the present case  $\sim 50\text{\AA}$ , one can "view" local effects of strain on the band structure of the semiconductor.

We have begun studies of the  $E_1$  and  $E_1 + \Delta_1$  critical point in GaAs as a function of doping. Since this van Hove singularity has a hyperbolic exciton associated with it, it is of interest to study the effects of free-charge screening on the final state interaction. This study has shown that the reflectivity as a function of increasing carrier concentration, shows little broadening, but a definite decrease in magnitude. These effects are indicative of screening effects on the hyperbolic exciton. Although there have been many experimental and theoretical studies to search for free-carrier screening on direct and indirect excitons, to our knowledge none have concerned the hyperbolic exciton of this critical point. This is particularly surprising in view of the extensive studies of band structure of semiconductors by electro, piezo, thermo-modulation

techniques. It is planned to continue these studies for n and p-type doped materials. In addition, we plan to develop the theory of screening for this exciton. The study of screening effects for such final state interactions is particularly attractive since one can avoid the ancillary effects of screening such as band tailing or Burstein shifts which can mask screening effects for direct and indirect excitons. Knowledge of screening effects will become increasingly important technologically as very large scale integration of heavily doped devices develops.

#### Deep Level Derivative Absorption Spectroscopy (DLDAS) on GaAs and Si

Our understanding of point defects, such as vacancies and chemical impurities in semiconductors which give rise to substantial rearrangements of electronic density and atomic positions, are not well understood since they are not well described by effective mass or linear response theory. In recent years the emergence of transient capacitance techniques have stimulated quantitative studies of deep levels and motivated theoretical studies. Despite the immense variation in these junction techniques which differ in technical details, the end results one desires from these measurements, is the optical emission or absorption crosssections for either electrons or holes which are proportional to the absorption coefficient. In general, excited states are not observed in these techniques and thresholds for the transitions to bands are not easily determined. Direct absorption measurements could yield the quantities of interest, but at levels of sensitivity of DLTS techniques, on the order of  $10^{12}$ - $10^{14}/\text{cm}^3$ , they can not be employed. However our optical derivative techniques have the requisite sensitivity. In addition it is not necessary to make electrical contacts to the samples nor are we restricted to specific sample resistivities.

We have performed wavelength derivative measurements on high purity triple zone refined Si and have observed numerous absorption bands between the band edge and the multiphonon tail at levels of  $10^{-4}\text{ cm}^{-1}$ . The identification of these levels have not been definitively made; some of them correspond to Si vacancies and interstitial energies. We plan further measurements on Si as a function of temperature. Aside from the above bulk levels we have also observed an absorption band at 4.4  $\mu\text{m}$  which is present in Si whose strength is

independent of sample thickness. This band seems to be due to an Si-H vibrational band; it is particularly strong when Si is etched with HF, however it is present regardless of the surface preparation employed.

The properties of high resistivity GaAs continues to be of technological importance since it is a substrate or buffer layer in molecular beam and other vaporous growth techniques. The aim of electrical characterization of insulating materials is to determine the concentration of shallow donor or acceptors to be compensated by deep levels. To this day it is not clear whether Cr or O levels used for compensation give rise to multiple levels or exist as clusters.

We have initiated studies by optical derivative techniques to study semi-insulating GaAs. In Cr:GaAs samples 20 mils thick, we have easily resolved a number of absorption bands between 0.8 and 1.1 eV. In addition, absorption bands were observed in undoped crystals with absorption coefficients at levels of  $10^{-2} \text{ cm}^{-1}$ . Most previous studies of such material have only been studied by OTSC techniques (optical thermally stimulated currents). We have initiated such electrical studies in conjunction with our optical derivative techniques. Simultaneous studies using optical and thermal stimulation can be profitable since each yield slightly different physical parameters for the deep levels.

In addition, we have initiated high resolution Fourier-transform photoconductivity measurements to look for the sample differences in the hydrogen-like spectra of shallow donor or acceptor species in MBE prepared layers.

The tripartite approach on the same sample will give a global assessment of semi-insulating GaAs. The purpose of such an assessment is to determine the residual concentration of shallow levels  $N_D - N_A$  and the concentration of compensating deep levels.

#### Raman Scattering and Optical Derivative Measurements of Oxides on HgCdTe, GaAs and Si

The oxides that are formed on compound semiconductors are of fundamental and technological interest. The sites of chemisorption on these materials have been a matter of discussion for some time. The successful fabrication of MOS type devices as well as the stabilization of surface states depends upon the preparation of appropriate oxides. The chemical, physical and electrical pro-

erties of oxides on GaAs and HgCdTe are not sufficiently understood or controlled. The use of microprobe, Auger and other commonly used surface analysis methods yield only atomic abundance. However, Raman spectroscopy can provide direct information on the composition and structure of surface oxides.

We have performed Raman measurements on a sample of 700  $\text{\AA}$  oxide grown on HgCdTe obtained from the Santa Barbara Research Center. In this work a number of bands were observed in the region 100 to 400  $\text{cm}^{-1}$ . To identify these oxides, a series of Raman experiments were performed on crystalline  $\text{CdO}$  and  $\text{TeO}_2$  since there is a paucity of literature of the modes of these oxides which are suspected to occur on HgCdTe surfaces. This work has allowed us to deconvolute some of the structures observed in the 700  $\text{\AA}$  layer. The dominant bands observed in these oxides seem to be due to oxygen bound to Te-sites. We have also been able to observe infrared active bands in these oxides using infrared derivative techniques.

In examining the oxides grown on GaAs substrates, it has been possible to detect  $\text{OH}^-$  modes in 0.5  $\mu\text{m}$  layers. We have previously shown, using our infrared modulation system to study the 9.0  $\mu\text{m}$   $\text{SiO}$  vibrational band in 8  $\text{\AA}$  layers of "nascent" oxide on Si form in normal laboratory ambient. In these experiments, Si substrates were etched with HF and the growth of the oxide was monitored by observing the growth of the 9.0  $\mu\text{m}$  band. As we have previously indicated in this report, we also observed strong  $\text{SiH}$  bands when HF etch was used as well as when other surface preparations were employed.

It is clear that since our methods can detect a fraction of a monolayer of oxide, if we were to perform such experiments in UHV we could answer the vexing question involved in the passivation of GaAs surfaces as to what is the initial site of oxidation on GaAs. By observing whether  $\text{Ga}_2\text{O}_3$  or  $\text{As}_2\text{O}_3$  bands are initially formed in UHV oxidation, an important contribution to this field can be made. We have given some consideration to performing such UHV optical experiments. The major components of UHV pumping and dewar system have been assembled. However some auxilliary equipment such as a quadrupole mass-spectrometer is not available to complete such a system.

### Rayleigh-Brillouin Scattering

We have assembled a high contrast ratio five-pass Fabry-Perot interferometer. In addition, a tandem Brillouin spectrometer has been assembled for the extended free spectral range up to  $100 \text{ cm}^{-1}$  to study low frequency modes in highly transparent solids. The systems are under computer control using a CAMAC interface. Aside from studying inelastic Brillouin and Raman regimes using the interferometer, the electronic system enables us to also study quasi-elastic (Rayleigh) scattering by digital-photon counting and self-beating techniques.

Current technological interests continue to motivate a search for candidate materials which exhibit low optical losses at specific wavelengths for utilization in fiber optic and other light guiding applications. Considerations have been given to the ultimate theoretical intrinsic-loss mechanisms and the practical extrinsic losses due to impurities and imperfections in crystals and glassy materials. The ultimate transparency of a material should lie in a valley between the intrinsic electronic absorption edge and the tail of the multiphonon transitions. In this spectral region, the ultimate losses should be due to Rayleigh and Brillouin scattering. The Brillouin scattering results from acoustical phonons and is an intrinsic property of a given material. The Rayleigh scattering of light results from nonpropagating fluctuations in the dielectric constant. These fluctuations can result from frozen-in random variations in the dielectric constant of a disordered solid as well as fluctuations resulting from local variations in strain in crystalline solids; such extrinsic scattering will vary from sample to sample; however entropy fluctuations which are intrinsic properties can still contribute to the Rayleigh scattering.

Using our Rayleigh-Brillouin scattering system, we have completed an initial study of scattering from single and polycrystalline materials in cooperation with a group at the Hughes Research Laboratory, to probe the scattering mechanisms in highly transparent solids. We have found that polycrystalline materials scatter more strongly than single crystal materials. However, we have not as yet explicitly associated a particular elastic scattering process which contributes to the total scattering. Grain boundaries, dislocations and the decoration of these structures by impurity-pinning are possible candidates. In addition, our results indicate that even in pure single crystal KCl samples, there is more scattering than predicted for an ideal crystal.

A paper entitled: "Scattering Losses in Single and Polycrystalline Materials for Infrared Fiber Applications" is to be published in the volume entitled "The Physics of Optical Fibers, 1980" as the Proceedings of the Am. Ceramic Society Annual Meeting, Chicago, April 1980. A copy of this manuscript is enclosed in the Appendix.

#### Fluoride Glasses

The search for materials which exhibit low optical losses has been directed progressively to larger wavelength for the following criterion. Consideration of the various contributions to intrinsic scattering indicate that the minimum optical loss should occur at the intersection of the Rayleigh scattering curve on the high frequency end and at the multiphonon edge at low frequency. Since the Rayleigh scattering losses exhibit a  $\lambda^{-4}$  wavelength dependence, it is clear that it is desirable to operate at longer wavelengths.

It has recently been discovered that it is possible to prepare a series of non-oxide glasses based on a mixture of  $ZrF_4$  and  $HfF_4$  with other metallic fluorides. In the conventional preparation of these glasses residual impurities such as  $OH^-$  and  $O^=$  can contribute extrinsic absorption and scattering centers. Because of our programmatic interest in highly transparent materials, we have turned our attention to the fabrication and optical measurements on these glasses. In collaboration with a group at the Hughes Research Laboratory, glasses consisting solely of high purity  $ZnF_4$ ,  $ThF_4$ , and  $BaF_2$  have been synthesized using reactive atmosphere processing (RAP) techniques. The utilization of RAP in the synthesis of these glasses has shown that infrared transparency and the mechanical strength of these halide glasses are greatly improved by eliminating anionic impurities such as  $OH^-$  and  $O^=$  resulting in glasses which are continuously transparent from 0.3 to 7  $\mu m$  and are water insoluble and unusually strong and hard.

This work has been published in "Infrared-Transparent Glasses Derived from the Fluorides, Thorium and Barium," M. Robinson, R. C. Pastor, R. R. Turk, D. P. Devor, M. Braunstein and R. Braunstein, Mat. Res. Bull. 15, 735 (1980).

### Rayleigh-Brillouin and Raman Scattering in Fluoride Glasses

In order to evaluate the scattering losses in these glasses, Rayleigh-Brillouin and Raman measurements were performed. By measuring the ratio of the intensity of the Rayleigh to Brillouin scattered light - the so-called Landau Placzek ratio, one can obtain the attenuation due to scattering in terms of calculable scattering losses. Such measurements were performed on two glass systems:  $\text{HfF}_4\text{-BaF}_2$  -  $\text{ThF}_4$  and  $\text{ZrF}_4\text{-ThF}_4\text{-BaF}_2$ . Preliminary measurements indicate that the scattering is larger for the  $\text{HfF}_4$  glass than the  $\text{ThF}_4$  glass. Whether this is fundamentally due to the "fictive temperature" of these glasses or is extrinsic, remains to be seen after further measurements on a number of samples are performed.

In addition, Raman scattering measurements were made on these systems as a means of identifying the optical phonons in the glasses compared to the phonons of the pure constituents of the glasses.

### Surface Polaritons

Optical attenuated total internal reflection measurements were performed on the surface polariton of  $n^+$  Silicon and Copper. These investigations enable the optical constants of the materials to be determined in a spectral regime where they are difficult to measure by conventional means and in addition, the dispersion relationship of the surface excitations were obtained. The general dispersion relationship for surface plasmon at an air-solid interface is  $k_{11}^2 = (\omega^2/c^2)(\epsilon(\omega)/(1+\epsilon(\omega)))$  where  $\epsilon(\omega)$  is the complex bulk dielectric function of the solid. In general, there will be two physical solutions to the dispersion relationship that is, one where the frequency is real and  $k_{11}$  complex; and the other where  $\omega$  is complex and  $k_{11}$  real. Up to the present work, there were wide discrepancies between theoretical and observed dispersion curves obtained by attenuated total internal reflection techniques. Previously, investigators had attempted to interpret their data using real values of  $\omega$ . Due to the apparent discrepancies between theoretical predictions and experimental evaluations in the real frequency phase, we examined the surface polariton dispersion relationship for various models in the complex frequency plane. An original method was developed to evaluate the optical constants, dielectric functions

and the Fresnel reflection coefficients by redefining them as functions of complex frequency. By evaluating the attenuated total integral reflection dispersion curves in the complex plane, we were able to obtain agreement between theory and experiment for the materials measured in this work. Before this analyses, it was believed that the backbending observed in some dispersion curves would occur only for complex wavevector solutions of the dispersion relationship. Our analysis comparing the complex- $\omega$  and complex- $k$  solutions of the dispersion relationship showed that the difference between the two calculations is small.

As a consequence of this work, we believe that all studies of surface polaritons should be conducted in the complex frequency plane when either the damping is large or there exists interband transitions in the spectral region studied.

The above work has been completed and the following manuscripts have been submitted for publication:

"Optical Properties of the Surface Plasmon of  $n^+$  Silicon" - P. F. Robusto and R. Braunstein to appear in Phys. Stat. Sol. (b), "Optical Measurements of Surface Plasmons in Copper" - P. F. Robusto and R. Braunstein, to appear in Phys. Stat. Sol. (b).

#### Publications For This Period

"Infrared-Transparent Glasses Derived From the Fluorides of Zirconium, Thorium and Barium," with M. Robinson, R. C. Pastor, R. R. Turk, D. P. Devor and M. Braunstein (Mat. Res. Bull. 15, 735 (1980)).

"Scattering Losses in Single and Polycrystalline Infrared Materials for Infrared Fiber Applications," with J. A. Harrington, M. Braunstein and B. Bobbs (to appear in Proceedings of Am. Ceramic Society Annual Meeting, April 1980, to be published as Volume on Physics of Optical Fibers, 1980).

"Infrared Wavelength Modulation Spectroscopy of Laser Window Materials," with R.K. Kim and M. Braunstein; Laser Damage in Optical Materials; 1980, Oct. 1980, NBS Boulder Co. ed by H. E. Bennett, A. J. Glass and A. H. Guenther to appear in NBS Special Publication.

"Infrared Transparent Glasses Derived from Hafnium Fluoride," with M. Robinson, R. R. Turk, D. P. Devor and M. Braunstein; To appear in Proceedings of Los Angeles Technical Symposium Feb. 9-13, 1981, North Hollywood, California, the Society of Photo-Optical Instrumentation Engineers.

"Optical Measurements of Surface Plasmons in Copper," with P. Robusto to appear in Phys. Stat. Sol. (b)

"Optical Properties of the Surface Plasmon of  $n^+$  Silicon," with P. Robusto to appear in Phys. Stat. Sol. (b).

Personnel Associated with Project

R. Braunstein	Principal Investigator
B. Bobbs	Ph.D. Candidate
M. Burd	Ph.D. Candidate
D. Deal	Ph.D. Candidate
M. Eetemadi	Ph.D. Candidate
R. K. Kim	Ph.D. Candidate

Scientific Interactions

We have continued active relationships with other groups in the field. Liason was maintained with the synthesis groups at the Hughes Research Laboratory regarding the evaluation of alkali halide, alkali earths and halide glasses prepared by reactive processing. The work on  $Hg_{1-x}Cd_xTe$  oxides has benefitted from samples and technological exchanges with the Santa Barbara Research Center. The Si on sapphire and ion implanted samples were obtained from the Industrial Products Division of Hughes at Carlsbad. The work on the fluoride glasses is a cooperative endeavour with the Hughes Research Laboratory. In addition, discussions on this project have been held with B. Bendow of RADC. We have had extensive technical exchanges regarding shallow donor and acceptor levels in molecular beam epitaxial material with C. W. Litton of the Air Force Avionics Laboratory and through an extensive visit by Dr. K. Baja to UCLA. In addition, we have participated in the ARPA review on nucleation of crystal growth and the properties of HgCdTe. We have evolved a detailed program with the Morris Braunstein Molecular Beam Epitaxial group at the Hughes Research Laboratory. This program entails a unified correlation with the Hughes synthesis activity and the UCLA study of shallow and deep levels in MBE layers of GaAs.

**APPENDIX**

## INFRARED WAVELENGTH MODULATION SPECTROSCOPY OF LASER WINDOW MATERIALS\*

Rubin Braunstein, Ryu K. Kim  
Department of Physics  
University of California  
Los Angeles, California 90024

and

Morris Braunstein  
Hughes Research Laboratories  
Malibu, California 90265

We have previously shown that the infrared wavelength modulation system that we have developed is capable of measuring the complete spectral distribution of the extrinsic absorption in highly transparent solids at levels of  $10^{-5} \text{ cm}^{-1}$  in the spectral range from 2.5 to 12 microns [1]. The previous measurement techniques that were employed for KBr and KC2 have been extended to other crystalline systems which are of interest in light guiding applications, namely: CaF<sub>2</sub>, LiF, NaCl, NaF, LaF<sub>3</sub>, BaF<sub>2</sub>, MgF<sub>2</sub>, SrF<sub>2</sub>, and MgO. Rich and varied absorption structures were observed in all of these crystals enabling an identification of volume and surface absorption. Similar dominant bands are observed in many of these substances indicating the presence of common impurities regardless of the crystal and the origin of its growth. However, varied fine structures are observed in different crystals which are indicative of the individual characteristics of the chemistry of the crystal preparation. These measurements were performed in laboratory and dry N<sub>2</sub> ambients and readily show the physisorption and desorption of surface contaminants. In appropriate materials, measurements were extended into the intrinsic multiphonon region.

**Key words:** Extrinsic and intrinsic infrared absorption; volume and surface impurities; infrared wavelength modulation; CaF<sub>2</sub>; LiF; NaCl; NaF; LaF<sub>3</sub>; BaF<sub>2</sub>; MgF<sub>2</sub>; SrF<sub>2</sub>; MgO; laser windows.

### 1. Introduction

The requirements for high power laser and light guiding systems continue to generate a need for extremely low absorption levels in infrared transmitting materials. These interests continue to stimulate efforts at material growth and surface preparation techniques to produce materials that approach intrinsic absorption levels in appropriate spectral regions. In practice, in the highly transparent regions, absorption coefficients are observed to vary greatly from sample to sample indicating the extrinsic nature of the absorption processes. To assess progress in improvements in material preparation, sensitive techniques are required to measure low levels of absorption.

To determine the sources and nature of the extrinsic light absorptions, we have employed the technique of infrared wavelength modulation in the spectral region from 2.5 to 12.0  $\mu\text{m}$ . We have previously employed this technique [1] in a study of KBr and KC2 prepared by different crystal growth techniques and were able to identify possible surface and volume impurities. In the present work, we have extended these studies to survey a number of optical materials commonly used in laser window applications, namely: CaF<sub>2</sub>, LiF, NaCl, NaF, LaF<sub>3</sub>, BaF<sub>2</sub>, MgF<sub>2</sub>, SrF<sub>2</sub>, and MgO. The continuous spectral distribution of the absorption obtainable by wavelength modulation techniques at levels of  $10^{-5} \text{ cm}^{-1}$  facilitates identification of volume and surface absorption centers. Although rich and varied absorption structures are observed in all of these crystals, similar dominant bands are observed in many of these substances indicating the presence of common impurities regardless of the crystal origin and the concomitant growth techniques used to prepare the materials.

### 2. Experimental Techniques

The infrared wavelength modulation spectrometer was previously described [1]. It consists of a system for sweeping the output wavelength of a monochromator across the exit slit by a vibrating output diagonal mirror whose depth of modulation can be continuously controlled. Careful consideration is given to the subtraction of the background of the transfer function of the monochromator which can include atmospheric absorption, the spectral response of the optics as well as the detector. To accomplish this, a sample-in-sample-out procedure is used to obtain the background intensity without the sample, the derivative of this background, the transmitted intensity with the sample present and its derivative. The above operations are performed under microprocessor control. The computation of the energy derivative of the absorption as well as its integration to display absorption peaks are performed on-line using a PDP 11/20 computer. Although the primary data in the form of the energy derivative of the sample absorption is adequate to reveal absorption structures, as an aid for comparison with the conventional literature, the integrated results are reported in this paper.

### 3. Experimental Results and Analysis

The crystals used in this study are indicated in table 1, together with suppliers of the materials. Standard procedures were used to prepare the surfaces of the samples; these consisted of surface grinding, polishing with a slurry of Linde A in ethanol or propanol, and then drying under a heat lamp. Prior to the optical measurements the samples were stored in a vacuum desiccator. The optical measurements were performed with the samples in the laboratory ambient as well as in a dry N<sub>2</sub> atmosphere. The data for the various materials studied are shown in figures 1, 3, 4, 5, 6, 7, 8, 9, 10.

\*Supported by the Air Force Office of Scientific Research.

<sup>1</sup>Figures in brackets indicate literature references at the end of this paper.

The laboratory ambient and dry  $N_2$  atmosphere runs for a given sample are displayed on the same page to facilitate comparison. The absorption coefficients at the upper left hand of the figures are the beginning of the intrinsic multiphonon tails and are shown when they fall within the spectral range of the spectrometer.

When the absorption coefficient is sufficiently high, as in the multiphonon region it is possible to measure the transmission directly as well as its derivative. In this case, it is possible to determine the constant of integration which is necessary to obtain the absolute value of the absorption when integrating derivative data; this constant can be used to calculate the absorption coefficient in the extrinsic region well below the multiphonon tail. The constant of integration can also be obtained from a laser calorimetric measurement at a given frequency. The integration is performed by a standard trapezoidal integration; in this computation the depth of modulation, which in the present work is  $10 \text{ cm}^{-1}$ , is inserted as a parameter. The integrated derivative data without the constant of integration is shown to the right of the figures. The zero of  $\Delta K$  is obtained by a computer correlation procedure to deconvolute the background derivative [2]. The zero of the  $\Delta K$  wavelength modulation result is subsequently normalized to an absorption coefficient determined by laser calorimetry shown in each figure, which effectively supplies the constant of integration. To read the actual absorption coefficient at a given wavelength, one merely adds or subtracts the value of  $\Delta K$  at that wavelength to the calorimetric value.

The absolute value of the absorption coefficient can be slightly ambiguous in providing the baseline data using multi-mode laser calorimetry since the mode structure of the laser can straddle some line features in the absorption spectrum of the sample. Obtaining the constant of integration, i.e., the baseline correction by a direct absorption measurement in the same wavelength modulation apparatus would be a more direct procedure as when the derivative measurements span the spectral range into the multiphonon region. This was not done in this work since this procedure would be more precise if the direct absorption measurement were performed above and below the region where the baseline is to be obtained. However, since the main thrust of the present work is to reveal the spectral features of the absorption, the laser calorimetric normalization was used and the values of  $\Delta K$  from the integrated wavelength modulation data displays the fine structure excursions above and below the calorimetric point.

Figure 1a and figure 1b show the absorption spectra of  $BaF_2$  taken in the laboratory ambient and in a dry  $N_2$  atmosphere, respectively. The richness of the spectra should be noted; previous laser calorimetric measurements using a few discrete lines show only a broad peak between  $1-5 \mu\text{m}$  peaking at  $3.4 \mu\text{m}$ . Comparing the spectra in figures 1a and 1b; it should be noted that the absorption within the spectral region from  $1600$  to  $4000 \text{ cm}^{-1}$  decreases after the sample has been initially in the laboratory atmosphere and is subsequently placed in a dry  $N_2$  atmosphere for two hours. When the sample is returned to the laboratory ambient for several hours the original structure in figure 1a is recovered. The fact that the magnitude and the linewidths of some of the bands change in a dry  $N_2$  atmosphere indicates that a portion of the absorption is due to surface physisorption. The structures that persist even when the samples are flushed in dry  $N_2$  may be due to surface chemisorption species or volume impurities. The absorption edge starting at  $1000 \text{ cm}^{-1}$  and increasing to lower energy is the multiphonon absorption tail.

Crystals containing substitutional molecular anion impurities typically exhibit a number of sharp infrared absorption bands corresponding to various internal modes of polyatomic ions. There may be small shifts in frequency and increase in linewidths depending on the particular host; however, because of the relatively small interaction with the crystal host, the vibrational frequencies can be used to identify a particular chemical impurity and the nature of its bonding. In addition to bulk absorption there is the possibility of surface absorption which can be comparable to bulk absorption which can be due to crystal growth techniques, mechanical or chemical polishes and chemical cleaners. In addition, exposure to the atmosphere can lead to a deposition of a conglomeration of impurities.

Correlation-type charts have been published which tabulate molecular-ion vibrational frequencies as a means of identification of possible surface and volume impurities in laser windows [3]. If one considers a complete frequency overlay of all possible impurities that can be present in concentrations of 0.1 ppm, one would expect a quasi-continuum absorption throughout the  $2.5$  to  $12.0 \mu\text{m}$  region due to the overlap of the Lorentzian tails of the various absorption bands. However, the distinct absorption bands observed in the present work indicates the presence of dominant impurities. Consequently, rather than dwelling on the multiplicity of possible impurities, we shall consider the common molecular anion impurities such as the metaborates, nitrides, hydrocarbons, carbonates, and  $OH^-$  ions that are revealed by conventional absorption spectroscopy of pure commercial crystals since it is reasonable to expect that they may still be present at lower levels in purified materials.

The vibrational frequencies of common bonds of some polyatomic anions are shown in figures 2a and 2b which display the  $OH^-$ , C-H and carbonate groups and the metaborates and nitrides, respectively; figure 2a will be used primarily in the following analysis since these impurities seem to be dominant; however, bands in figure 2b may also be present.

If we examine figure 1a for the laboratory atmosphere data in conjunction with figures 2a and 2b, it is possible to identify some possible impurities. A prominent band at  $4.2 \mu\text{m}$  can be associated with the physisorption of atmospheric  $CO_2$ . The bands in the  $4$  to  $6 \mu\text{m}$  and  $2.8 \mu\text{m}$  regions can be due to atmospheric water, while the bands in the  $3$  to  $4 \mu\text{m}$  region can be assigned to an overlap of hydrocarbon bands. The bands in the  $6$  to  $8 \mu\text{m}$  region seem to be associated with carbonates. The fact that the bands in the  $4$  to  $6$ ,  $2.8 \mu\text{m}$  and  $3$  to  $4 \mu\text{m}$  regions are largely due to physisorbed species is confirmed by the decrease in absorption in the dry  $N_2$  atmosphere data shown in figure 1b.

The region between  $6$  and  $8 \mu\text{m}$  in  $BaF_2$  shows considerable structure whose magnitude varies only slightly with dry  $N_2$  flushing. As we have previously indicated by the examination of figures 1a and 1b in conjunction with figures 2a and 2b these structures can be associated with the chemisorption of carbonates. Photoacoustic measurements on  $BaF_2$  and  $SrF_2$  using a  $CO$  laser that was tunable to discrete lines in the  $6$  to  $8 \mu\text{m}$  region [4] have revealed step-like structures in the surface adsorption, while our measurements reveal distinct bands.

The  $MgF_2$  laboratory atmosphere data shown in figure 3a reveal a cluster of bands similar to those observed in  $BaF_2$ . Again the ubiquitous  $CO_2$  at 4.2  $\mu m$  is evident. The 2.8 and 4 to 6  $\mu m$  regions reveal the "liquid" water and  $OH^-$  bands, while the 3 to 4  $\mu m$  region reveals the possible overlap of C-H bands. The 6 to 8  $\mu m$  bands seen in  $BaF_2$  seem to be absent or are obscured by the strong water band in the 4 to 6  $\mu m$  region. The dry  $N_2$  data in figure 3b shows a dramatic suppression of all the above bands. The remaining structure can be due to volume or chemisorbed species; the rise in the neighborhood of 2.8 and 4.8 can be due to  $OH^-$  and "liquid" water, respectively.

The  $SrF_2$  sample in laboratory atmosphere shown in figure 4a is very similar to the structure seen in  $BaF_2$  and the identifications of the bands are similar to the  $BaF_2$  discussion. However, it should be noted that the dry  $N_2$  atmosphere run in figure 4b shows a much greater decrease in the structure compared to the  $BaF_2$  dry  $N_2$  run. The remaining structures in figure 4b can be due to bulk or chemisorption with the possible identifications: 6 to 8  $\mu m$  (carbonates), 3 to 4  $\mu m$  (C-H bands), 2.3  $\mu m$  ( $OH^-$ ).

The  $CaF_2$  laboratory data in figure 5a again shows a similar distribution of bands as exhibited by the  $BaF_2$  and  $SrF_2$  sample with a possible similar identifications of the bands. The marked decrease in height of these bands in the dry  $N_2$  is again evident as shown in figure 5b.

The distribution of the bands in  $NaF$  in figure 6a exhibits the familiar pattern previously discussed for  $BaF_2$ ,  $SrF_2$ , and  $CaF_2$ . However, figure 6b shows a large decrease in the band heights in the 2.5 to 4.0  $\mu m$  region.

The  $LaF_3$  sample in the laboratory atmosphere shown in figure 7b reveals the 4.2  $\mu m$   $CO_2$  band, the 6 to 8  $\mu m$  possible carbonates and the  $OH^-$  band near 2.8  $\mu m$ . However, it should be noted that the bands in the 3 to 4  $\mu m$  region due to C-H vibrations which have been prominent in  $BaF_2$ ,  $MgF_2$ ,  $SrF_2$ ,  $CaF_2$  and  $NaF$  seem to be absent or greatly suppressed. In the dry  $N_2$  data in figure 7b the peak near 2.8  $\mu m$  possibly due to  $OH^-$  is about the same height as in figure 7a. One should note the decrease in the overall absorption in the 4 to 8  $\mu m$  region as indicated by the large negative values of  $\Delta K$ .

The  $NaCl$  data in both the laboratory and dry  $N_2$  atmosphere data in figure 8a and 8b, respectively, show prominent structures. Although the spectral distribution is different in detail in both of these figures one can still identify the: 6 to 12  $\mu m$  (carbonates), 4.8  $\mu m$  ("liquid" water), the 4.2  $\mu m$  ( $CO_2$ ), 3 to 4  $\mu m$  (C-H) and the 2.8  $\mu m$  ( $OH^-$ ) bands. The prominence of the bands in both ambients is consistent with the greater surface activity expected for  $NaCl$  as compared to the above substances. Although there is a large decrease in the height of the bands in figure 8b, as shown by the large negative values of  $\Delta K$ , most of the bands are still evident that were present in figure 8a.

The  $LiF$  data in figures 9a and 9b show little structure indicating that  $LiF$  is the least surface active of all the substances studied. The absence of the 4.2  $\mu m$   $CO_2$  band which was visible in all the previous substances studied including  $KBr$  and  $KCl$  which was previously published [1] should be noted. The only band which seems to be noticeable is 4.5  $\mu m$  band in both ambients possibly due to water.

The data for  $MgO$  are shown in figures 10a and 10b. The most prominent features seen in the laboratory ambient are: a doublet in the 2.8 to 3.0  $\mu m$  region (water and  $OH^-$ ), some aspects of a possible 4.2  $\mu m$  ( $CO_2$ ), structure in the 4 to 6  $\mu m$  region (liquid  $H_2O$ ) and very slight structure in the 3 to 4  $\mu m$  region (hydrocarbons). It is interesting to note that of the doublet in the laboratory ambient it is only the 3.0  $\mu m$  band which survives dry  $N_2$  flushing with a noticeable suppression of the 2.8  $\mu m$  band. In a previous study of  $MgO$  [5] impurity bands were observed between the 3.3  $\mu m$  and 2.7  $\mu m$ . Our study clearly shows that the 3.0  $\mu m$  band is due to bulk or chemisorbed  $OH^-$  while the 2.8  $\mu m$  band is due to physisorbed  $OH^-$ .

The region of intrinsic absorption in  $MgO$  shows some fluted structures in the multiphonon absorption tail. The rise around  $1600 \text{ cm}^{-1}$  (6.3  $\mu m$ ) agrees with the shoulder previously studied in the multiphonon spectra of  $MgO$  [6] and was attributed to 4TO phonons by suitably averaging over the 115-person curves.

#### 4. Summary

Figure 11 shows a "schematic" representation of the typical spectra seen in most of the samples in the laboratory atmosphere; this "free-hand" drawing essentially summarizes the dominant bands that are observed! An examination of all of the samples studied except  $LiF$  show many features in common despite the fact that a cursory glance would emphasize the differences in detail. The 6 to 8  $\mu m$  (carbonates), the 4-6  $\mu m$  (liquid water), the 4.2  $\mu m$  ( $CO_2$ ), the overlap of bands in the 3 to 4  $\mu m$  region (hydrocarbons) and the 3 and 2.8  $\mu m$  bands ( $OH^-$  bound to water and free  $OH^-$ ) are seen in most of the samples. In general, the physisorbed surface character of these bands is confirmed by their marked suppression in a dry  $N_2$  atmosphere.

#### 5. Conclusion

We have measured the continuous spectral distribution of the absorption in a number of materials of interest for laser window applications in the spectral region from 2.5 to 12.0  $\mu m$ . This work has enabled an identification of volume and surface contaminants where their existence could only be conjectured from previous discrete thermocouple laser calorimetry and photoacoustic calorimetry measurements. It is interesting to note that although the diverse chemistry and crystal growth techniques were employed in the preparation of these materials, similar dominant bands are observed in most samples which are due to physisorption, volume, and surface chemisorption. It has been possible to identify the type of bonding of the particular constituents present. The surface character of some of the absorption at levels of  $10^{-4}$  to  $10^{-5} \text{ cm}^{-1}$  indicates the importance of performing measurements in the same ambient when comparing low level absorption measurements by various sensitive techniques. The sensitivity of the infrared wavelength modulation technique indicates that a fraction of a monolayer of surface adsorbed species can be detected. Experiments in controlled ambients and on well characterized surfaces using this technique can be rewarding for the study of the physics and chemistry of surfaces. The dramatic changes in the physisorbed spectra in the substances studied indicate that

a continuous flow of dry N<sub>2</sub> along the outer surfaces of optics may have some rewards in high power laser systems.

#### 6. Acknowledgments

The authors wish to thank Robert Curran for performing the laser calorimetric measurements, Rick Pastor and Mort Robinson for supplying several of the samples for this work, and James A. Harrington, Bradley Bobbs and Michael Burd for helpful discussions.

#### References

- [1] Braunstein, R., Kim, R.K., and Braunstein, M., *Wavelength modulation spectroscopy of highly transparent solids; Laser Damage in Optical Materials; 1979, 30-31 October 1979, NBS Boulder Co., ed. by H.E. Bennett, A.J. Glass and A.H. Guenther, NBS Special Publication 568, U.S. Government Printing Office, Washington, D.C. 1970, p. 99.*
- [2] To be published.
- [3] Flannery, M. and Sparks, M., *Extrinsic absorption in infrared laser-window materials; Laser Damage in Optical Materials; 1977, 4-6 October 1977, Boulder, Colo., ed by A.J. Glass and A.J. Guenther, NBS Special Publication 509, U.S. Government Printing Office, Washington, D.C. 1977, p. 5.*
- [4] Hordvik, A., *Measurement techniques for small absorption coefficients: recent advances, Appl. Opt. 16, 2827 (1977).*
- [5] Harrington, J.A., Gregory, D.A., and Otto, Jr., W.F., *Infrared absorption in chemical laser window materials, Appl. Opt. 15, 1953 (1976).*
- [6] Gourley, J.T., and Runciman, W.A., *Multiphonon absorption spectra of MgO and CaO, J. Phys. C. Solid State Phys. 6, 583 (1973).*

Table 1. Origins of the samples used in this work.

---

$\text{BaF}_2$	- HARSHAW
$\text{MgF}_2$	- OPTOVAC
$\text{SrF}_2$	- Hughes Research Laboratories - Press-forged from RAP Boule
$\text{CaF}_2$	- HARSHAW
$\text{NaF}$	- OPTOVAC
$\text{LaF}_3$	- Hughes Research Laboratories - He+HF cast
$\text{NaCl}$	- Hughes Research Laboratories
$\text{LiF}$	- MELLER
$\text{MgO}$	- OPTOVAC

---

#### FIGURE CAPTIONS

Figure 1a. Wavelength modulation spectra of  $\text{BaF}_2$  in the laboratory atmosphere.

Figure 1b. Wavelength modulation spectra of  $\text{BaF}_2$  in a dry  $\text{N}_2$  atmosphere.

Figure 2a. Correlation chart of carbonates, C-H, O-H and water frequencies.

Figure 2b. Correlation chart of metaborate and nitride frequencies.

Figure 3a. Wavelength modulation spectra of  $\text{MgF}_2$  in the laboratory atmosphere.

Figure 3b. Wavelength modulation spectra of  $\text{MgF}_2$  in a dry  $\text{N}_2$  atmosphere.

Figure 4a. Wavelength modulation spectra of  $\text{SrF}_2$  in the laboratory atmosphere.

Figure 4b. Wavelength modulation spectra of  $\text{SrF}_2$  in a dry  $\text{N}_2$  atmosphere.

Figure 5a. Wavelength modulation spectra of  $\text{CaF}_2$  in the laboratory atmosphere.

Figure 5b. Wavelength modulation spectra of  $\text{CaF}_2$  in a dry  $\text{N}_2$  atmosphere.

Figure 6a. Wavelength modulation spectra of  $\text{NaF}_2$  in the laboratory atmosphere.

Figure 6b. Wavelength modulation spectra of  $\text{NaF}_2$  in a dry  $\text{N}_2$  atmosphere.

Figure 7a. Wavelength modulation spectra of  $\text{LaF}_3$  in the laboratory atmosphere.

Figure 7b. Wavelength modulation spectra of  $\text{LaF}_3$  in a dry  $\text{N}_2$  atmosphere.

Figure 8a. Wavelength modulation spectra of  $\text{NaCl}$  in the laboratory atmosphere.

Figure 8b. Wavelength modulation spectra of  $\text{NaCl}$  in a dry  $\text{N}_2$  atmosphere.

Figure 9a. Wavelength modulation spectra of  $\text{LiF}$  in the laboratory atmosphere.

Figure 9b. Wavelength modulation spectra of  $\text{LiF}$  in a dry  $\text{N}_2$  atmosphere.

Figure 10a. Wavelength modulation spectra of  $\text{MgO}$  in the laboratory atmosphere.

Figure 10b. Wavelength modulation spectra of  $\text{MgO}$  in a dry  $\text{N}_2$  atmosphere.

Figure 11. "Schematic" representation of the typical spectra seen in most samples in the laboratory atmosphere.

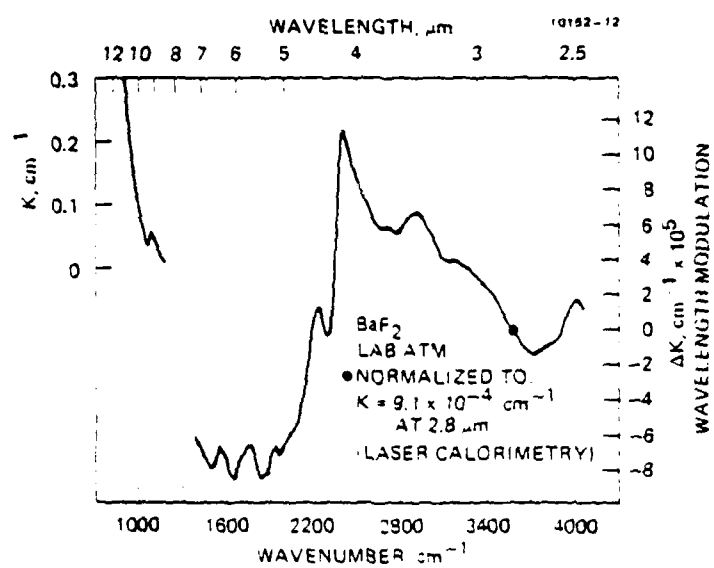


Figure 1a

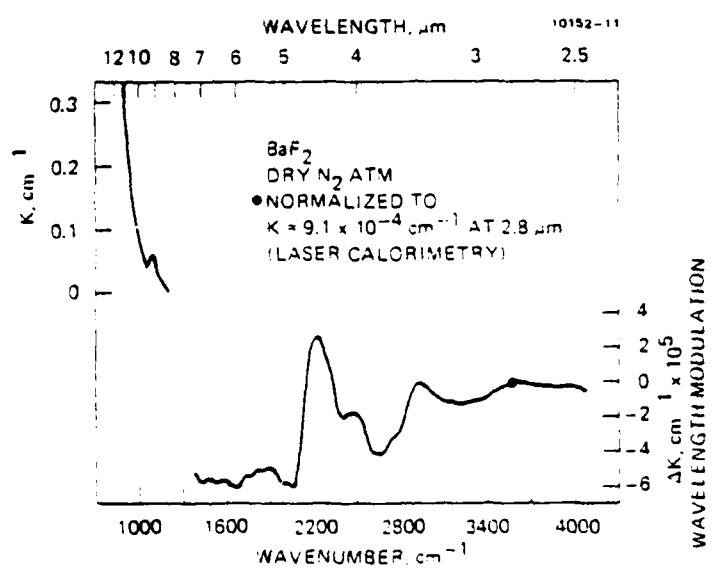


Figure 1b

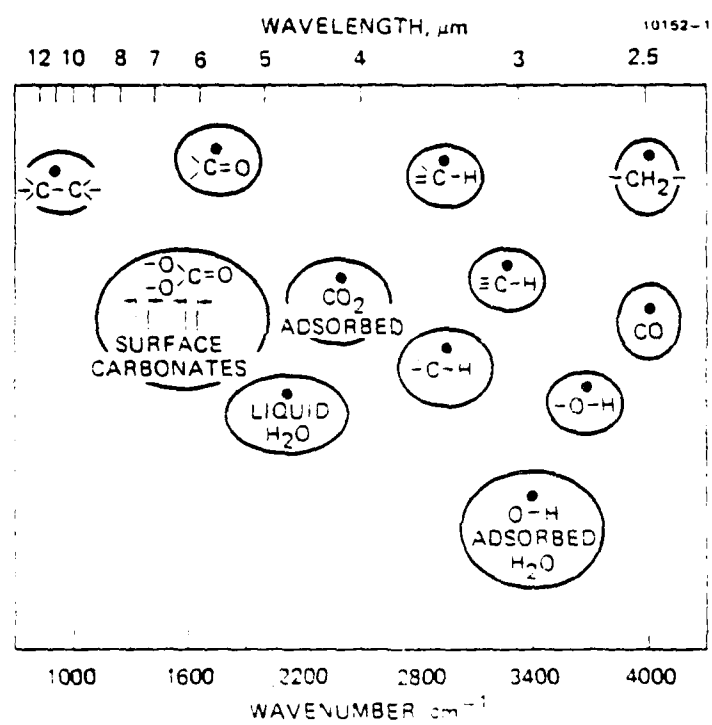


Figure 2a

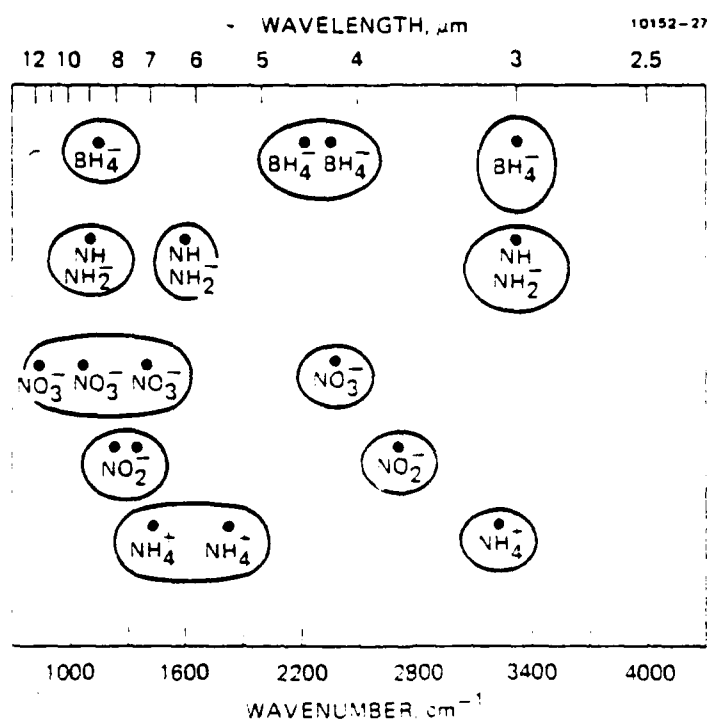


Figure 2b

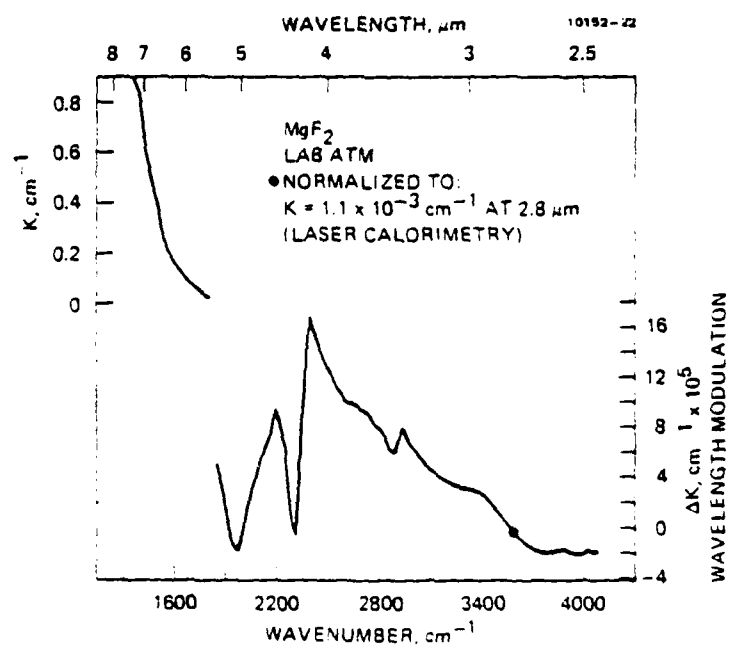


Figure 3a

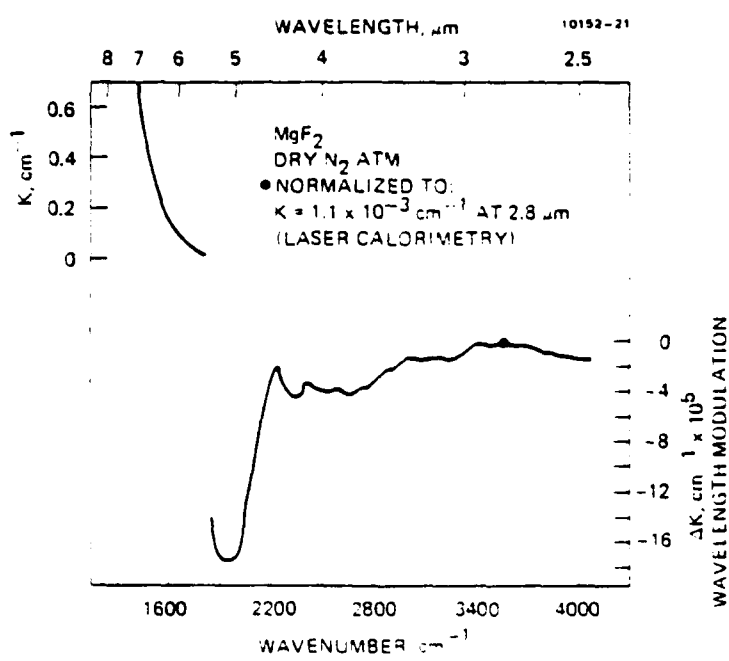


Figure 3b

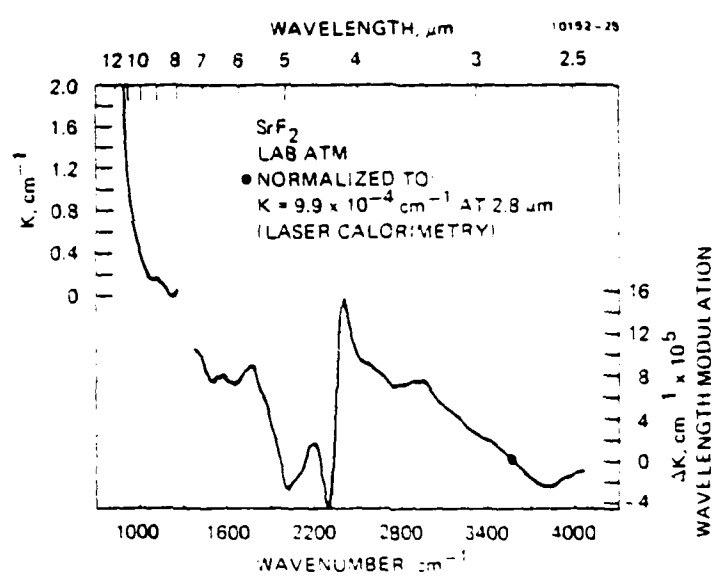


Figure 4a

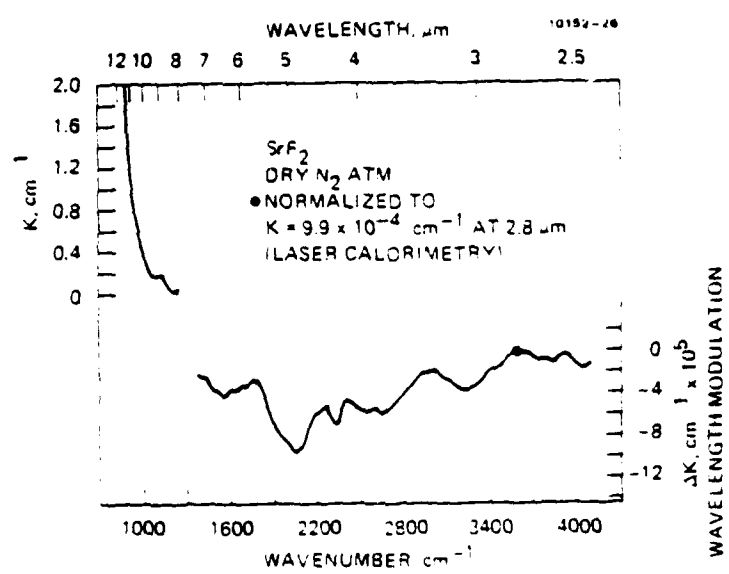


Figure 4b

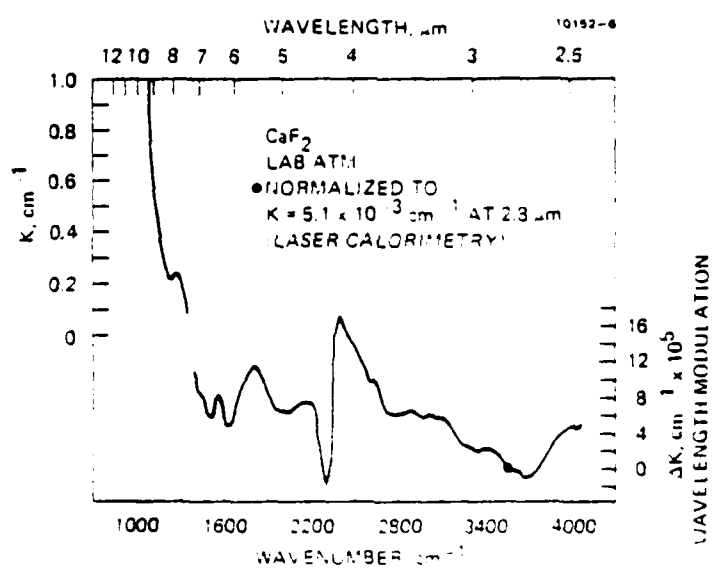


Figure 5a

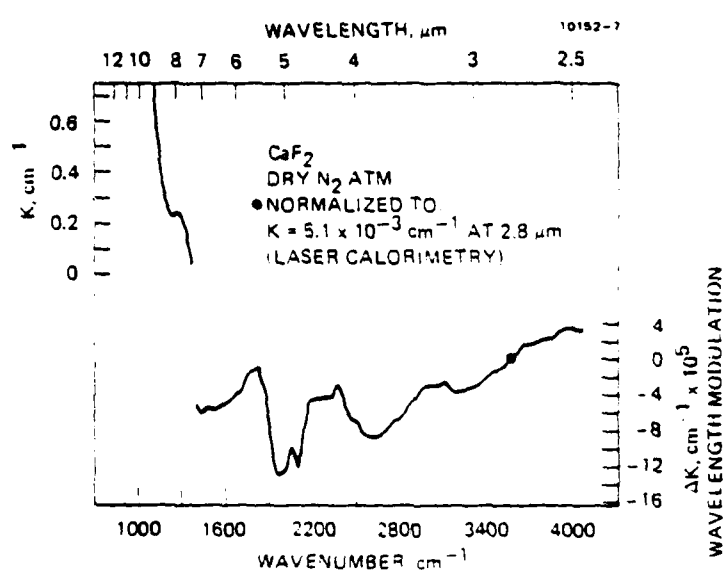


Figure 5b

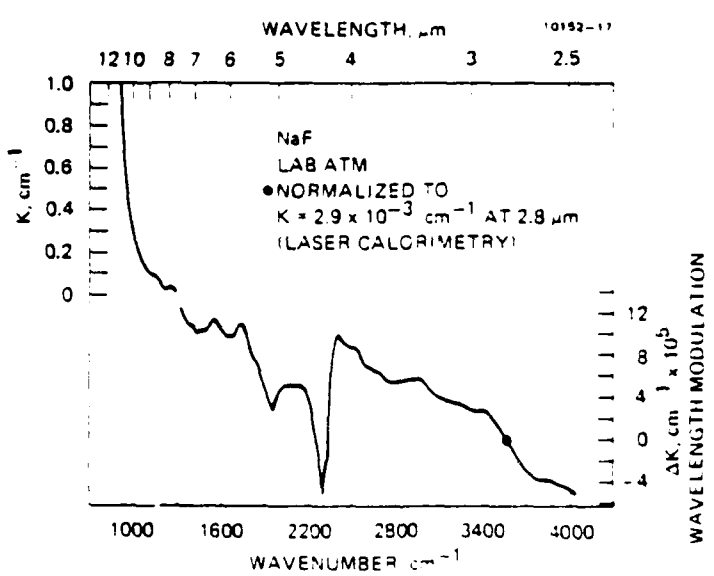


Figure 6a

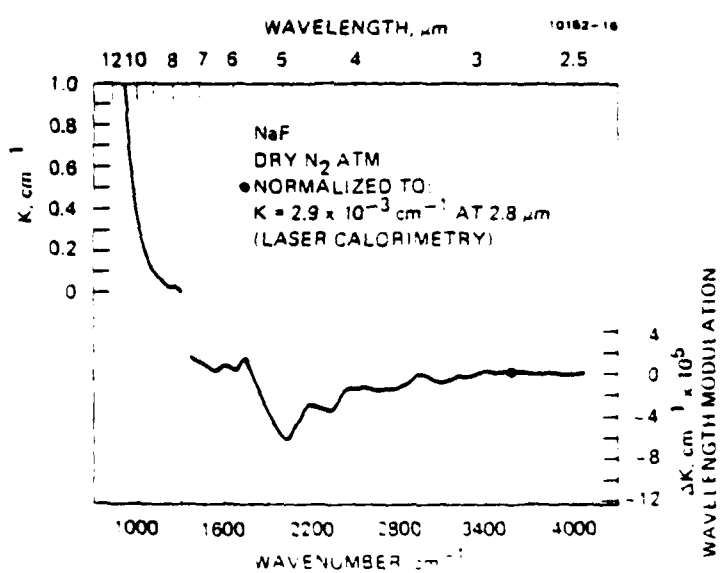


Figure 6b

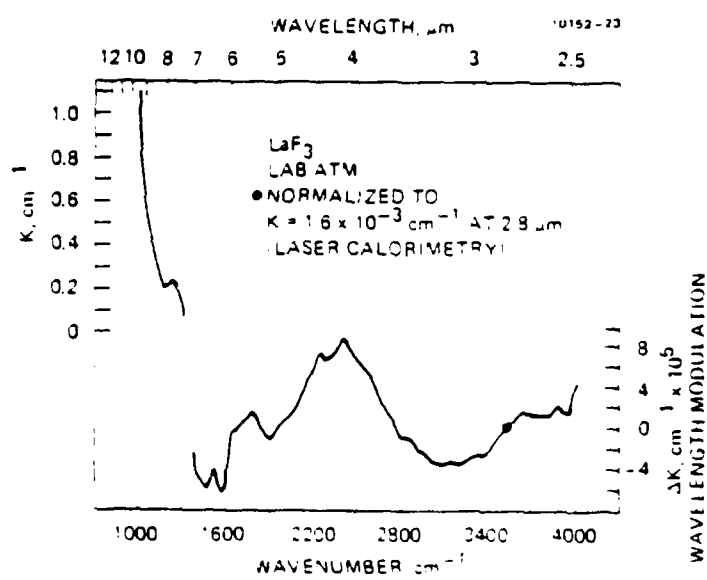


Figure 7a

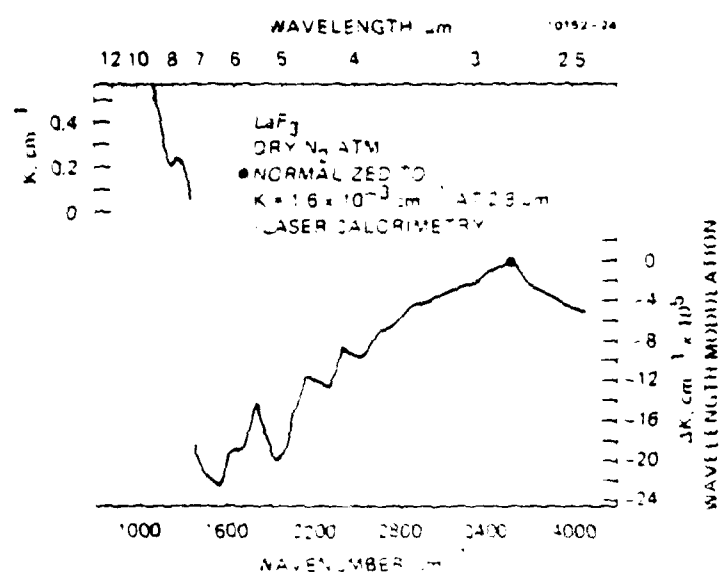


Figure 2b

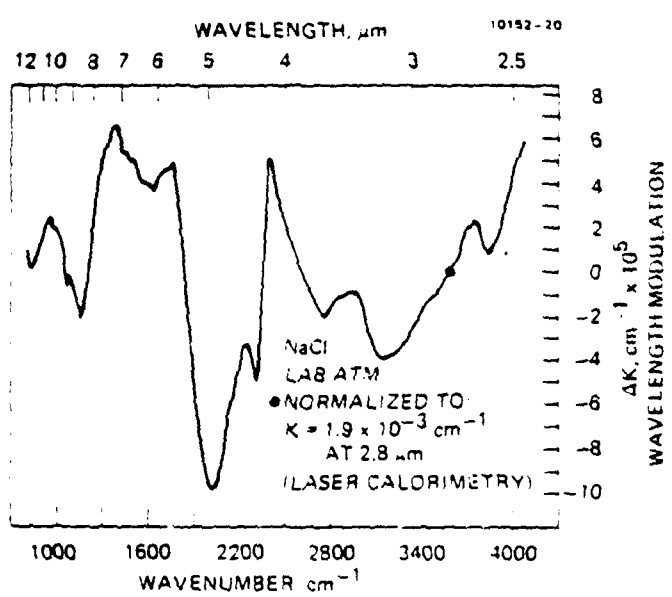


Figure 8a

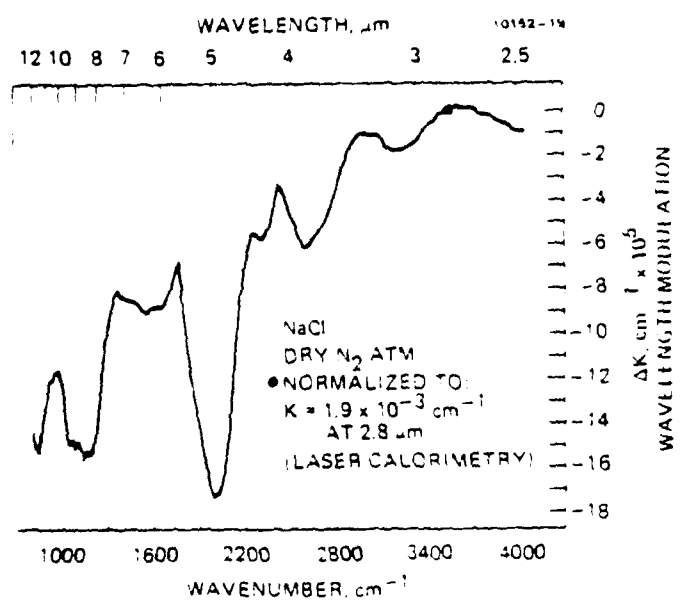


Figure 8b

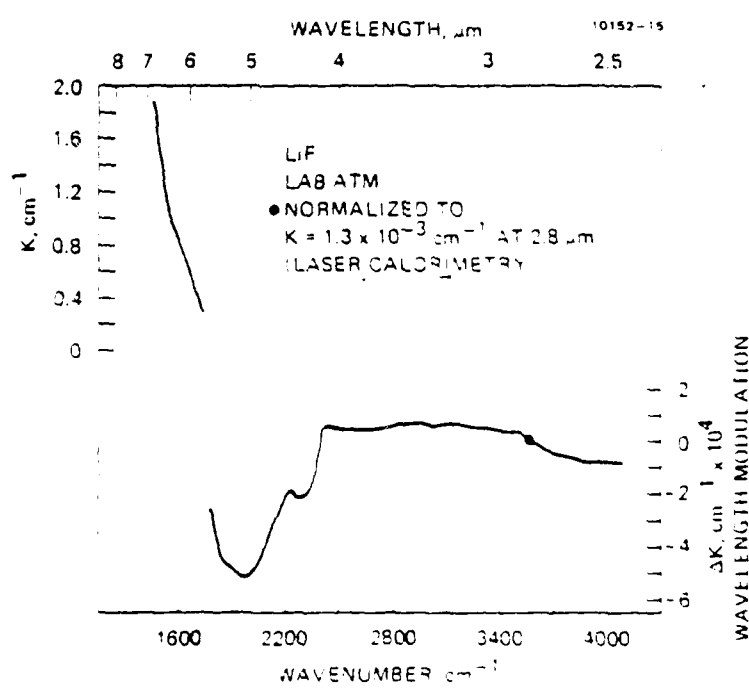


Figure 9a

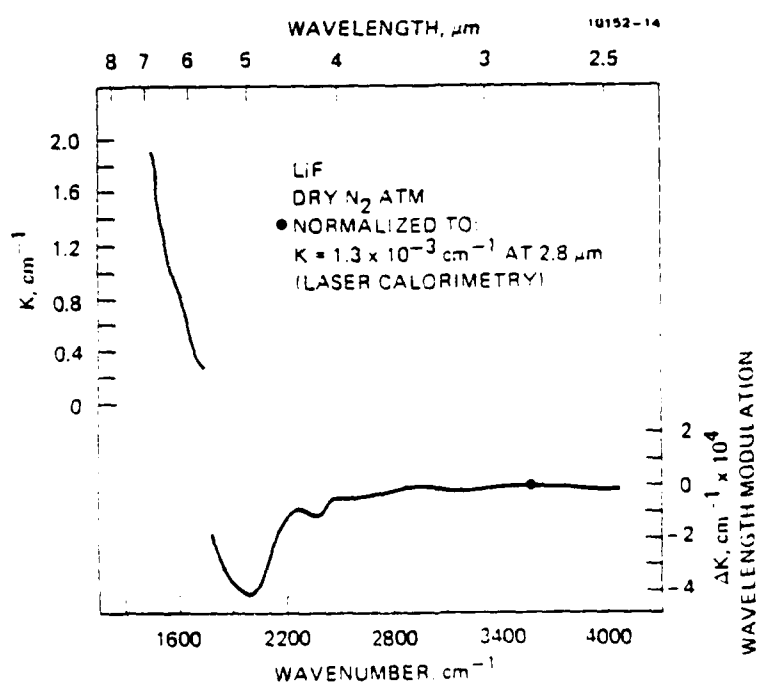


Figure 9b

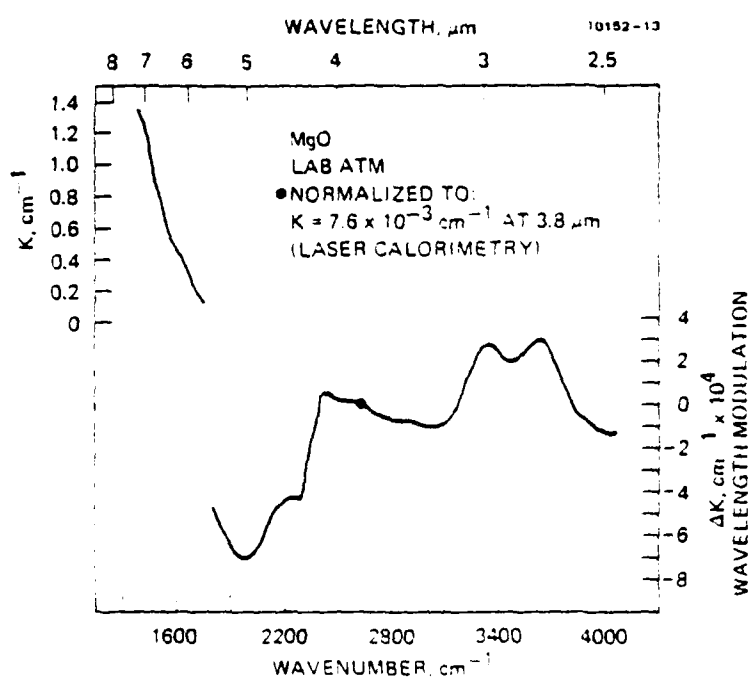


Figure 10a

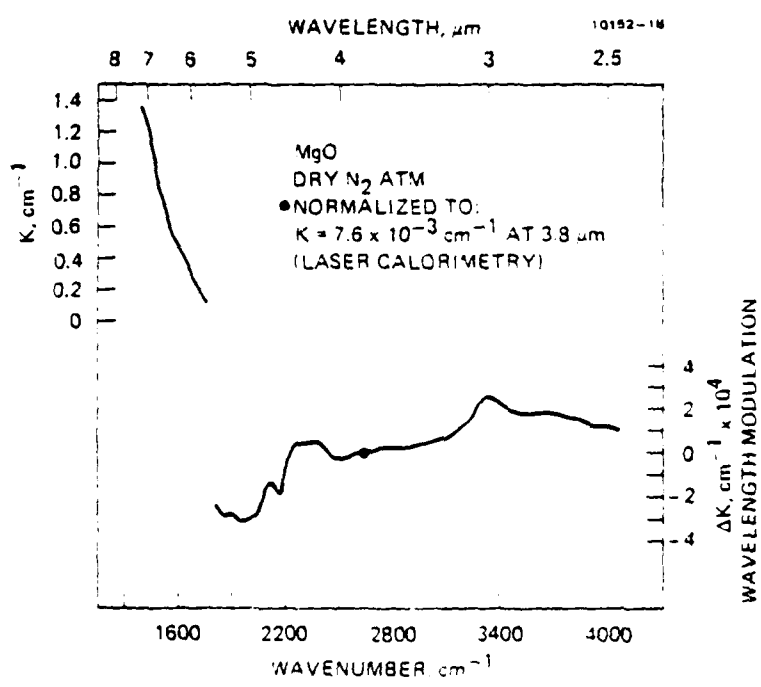


Figure 10b

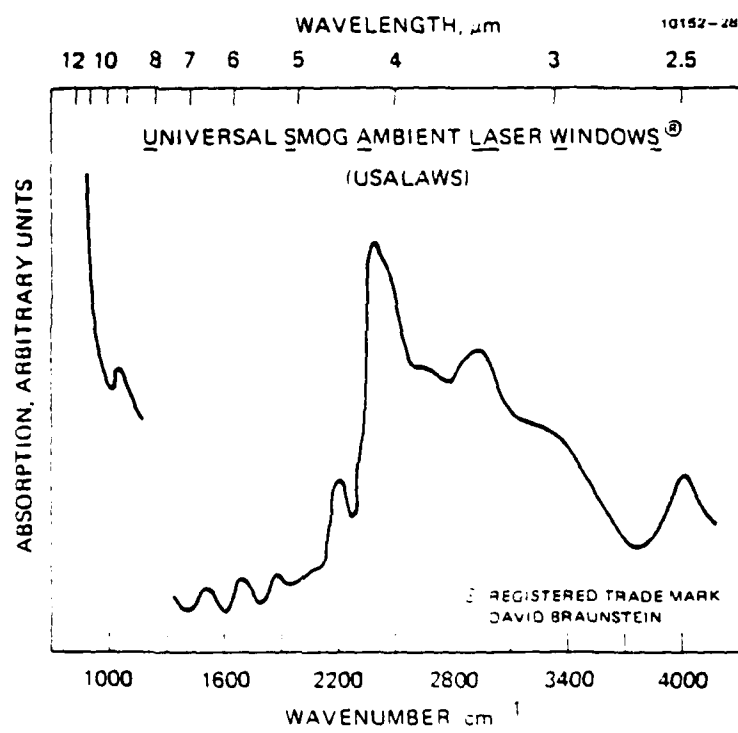


Figure 11

SCATTERING LOSSES IN SINGLE AND POLYCRYSTALLINE  
MATERIALS FOR INFRARED FIBER APPLICATIONS

J.A. Harrington and M. Braunstein

Hughes Research Laboratories<sup>†</sup>

Malibu, CA 90265

B. Bobbs<sup>\*</sup> and R. Braunstein

University of California at Los Angeles<sup>††</sup>

Los Angeles, CA 90024

ABSTRACT

Polycrystalline fiber waveguides, fabricated from infrared transparent solids such as KRS-5 and KCl, have measured losses much greater than conventional silica fibers. One major source of these losses is scattering from grain boundaries present in the polycrystalline fibers. To improve the optical transmission of our infrared waveguides, we have studied the losses due to scattering in single and polycrystalline materials which are suitable for fabrication into infrared transmissive waveguides.

<sup>\*</sup>Hughes Staff Doctoral Fellow.

<sup>†</sup>This work has been supported by Hughes Aircraft Company internal research and development programs and by RADC, Hanscom AFB, Mass.

<sup>††</sup>This work has been supported in part by AFOSR and ARO (Durham).

## INTRODUCTION

Optical fiber waveguides made from crystalline materials such as KRS-5 (TlBrI), TlBr, AgCl, and KCl have been used for a variety of 10.6- $\mu\text{m}$ ,  $\text{CO}_2$  laser applications.<sup>1-4</sup> The losses in the current IR fibers, however, are high (lowest loss measured is 300 dB/km at 10.6  $\mu\text{m}$  in KRS-5) and applications in sensor and laser power delivery systems have been limited to short (1- to 2-m) lengths of fiber.<sup>2-4</sup> This measured IR fiber attenuation is considerably higher than that predicted theoretically for these and related IR transparent materials.<sup>2,5</sup> In fact, Gentile et al.<sup>2</sup> and van Uitert and Wemple<sup>5</sup> have shown that these materials have projected losses as low as  $10^{-3}$  dB/km near 5  $\mu\text{m}$ . To develop this ultra-low-loss potential, for such applications as long-distance communication links, requires a careful analysis of the nature of the attenuation mechanisms present in IR transparent waveguides. In this paper, we address the contribution of scattering to the total attenuation in bulk materials that have the potential for being fabricated into highly transparent fibers.

The attenuation mechanisms present in low-loss solids are illustrated in Fig. 1 for fused silica. At the shortest wavelengths, electronic processes (Urbach tail) contribute heavily to the total loss. At the IR wavelengths of interest, however, two mechanisms — scattering and multiphonon absorption — have been identified as the ultimate, limiting loss processes.<sup>2</sup> In Fig. 1, the curves for

scattering (which decreases as  $\lambda^{-4}$  with increasing wavelength) and lattice (multiphonon) absorption (which increases exponentially with increasing wavelength) cross to yield a minimum in the total attenuation. For fused silica, this minimum, which is about 0.25 dB/km at 1.6  $\mu\text{m}$ , has been achieved in kilometer-long fibers.<sup>6</sup> For certain crystalline as well as special glassy solids, minima occur near 5  $\mu\text{m}$  with projected losses well below the intrinsic losses measured in silica (projected losses are given in the next section).

The total attenuation coefficient  $\alpha_T$  may be written as the sum

$$\alpha_T = \alpha_S + \alpha_A , \quad (1)$$

where  $\alpha_S$  and  $\alpha_A$  are the contributions due to scattering and absorption, respectively. Each term in Eq. 1 can be measured independently, thus allowing the individual mechanisms contributing to the overall optical loss in solids to be studied. For example,  $\alpha_T$  can be obtained from standard spectroscopic and fiber insertion loss measurements while laser calorimetry has been used very successfully to determine residual absorption  $\alpha_A$  in weakly absorbing materials. The scattering terms  $\alpha_S$  has not been as well studied. Measurements using integrating spheres for both bulk and fiber materials are generally used to obtain a total integrated scattering (TIS) loss.

These methods, however, have the disadvantage of being unable to distinguish among the various individual scattering mechanisms contributing to TIS. To elucidate the various scattering mechanisms as well as to obtain a value for  $\alpha_S$ , we have chosen to study the light scattering spectra of solids. These spectra are composed of elastically (Rayleigh) scattered light that results from various nonpropagating fluctuations in the materials index of refraction and inelastically (Brillouin) scattered light that results from the interaction of light and the thermal motion of ions (sound waves). Although Rayleigh-Brillouin (RB) spectra have been used to measure  $\alpha_S$  in glasses,<sup>7</sup> this technique has not been expressly used before to study scattering losses in single- and poly-crystalline materials. In this work, we have measured RB scattering at 90° in bulk single- and poly-crystalline KCl. As discussed in the next section, we expect very little Rayleigh scattering in single-crystal materials; for polycrystalline samples, however, intuition suggests that the residual strain and grain boundaries associated with the hot press-forged, polycrystalline material should lead to larger amounts of scattering. Our preliminary results support this presumption, but we have not yet been able to account for the source of each scattering mechanism contributing to the RB spectra.

#### GENERAL CONSIDERATIONS

The limiting attenuation mechanisms in transparent solids are scattering and multiphonon absorption. These contributions have

been considered by several investigators in the context of projecting future ultra-low-loss materials for the next generation of fiber waveguides. Van Uitert and Wemple<sup>5</sup> have studied the potential of  $ZnCl_2$  (a glass former) while Gentile et al.<sup>2</sup> and Pinnow et al.<sup>1</sup> have concentrated on the crystalline materials. In Fig. 2, we consider the projected transmission for KRS-5 and KCl and compare these predictions to fused silica. The curves in Fig. 2 show the characteristic V shape resulting from the crossing of the scattering (short wavelength) and multiphonon (long wavelength) attenuation mechanisms. The only scattering mechanism assumed in calculating the  $\lambda^{-4}$ -dependent scattering curve for KRS-5 and KCl was Brillouin scattering ( $\alpha_B$  - see below). As mentioned above, the V-shaped curve for silica has essentially been traced out experimentally and thus silica fiber losses are now intrinsic. For KCl and KRS-5 (as well as for many other non-oxide ionic solids), however, Fig. 2 shows the extremely low loss potential for these materials near 5  $\mu m$ .

To determine  $\alpha_S$  from RB light scattering experiments requires a careful measurement of the intensity of both the Brillouin- and Rayleigh-scattered light. Brillouin scattering results from light that has been inelastically scattered (Bragg scattering) from acoustical phonons (sound waves). The frequency of the scattered light is Doppler shifted from the frequency of the laser light  $\omega_L$  by an amount  $\pm \Delta \omega$ :

$$\Delta = \frac{4\pi n v \sin(\theta/2)}{\lambda_0} \quad ,$$

where  $n$  is the index of refraction of the medium,  $v$  is the velocity of sound,  $\theta$  is the scattering angle, and  $\lambda_0$  is the vacuum wavelength of the light. This frequency shift has been well studied in alkali halides.<sup>8</sup> The Rayleigh-scattered light (central maximum at  $\omega_L$ ) is due to scattering of light from nonpropagating fluctuations in the dielectric constant. In glasses, mechanisms which give rise to these fluctuations include: density variations resulting from the frozen-in, random variations in dielectric constant inherent in a disordered solid; concentration fluctuations resulting from the local compositional variations present in mixtures; and entropy fluctuations resulting from temperature variations.<sup>7</sup> Of the three, only entropy fluctuations, which are very weak, would be present in an ideal single crystal.

To obtain  $\chi_S$ , we first evaluate the intensity ratio of the Rayleigh ( $I_R$ ) to the total Brillouin ( $2I_B$ ) scattered light. This ratio is called, based on its use in light scattering in liquids, the Landau-Placzek ratio  $R_{LP}$  and is defined<sup>7</sup> as

$$R_{LP} \equiv \frac{I_R}{2I_B} \quad . \quad (2)$$

Strictly speaking, since  $I_R$  and thus  $R_{LP}$  are related to specific scattering mechanisms (such as those discussed above for glasses),

measured values of  $R_{LP}$  are generally regarded as a property of a given material (e.g., fused  $SiO_2$  has an  $R_{LP} \geq 23$ , while  $33K_2O-67SiO_2$  has an  $R_{LP} \geq 10$ ).<sup>9</sup> In our experiments, we measure  $I_R$  without, in general, knowing the specific mechanisms contributing to the Rayleigh component of scattered light. Therefore, we should more appropriately speak of an effective Landau-Placzek ratio with  $I_R$  representing the intensity of the central maximum.

The measured  $R_{LP}$  is then used to calculate  $\alpha_S$ , as described by Pinnow et al.<sup>10</sup> and others,<sup>7,9</sup> from the relationship

$$\alpha_S = \alpha_B (R_{LP} + 1) \quad . \quad (3)$$

where  $\alpha_B$  is the small residual attenuation coefficient due to Brillouin scattering alone. It is given by

$$\alpha_B = \frac{8\pi^3}{3} \frac{1}{4} \left( \frac{\pi^3 P_{12}^2}{\alpha} \right) k_B T B_T \quad , \quad (4)$$

where  $P_{12}$  is the photoelastic (Pockels) coefficient,  $T$  is the temperature,  $k_B$  is Boltzmann's constant, and  $B_T$  is the isothermal compressibility. For ideal single crystals,  $I_R \geq 0$ , thus  $R_{LP} \geq 0$  and (from Eq. 3)  $\alpha_S \geq \alpha_B$ . This leads to the scattering curves in Fig. 2 for KRS-5 and KCl, which were calculated from Eq. 4 alone, while the scattering for fused silica was calculated from Eq. 3 using  $R_{LP} = 23$ .

An interesting feature of measured  $R_{LP}$ s for crystalline solids is their dependence on polarization. For our single-crystal measurements in KCl, a [100] crystal orientation was used for most samples studies. With incoming light along the [100] direction and scattered light along the [010], the polarization of the incident and analyzed scattered light was either vertical (V) or horizontal (H) with respect to the scattering plane. For this geometry, we may determine the intensities of the Brillouin components from the selection rules for the rock salt structure ( $O_h$ ) and the differential cross section.<sup>11</sup> The intensities  $I$  and allowed vibrational modes for the various polarizations (phonon momentum  $q$  along [110] direction) are summarized in the matrix given in Table 1a. Using the known photoelastic ( $P_{12}$  and  $P_{44}$ ) and elastic ( $C_{11}$ ,  $C_{12}$ , and  $C_{44}$ ) constants for KCl,<sup>12</sup> we calculate the matrix elements in Table 1a and give them, normalized to  $I_{HH}$  (the weakest intensity), in Table 1b. Table 1b shows that the intensities of the longitudinal modes (frequency equal to 15.8 GHz) in VV polarization are much stronger than those in the other polarizations (transverse mode frequency equal to 7.2 GHz). This means that measured Landau-Placzek ratios may vary greatly depending on crystal orientation and polarization, with the smallest  $R_{LP}$  occurring for the VV polarization.

## LIGHT SCATTERING MEASUREMENTS

The RB spectra were recorded using as a source an Ar-ion laser (Spectra Physics Model 165) delivering 10 to 300 mW of single-line power and a PZT-scanned Fabry-Perot spectrometer. The experimental set-up is shown in the block diagram in Fig. 3. The spectrometer is a Burleigh Instruments, Inc., actively stabilized Fabry-Perot interferometer with its associated photon counting electronics. Data acquisition is provided by a 512-channel Tracor-Northern multichannel analyzer (MCA). This MCA has proven essential for obtaining good S/N ratios for these crystals (between 2000 and 20,000 scans are generally accumulated for each spectrum).

To improve the contrast of the spectrometer, we added a three-pass attachment to the interferometer. This allowed us to readily detect the Brillouin components in the polycrystalline materials where the Rayleigh scattering is more intense. Fig. 4 shows the results of a 90° scattering measurement on polycrystalline KCl doped with 1.75% RbCl taken with the light passing once (one-pass) or thrice (three-pass) through the interferometer. The improved contrast in the three-pass case is obvious. Note in particular the resolution of the transverse modes in the three-pass case that has been lost in the Rayleigh wing in the one-pass case. Clearly, the three-pass arrangement, which has been used in all our measured data, is necessary to obtain a reliable  $R_{LP}$ . The resolution of the triple-pass Fabry-Perot spectrometer was  $0.03 \text{ cm}^{-1}$  (finesse equal to 30).

## RESULTS OF LIGHT SCATTERING EXPERIMENTS

Measurements of scattering losses were made at 488.0 nm in bulk single and polycrystalline KCl. The KCl was reactive atmosphere process (RAP) single-crystal material<sup>13</sup> which was either used in oriented single-crystal (SC) or in hot-press forced, polycrystalline (P) form. The RB scattering data shown in Fig. 5 are for pure, single-crystal KCl oriented as shown in the insert. From the data, we can see the intense stokes (S) and anti-stokes (AS) longitudinal Brillouin components in the VV polarization. The Brillouin components are also seen to become weaker in VH (or HV) and HH polarization, which is in qualitative agreement with the results stated in Table 1 for this scattering geometry. Similar results were obtained for other RAP-grown KCl (SC) although the  $R_{sp}$ 's were found to vary somewhat from sample to sample.

The data for polycrystalline KCl (average grain size, 10  $\mu\text{m}$ ) are shown for two polarizations in Fig. 6. We can see from these data the intense Rayleigh scattering typical of our polycrystalline samples. In this sample, we also note the presence of only longitudinal modes in VV polarization and transverse modes in VH polarization. This leads us to conclude that we have, by chance, illuminated an axis of high symmetry in this sample. Specifically, it would appear from the data that the crystallites are oriented along the [100] direction for this particular experiment. In general, we would expect to observe an admixture of L and T modes

consistent with a random orientation of polycrystalline samples.

Effective Landau-Piaseczek ratios have been calculated for these two samples from the data in Figs. 5 and 6. These data are summarized in Table 2. For the single-crystal KCl,  $R_{LP}$  is lowest for the VV polarization, as discussed above, but the  $R_{LP}$ 's for other polarizations do not scale with the predicted Brillouin intensities (see Table 1). This is due to the polarization dependence of the Rayleigh-scattered light. Our measurements of  $I_R$  indicate that the Rayleigh scattered light is, as expected, most intense for the VV polarization. For this polarization,  $I_R$  is approximately 8 to 10 times stronger than when measured under HV, VH, or HH conditions. More detailed studies of the depolarization ratio might give insight into the nature of the static defect contribution to elastic scattering. In general, the values for  $R_{LP}$  obtained for polycrystalline KCl(P) are higher than those for KCl(SC) (see Table 2). Again, the VV polarization for this unoriented poly sample yields the lowest  $R_{LP}$  and the HH case yields the highest  $R_{LP}$  (this trend was also seen in another KCl(P) sample).

Table 2 also gives the values of  $\alpha_S$  calculated from Eqs. 3 and 4, which, for KCl at 488.0 nm, reduce to,

$$\alpha_S = 1.5 \times 10^{-6} (R_{LP} + 1) \text{ cm}^{-1} .$$

These attenuation coefficients due to scattering may be compared to the absorption coefficients obtained for KCl by laser calorimetric measurements at 488.0 nm by Harrington et al.<sup>14</sup> They found  $\alpha_A \approx 3 \times 10^{-4} \text{ cm}^{-1}$  for KCl(P) and  $\alpha_A < 2 \times 10^{-5} \text{ cm}^{-1}$  for KCl(SC). We see, therefore, that the total attenuation  $\alpha_T (= \alpha_A + \alpha_S)$  is largely due to scattering.

The nature of the Rayleigh scattering in our crystalline samples is not completely understood. The results indicate substantial elastic scattering beyond that predicted above theoretically from entropy fluctuations. One may consider this excess parasitic scattering as arising from mechanical and chemical defects in the crystal. Although all the KCl has been RAP purified, we cannot rule out different amounts of chemical impurities in each sample. It is also evident that residual strain is present in both single and polycrystalline samples (observed as birefringence in crossed polarizers). This strain, which one would intuitively expect to be greater in the hot-forged polycrystalline materials, can lead to substantial elastic scattering. In particular, one would suspect grain boundaries as a potentially strong source of Rayleigh scattering because impurities, voids, and high strain would be more prevalent in these areas.

In our polycrystalline samples, it was not possible to examine the scattering from a single grain boundary because the average grain size (10  $\mu\text{m}$ ) was much smaller than the scattering volume

(cylindrical volume, 350  $\mu\text{m}$  long by 30  $\mu\text{m}$  in diameter). Brody et al.,<sup>15</sup> however, were able to study elastic scattering from a single grain boundary in polycrystalline calcium fluoride (Irtran-3). In their measurements, the grain size (150  $\mu\text{m}$ ) was larger than the scattering volume and they found essentially no difference in the intensity of light scattered from within a crystallite to that scattered from a volume containing a grain boundary. One might conclude from their results that grain boundaries do not contribute to elastic scattering; however, to assess the effect of grain boundaries properly, one must study high-purity material with a low Rayleigh background. Our future experiments will look more closely at the effect as well as the importance of residual strain on the Rayleigh scattered light.

#### SUMMARY

Our RB scattering studies on bulk KCl have been an initial attempt to probe the mechanisms responsible for scattering losses in highly transparent materials. We have found that polycrystalline materials scatter more strongly than do single-crystal materials, but we have not as yet been able to explicitly associate a particular elastic scattering process with a finite contribution to the total scattering. Our results, however, do indicate that, even in these very pure KCl samples, there is more scattering than predicted for the ideal KCl crystals and thus future fiber waveguides from these low-loss materials may be limited

more by scattering than absorption losses. Consequently, it is important to study scattering in poly- and single-crystal materials to understand the origin of the Rayleigh scattering and thereby to determine methods of minimizing this contribution to the attenuation.

#### REFERENCES

1. D.A. Pinnow, A.L. Gentile, A.G. Standlee, A.J. Timper, and L.M. Hobrock, "Polycrystalline Fiber Optical Waveguides for Infrared Transmission," *Appl. Phys. Lett.*, Vol. 33, pp. 28-29, 1978.
2. A.L. Gentile, M. Braunstein, D.A. Pinnow, J.A. Harrington, D.M. Henderson, L.M. Hobrock, J. Myer, R.C. Pastor, and R.R. Turk, "Infrared Fiber Optical Materials," in *Fiber Optics: Advances in Research and Development*, ed. by B. Bendow and S.S. Mitra, pp. 105-118, Plenum Publishing, N.Y., 1977.
3. D. Chen, R. Skogman, G.E. Bernal, and C. Butter, "Fabrication of Silver Halide Fibers by Extrusion," *ibid*, pp. 119-122.
4. J.A. Harrington, "Infrared Fiber Optics for CO<sub>2</sub> Laser Applications," in *CO<sub>2</sub> Laser Devices and Applications*, Proceedings of SPIE Technical Symposium East, Vol. 227, Fall, 1980.
5. L.G. Van Uitert and S.H. Wemple, "ZnCl<sub>2</sub> Glass: A Potential Ultralow-Loss Optical Fiber Material," *Appl. Phys. Lett.*, Vol. 33, pp. 57-59, 1978.

6. S. Kobayashi, N. Shibata, S. Shibata, and T. Izawa, "Characteristics of Optical Fibers in Infrared Wavelength Region," *Rev. of Elect. Comm. Lab. (Japan)*, Vol. 26, pp. 453-468, 1978.
7. For a review see J. Schroeder, "Light Scattering of Glass," in *Treatise on Materials Science and Technology*, Vol. 12 Glass 1: Interaction With Electromagnetic Radiation, pp. 157-222, Academic Press, 1977.
8. G.B. Benedek and K. Fritsch, "Brillouin Scattering in Cubic Crystals," *Phys. Rev.*, Vol. 149, pp. 647-662, 1966.
9. J. Schroeder, R. Mohr, P.B. Macedo, and C.J. Montrose, "Rayleigh and Brillouin Scattering in  $K_2O$ - $SiO_2$  Glasses," *J. Amer. Cer. Soc.*, Vol. 56, pp. 510-514, 1973.
10. T.C. Rich and D.A. Pinnow, "Total Optical Attenuation in Bulk Fused Silica," *Appl. Phys. Lett.*, Vol. 20, pp. 264-266, 1972.
11. W. Hayes and R. Loudon, "Scattering of Light by Crystals, pp. 327-353, J. Wiley & Sons, 1978.
12. Landolt-Bornstein Numerical Data and Functional Relationships in Science and Technology, New Series, ed. by K.H. Hellwege and A.M. Hellwege, Vol. II, pp. 25, 29, 510, and 513, Springer-Verlag, 1979.
13. R.C. Pastor and A.C. Pastor, "Crystal Growth in a Reactive Atmosphere," *Mat. Res. Bull.*, Vol. 10, pp. 117-124, 1975.

14. J.A. Harrington, B.L. Bobbs, M. Braunstein, R. Kim, R. Stearns, and R. Braunstein, "Ultraviolet-Visible Absorption in Highly Transparent Solids by Laser Calorimetry and Wavelength Modulation Spectroscopy," *Appl. Opt.*, Vol. 17, pp. 1541-1546, 1978.
15. E. Brody, C. Roychoudhuri, and M. Hercher, "Brillouin Spectra of  $\text{CaF}_2$  Microcrystals Using a Stable 3-Pass Fabry-Perot Interferometer," *Appl. Phys. Lett.*, Vol. 23, pp. 543-545, 1973.

TABLE I  
Intensities of Brillouin Components for a Rocksalt Crystal

Mode	IVV	IVH = IHV	IHH
(110) L	$\frac{4P_{12}^2}{C_{11} + C_{12} + C_{44}}$	0	$\frac{4P_{44}^2}{C_{11} + C_{12} + C_{44}}$
(a) (110) T	0	0	0
(001) T	0	$\frac{P_{44}^2}{2C_{44}}$	0

Mode	IVV	IVH	IHH
(110) L	133	0	1
(b) (110) T	0	0	0
(001) T	0	4.8	0

TABLE II  
Effective  $R_{LP}$  and Calculated Values of  $\alpha_S$

Structure	Polarization	$R_{LP}$	$\alpha_S$ ( $\text{cm}^{-1}$ )
Single	VV	26.2	$4.1 \times 10^{-5}$
Crystal	VH	38.5	$5.9 \times 10$
(SC)	HV	44.9	$6.9 \times 10^{-5}$
	HH	276.4	$4.2 \times 10^{-4}$
<hr/>			
Polycrystalline	VV	496	$7.5 \times 10^{-4}$
(P)	VH	830	$1.2 \times 10^{-3}$
	HV	1598	$2.4 \times 10^{-3}$
	HH	>5000	$>7.5 \times 10^{-3}$

## FIGURE CAPTIONS

Fig. 1 - Schematic representation of optical attenuation mechanisms in solids.

Fig. 2 - Projected losses for some IR transparent materials.

Short wavelengths are bounded by  $1/\lambda^4$ -scattering and long wavelengths by multiphonon absorption.

Fig. 3 - Block diagram of scanning Fabry-Perot interferometer for measuring RB spectra.

Fig. 4 - Improved contrast in RB spectra of poly KCl + 1.75% RbCl through the use of 3-pass attachment on Fabry-Perot interferometer. The spectra were all recorded using the 3-pass configuration.

Fig. 5 - Scattering spectra for single-crystal KCl for three different polarizations. Landau-Placzek ratios are given in Table 2 for these data.

Fig. 6 - Scattering spectra for polycrystalline KCl (average grain size is 10  $\mu\text{m}$ ). Landau-Placzek ratios are given in Table 2 for these data.

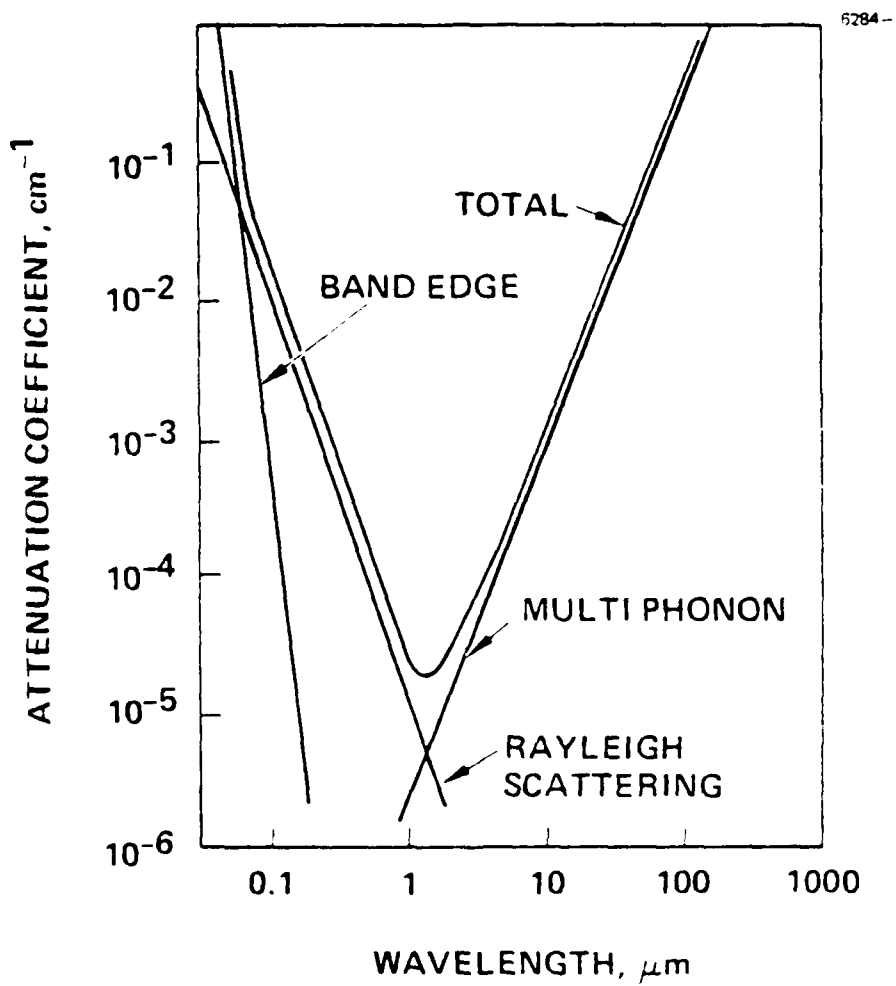


Figure 1.

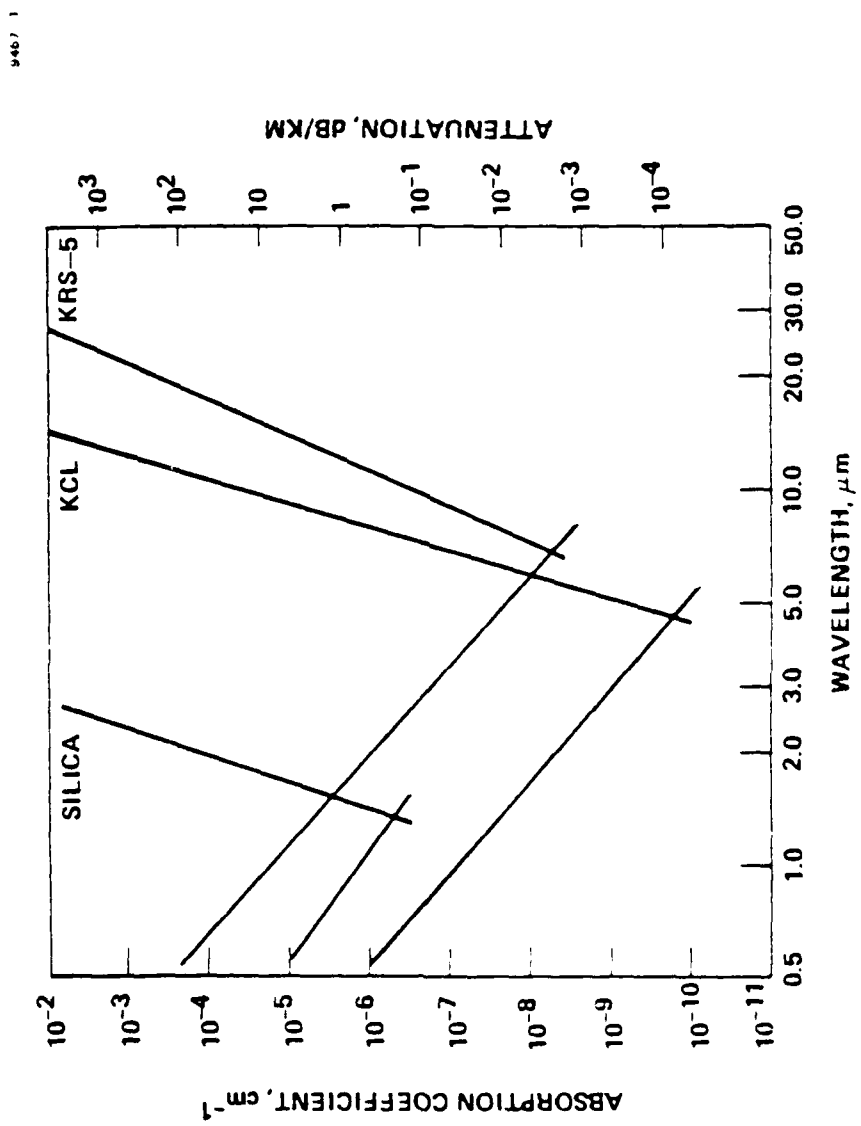


Figure 1.

8864 /

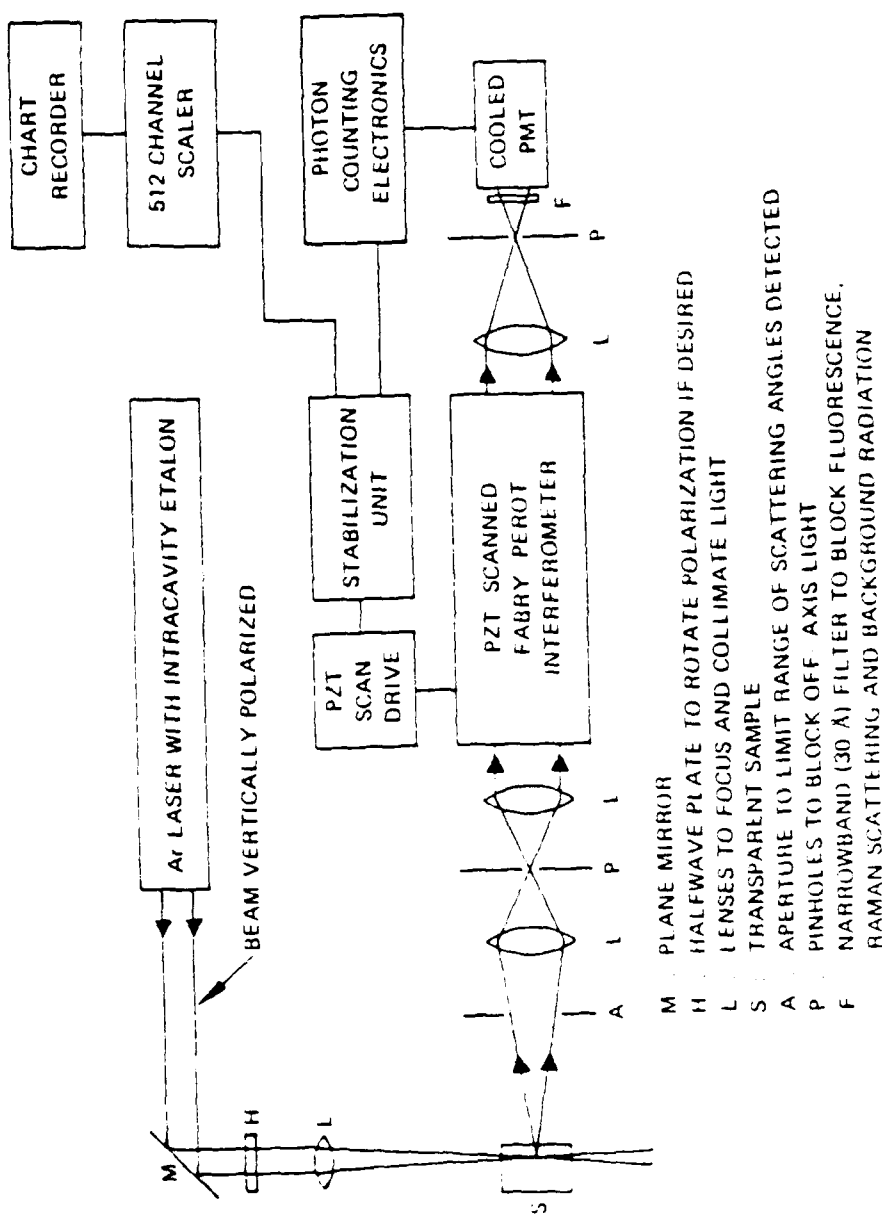


Figure 3.

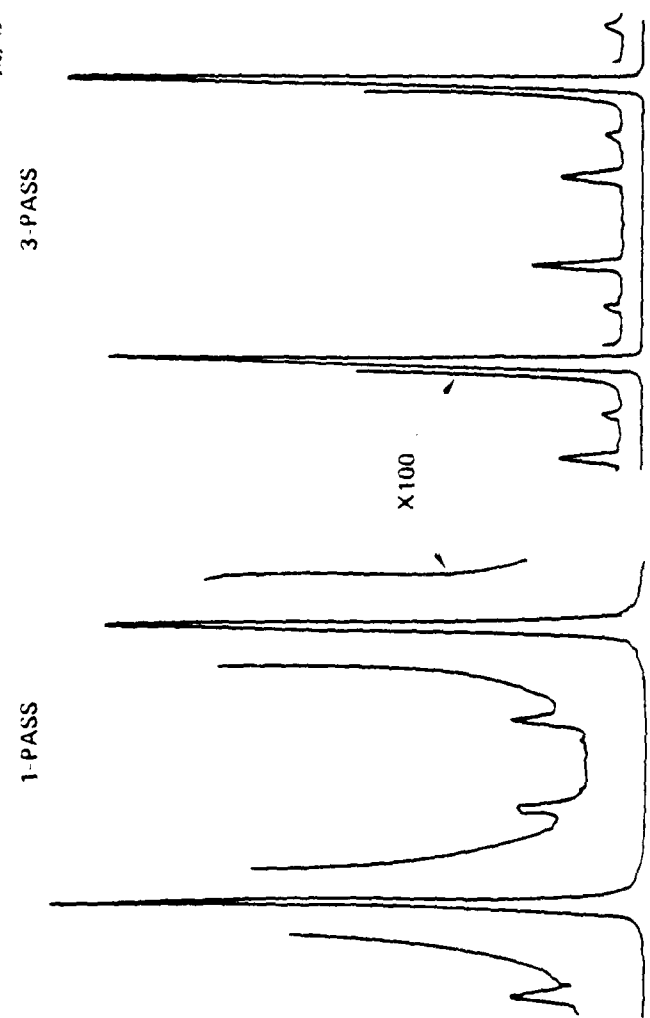
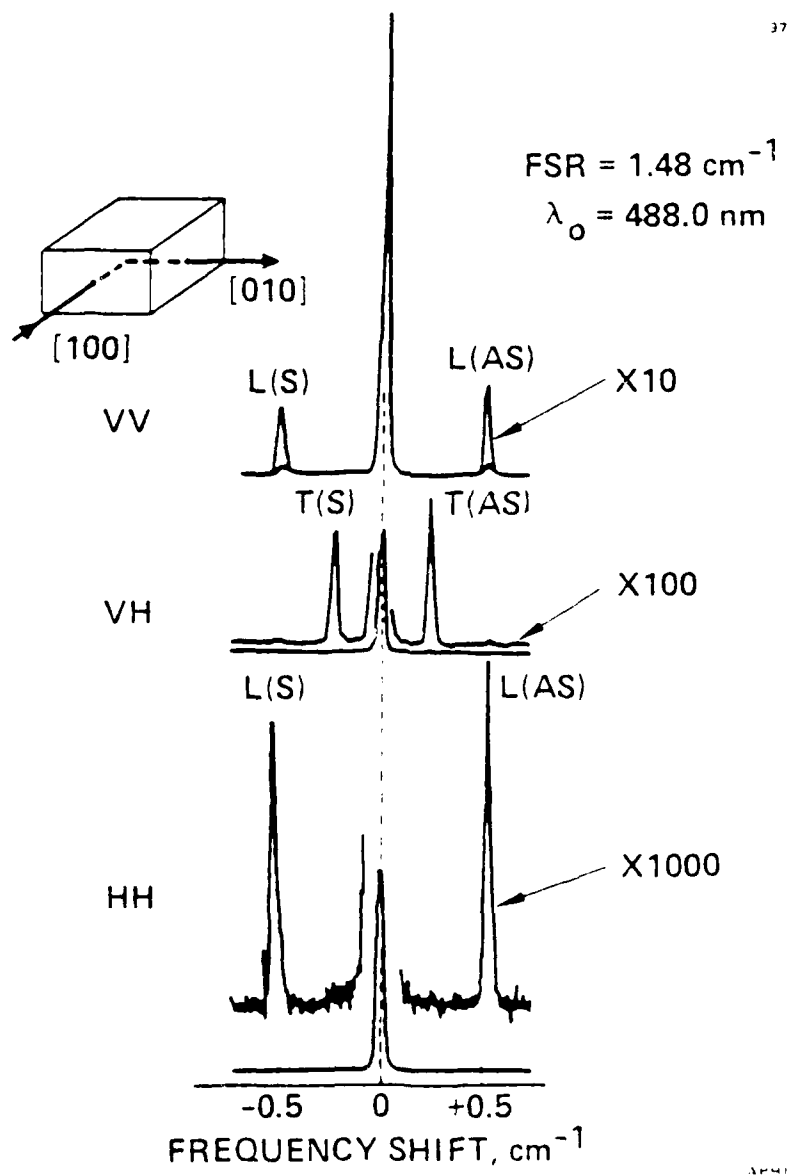
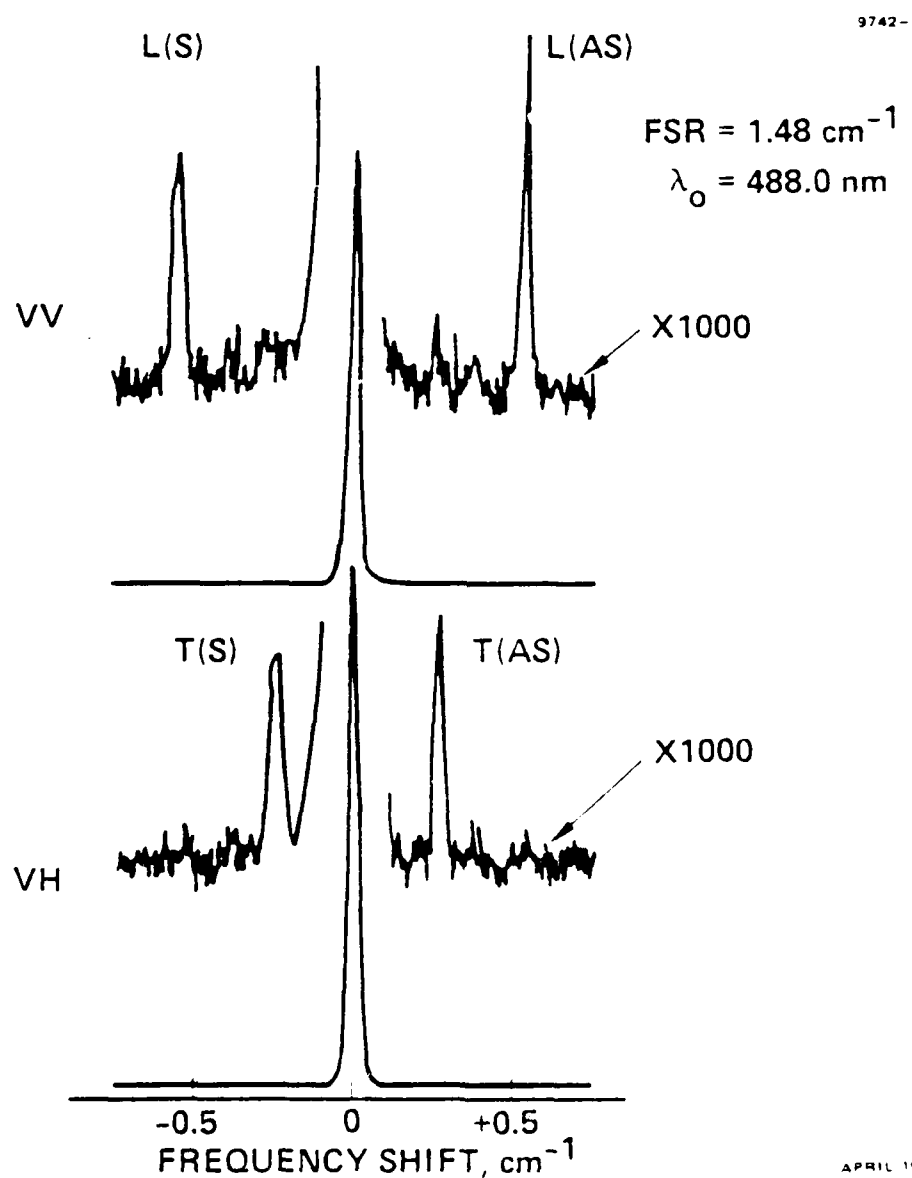


Figure 4.



APRIL 1980

Figure 3.



APRIL 1980

Figure 5.

INFRARED-TRANSPARENT GLASSES DERIVED FROM THE FLUORIDES  
OF ZIRCONIUM, THORIUM, AND BARIUM

M. Robinson, R.C. Pastor, R.R. Turk, D.P. Devor, M. Braunstein  
Hughes Research Laboratories, Malibu, California 90265

R. Braunstein  
Department of Physics  
University of California at Los Angeles, Los Angeles, California 90024

(Received March 24, 1980; Communicated by R. A. Huggins)

ABSTRACT

Glasses consisting solely of high-purity  $ZrF_4$ ,  $ThF_4$ , and  $BaF_2$  have been synthesized using reactive atmosphere processing (RAP) techniques. RAP of the individual components and the molten material with anhydrous HF and  $CCl_4$  is described. The glass molds easily at  $312^\circ C$  and 1920 psi with a high-fidelity replication of the die surface. The glass is water insoluble, unusually hard and strong, and continuously transparent from 0.3 to 7  $\mu m$ .

Introduction

During the past several years, considerable effort has been directed to the preparation of exceptionally high purity halide materials for a multitude of applications ranging from laser windows to fiber optics. RAP has been successfully developed for crystalline  $KCl$  to bring about the reduction in the 10.6- $\mu m$  absorption coefficient from  $\geq 10^{-2} \text{ cm}^{-1}$  (Ref. 1) to  $\leq 10^{-4} \text{ cm}^{-1}$  (Ref. 1). RAP methods increased the rupture strength by one order of magnitude and greatly reduced surface attack by ambient humidity.

RAP, when applied to the single-crystal growth of rare earth fluorides (3), totally eliminated many solid-solid phase transitions thought to be intrinsic to these compounds. The transitions are triggered by low concentrations of  $OH^-$ ; minimizing the  $OH^-$  level by atmosphere control permitted large single crystals ( $> 1 \text{ cm}$ ) to be grown from melts of fluorides previously thought to exhibit di-morphism.

Multicomponent fluorozirconate glasses, a relatively new class of materials, were reported first by M. Chanthanasiw (4) in 1976 and later by Poulain et al. in 1977 (5). Both were concerned with the  $ZrF_4$ - $ThF_4$ - $BaF_2$  system; that system is also the subject of this paper. The preparation technique typically used by earlier workers consisted of reacting highly purified components at 800 to  $900^\circ C$  in an argon atmosphere. The starting materials were contained in a hermetically sealed nickel crucible and the glass was formed by pouring the fully reacted melt into a mold residing in a nitrogen-filled glove box. The vitreous

domain for  $ZrF_4$ - $ThF_4$ - $BaF_2$  can be described as an area of a triangle on the ternary diagram bounded by the following points: 63 mole %  $ZrF_4$ , 15 mole %  $ThF_4$ , and 33 mole %  $BaF_2$ . RAP preparations throughout this area readily yield transparent glasses; however, the composition of interest for this paper is 60%  $ZrF_4$ , 7%  $ThF_4$ , and 33%  $BaF_2$ , which is essentially the center of the vitreous domain.

This paper describes the RAP approach to preparing this fluoride glass utilizing open crucibles and controlled atmospheres of anhydrous HF and  $CCl_4$ . Physical properties including spectral data are given as well as glass molding techniques.

### Experimental

#### Purification of Materials

$ZrF_4$  of 99.5% purity was obtained from the Cerac Company. This raw material was treated with dry HF at 400°C and sublimed once at 900°C in a stainless-steel sublimator. The high-purity, colorless, transparent needles were then combined with  $ThF_4$  and  $BaF_2$  to give the desired ratio - 0.60 Zr: 0.07 Th: 0.33 Ba. The  $ThF_4$  was derived from 99.9%  $ThO_2$  (Cerac). The oxide was first reacted with a 49% HF solution, and then the water was evaporated away at about 100°C until a dry powder resulted. Next, this powder was slowly heated and subjected to gaseous HF until melting occurred. The high-purity product was the source of  $ThF_4$  for glass-forming experiments. The  $BaF_2$ , from EM Laboratories, was 99.99% pure. It was treated with dry HF to 1000°C prior to use as a starting material for glass preparations.

Each glass forming run consisted of a 93-g batch. Vitreous carbon or platinum crucibles were used in an Astro Industries (graphite resistance) furnace. The furnace was vacuum pumped to 300°C before the start of RAP. The reactive atmosphere was either anhydrous HF diluted to 10 mole % with helium, or gaseous  $CCl_4$  (Mailinkrodt AR) diluted with helium. The mixture was heated to 900°C in 5 hr; the resulting melt was soaked for 5 hr and then cooled abruptly to room temperature. The ingot could then be annealed at 120°C to remove strain.

#### Glass Molding

Molding was accomplished with a 10-ton PHI hydraulic press with readable pressure to 2.5 psi intervals. A 1/2-in. cylindrical tungsten carbide die was used. The inner faces of the plungers were polished optically flat to 1.1 fringe (sodium spectral line - 5896 Å). The die with sample inside is placed in the press. The temperature is raised to 312°C and increasing pressure is applied until a pressure drop is indicated due to glass flow. Temperature is held constant until the die is filled as indicated by no further pressure drop even as higher pressure is applied. The temperature is then lowered below 300°C, the pressure is released, and the sample is cooled to room temperature.

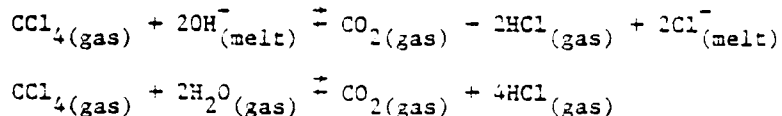
### Results and Discussion

#### Glass Properties

Early batches of 0.60  $ZrF_4$ :0.07  $ThF_4$ :0.33  $BaF_2$  glass were prepared exclusively with a RA consisting of HF diluted with helium. Although X-ray powder pattern showed that the specimens were indeed glassy, they appeared to consist of two phases - a primary transparent-colorless phase and a relatively small quantity of an opaque-black phase. Electron microprobe analysis of the samples

indicated that the opaque-black substance contained only one-half the fluorine of the transparent phase. This fluoride-deficient phase formed regardless of whether a platinum or carbon crucible was used, and, surprisingly, its concentration appeared to increase with longer HF soak times.

The formation mechanism of this opaque-black phase is not understood; it would appear to result from the dissociation of  $ZrF_4$ . Figure 1 shows the IR transmission curves (Beckman IR 12) of three fluoride glass samples. Curve A is for the glass 0.60  $ZrF_4$ :0.10  $ThF_4$ :0.30  $BaF_2$ . This glass is manufactured in France by La Verre Fluore and, using an inert atmosphere, is prepared with careful attention to the prevention of hydrolysis. The absorption centered at about 2.35  $\mu$ m may be the result of a trifling amount of  $OH^-$  contamination. Curve B results from a HF-prepared glass, 0.60  $ZrF_4$ :0.07  $ThF_4$ :0.33  $BaF_2$ . This specimen appears to have even a higher concentration of  $OH^-$  than does A. HF is not an effective reactive atmosphere for these glasses. It can displace  $OH^-$  and  $O^-$  from simple mixtures of  $BaF_2$  and  $ThF_4$ , but, at temperatures above 530°C,  $ZrO_2$  resists conversion to  $ZrF_4$  (i.e.,  $ZrO_2$  is thermodynamically favored over  $ZrF_4$  even in the presence of HF).  $OH^-$  impurity arises from hydrolysis stemming from water emanating from the interior surfaces of the furnace, and HF of course cannot eliminate this water. The reduced transmission throughput is caused by some precipitated fluoride deficient base. Curve C is 0.60  $ZrF_4$ :0.07  $ThF_4$ :0.33  $BaF_2$  glass prepared in a  $CCl_4$  atmosphere. Note that the transmission is continuous.  $CCl_4$  is an extremely effective reactive atmosphere. It reacts with both  $OH^-$  in the melt and outgassed water:



Moreover,  $CCl_4$  pyrolytically cracks at temperatures above 400°C to give nascent chlorine, which compensates any fluoride deficiency and yields remarkably colorless and transparent ingots.

The absorption coefficients of sapphire, Le Verre Fluore glass, and Hughes fluorozirconate glass are compared as a function of wavelength in Figure 1. The measurements, made with a Cary Model 14R, show the Hughes glass ( $CCl_4$  prepared) to be less absorbing than the Le Verre Fluore, but not nearly as good as sapphire. Fluorozirconate glass prepared in anhydrous HF gives about the same result as Le Verre Fluore glass. The physical properties of the glass 0.60  $ZrF_4$ :0.07  $ThF_4$ :0.33  $BaF_2$  prepared in  $CCl_4$  are given in Table I. The glass transition, crystallization, and fusion temperatures were determined for a sample sealed at room temperature in a platinum capsule at a pressure of  $<10^{-3}$  Torr. Water insolubility was determined by soaking typical glass samples in tap water for 14 hr at room temperature and observing no weight change.

#### Molded Glass

Figure 3 shows the fluorozirconate glass (prepared in  $CCl_4$ ) and the die before and after hot pressing. Pressing was done at 312°C and 1920 psi in air. Note the frosty areas corresponding to flat cut corner bevels on the original blank. Total height reduction was 31.2% - from 0.213 in. to 0.150 in.

Residual gas analysis of crystalline  $ZrF_4$  shows the evolution of fluorine at  $T \geq 500^\circ C$ , i.e., (white)  $ZrF_4 \rightleftharpoons$  (black)  $ZrF_2 + F_2$ .

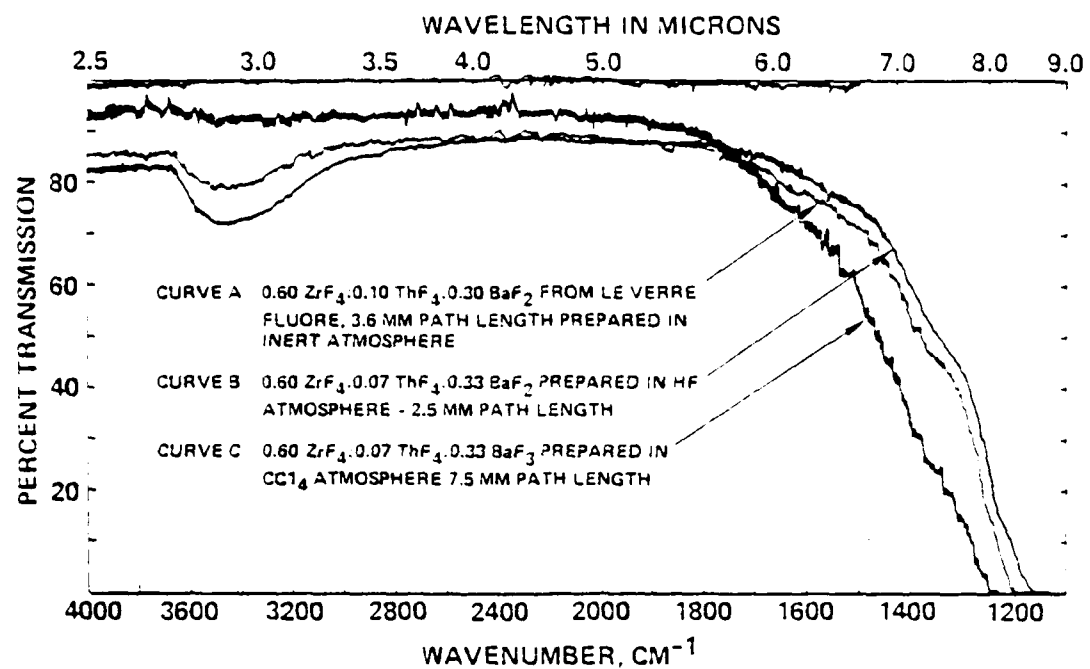


FIG. 1  
Transmission spectra of fluorozirconate glasses. Both faces polished to a window finish for all samples.

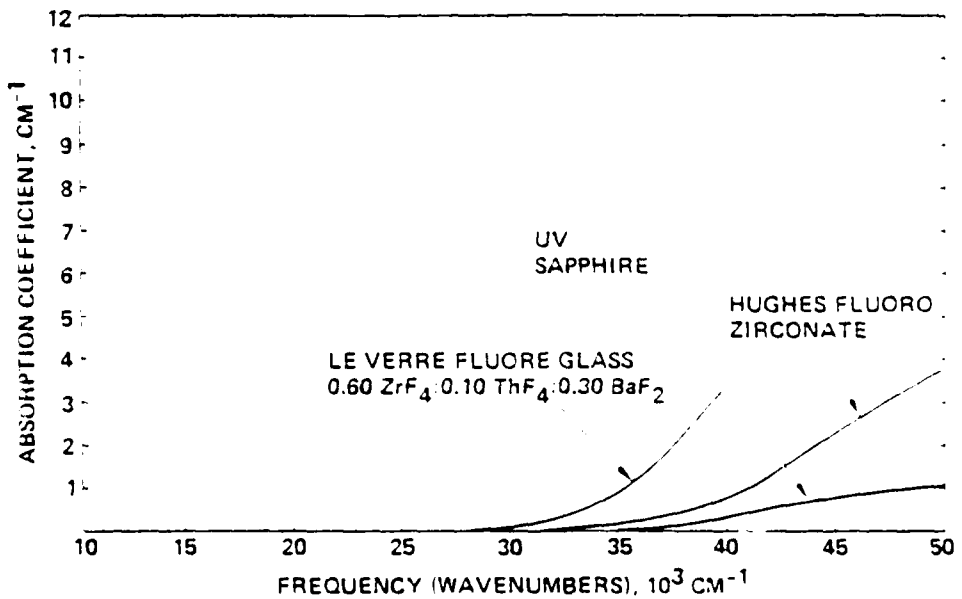


FIG. 2  
UV absorption coefficient of uv grade sapphire, Le Verre Fluore and Hughes fluorozirconate glass (prepared in CCl<sub>4</sub> atmosphere).

TABLE 1  
 Physical Properties of 0.60  $ZrF_4$ :0.07  $ThF_4$ :0.33  $BaF_2$  Glass  
 (Prepared in  $CCl_4$  Atmosphere)

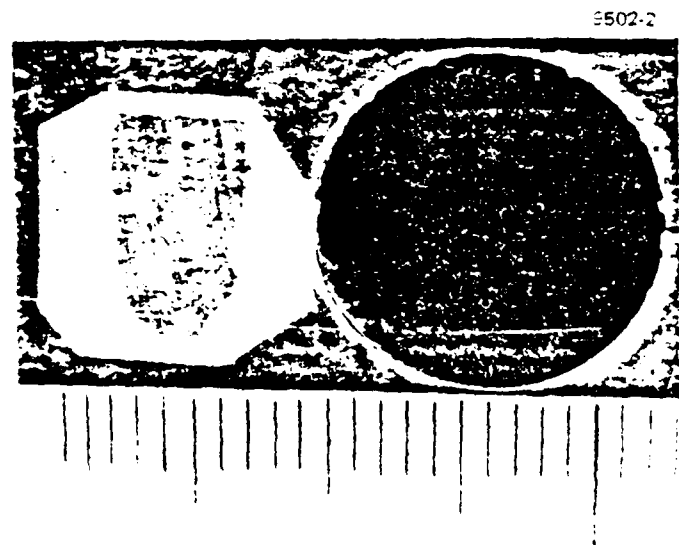
Properties	Values
Optical transparency	0.3 $\mu m$ UV to 7 $\mu m$ IR <sup>a</sup>
Density	4.8 $g/cm^3$
Glass transition temperature <sup>d</sup>	295°C
Crystallization temperature <sup>d</sup>	390°C
Fusion temperature <sup>d</sup>	485°C
Refractive index ( $n_D$ )	1.53
Knoop hardness <sup>b</sup> ( $Kg-mm^{-2}$ )	250
Humidity effects	Water insoluble
Heat capacity ( $C_p$ ) at 45°C <sup>d</sup>	0.511 J/g-°C
Coefficient of linear expansion <sup>d</sup>	
30 to 60°C	$4.3 \times 10^{-6}/^{\circ}C$
250 to 270°C	$13.3 \times 10^{-6}/^{\circ}C$
Rupture strength <sup>c</sup>	35,300 psi
Absorption coefficient at HF laser wavelength (2.8 $\mu m$ )	$6 \times 10^{-3} cm^{-1}$
Absorption coefficient at DF laser wavelength (3.3 $\mu m$ )	$2 \times 10^{-3} cm^{-1}$

<sup>a</sup>Prior art fluoride glass shows a strong absorption at 2.35  $\mu m$ .

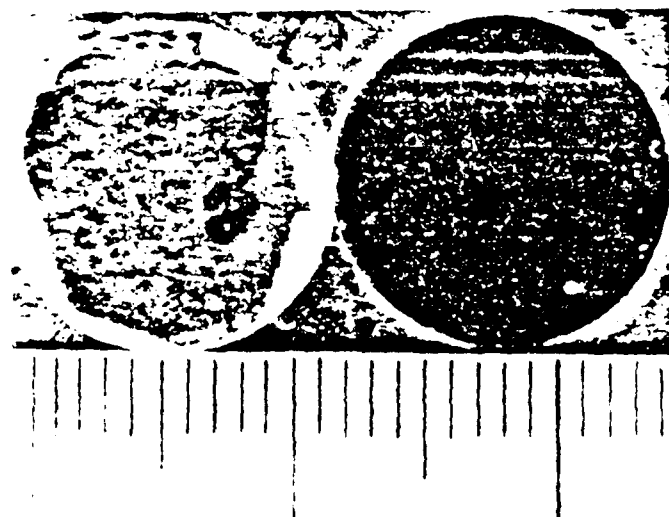
<sup>b</sup>Single crystal calcium fluoride ( $CaF_2$ ) is 155.

<sup>c</sup>Forged  $CaF_2$  is 14,000 psi.

<sup>d</sup>Measured with DuPont thermal analyzer model 1090.

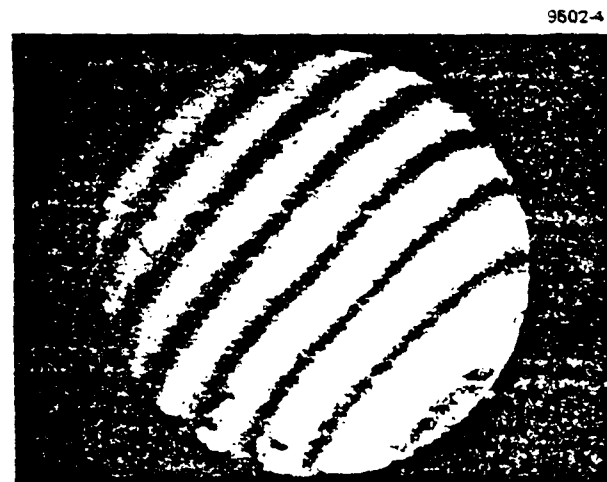


(a) SAMPLE AND DIE  
BEFORE PRESSING

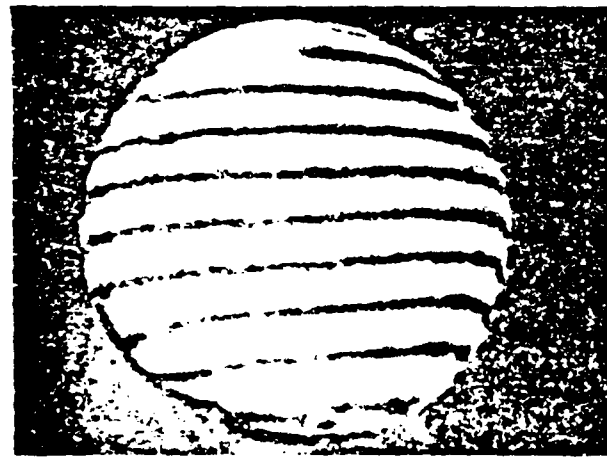


(b) SAMPLE AND DIE  
AFTER PRESSING

FIG. 3  
Hot pressed 0.90 ZrF<sub>4</sub>0.07 ThF<sub>4</sub>0.03 BaF<sub>2</sub>  
glass prepared in  $\text{CO}_2$  atmosphere.



(a) FACE OF DIE PLUNGER



(b) FACE OF PRESSED GLASS

FIG. 4  
Hot pressed 0.60  $\text{ZrF}_4$ :0.07  $\text{ThF}_4$ :0.33  $\text{BaF}_2$  glass (prepared in  $\text{CCl}_4$  atmosphere). Both surfaces photographed in sodium light while contacting a 1.00" optical reference flat.

Figure 4(a) shows the flatness of the die plunger to be about 1/2 fringe of sodium light (5896 Å/4). Figure 4(b) shows that the molded glass surface closely duplicates the die surface.

#### Summary

The key to maximizing IR transparency and mechanical strength for these halide glasses lies in eliminating anionic impurities such as  $\text{OH}^-$  and  $\text{O}^2-$  which enter the condensed phase through hydrolysis during the mixing and melting stages of preparation. The HF scrubbing is not effective in this case. HF will not react with outgassed water emanating from the furnace interior, and, at elevated temperatures, it will not react with  $\text{ZrO}_2$  to yield  $\text{ZrF}_4$ . Moreover, the use of HF appears to promote significant quantities of a black, fluoride-deficient phase.  $\text{CCl}_4$ , on the other hand, eliminates oxygen-containing species by reacting both with atmospheric water and with oxygen species in the melt.

Furthermore, utilization of  $\text{CCl}_4$  for scrubbing compensates fluoride deficiency by adding  $\text{Cl}^-$  to the  $\text{F}^-$  vacancies. Fluoride glass prepared with the benefit of  $\text{CCl}_4$  RAP is continuously transparent from 0.3  $\mu\text{m}$  to 0.7  $\mu\text{m}$ , is unusually hard and strong, and can be easily molded at moderate temperature and pressure.

#### Acknowledgments

The authors are grateful for the assistance of the following colleagues: A.C. Pastor and M.B. Klein of this laboratory, who gave considerable time in helpful discussions, J.A. Harrington performed the calorimetric absorptions at HF and DF laser wavelengths, R. Wong-Quen and R. Chew supplied the IR transmission data, and K.T. Miller and A. Timper carried out X-ray determinations on starting materials and final products.

#### References

1. F. Horrigan, C. Klein, R. Rudko, and D. Wilson, *Microwaves* 3, 68 (1969).
2. R.C. Pastor and A.C. Pastor, *Mat. Res. Bull.* 10, 117 (1975).
3. R.C. Pastor and M. Robinson, *Mat. Res. Bull.* 9, 569 (1974).
4. M. Chanthanasinh, Doctoral Thesis, University of Rennes (France) July (1976).
5. M. Poulaing, M. Chanthanasinh, and J. Lucas, *Mat. Res. Bull.* 12, 151 (1977).

## High-Desert Book

Site 100 181

Infrared transparent glasses refined from barium fluoride

J. Robinson, R.C. Pastor, R.R. Park, D.R. Devor, and M. Braunstein

Hughes Research Laboratories  
3011 Malibu Canyon Road, Malibu, California 90265

R. Braumstein

Department of Physics, UCLA  
Los Angeles, California 90024

### Abstract

A new family of glasses derived from hafnium fluoride ( $HfF_4$ ), carbon tetrifluoride ( $CaF_4$ ), and various rare earth fluorides has been studied. The spectral and thermal properties are given, as well as hardness, melt strength, and coefficients of expansion. Reactive atmosphere processing (RAP) of the individual components and the molten glass with anhydrous  $CF_4$ ,  $BF_3$ , HF and  $CaF_2$  are described. RAP eliminates anionic impurities such as  $H^+$  and  $O^{\bullet}$  which enter the condensed phase through hydrolysis during the melting and mixing stages of preparation. Elimination of these impurities through RAP maximizes IR transparency and mechanical strength. The glasses are resistant to room temperature hydrolysis, are hard and strong, and are continuous transparent from 0.2  $\mu m$  to 9  $\mu m$ .

## Introduction

Fluoride glasses synthesized from the  $\text{ErF}_3\text{-BaF}_2$  (CB) and  $\text{HfF}_4\text{-BaF}_2$  (HB) systems are relatively new. Glasses based on CB were first reported by M. Chantaisinh and later by Poulin et al.,<sup>1</sup> and Bendow et al.<sup>2</sup> These CB glasses when prepared by reactive atmosphere processing (RAP) technique<sup>3</sup> are continuously transparent from 0.3  $\mu\text{m}$  to 1  $\mu\text{m}$ , ir quite hard and strong, and generally resistant to attack by environmental moisture.

A great need exists for rugged, infrared-transparent glasses capable of being inexpensively fabricated into fiber optic elements, and optical components such as laser hosts, windows, prisms, and Faraday windows. Crystalline materials are, of course, known that are transparent in the IR portion of the spectrum. These materials, that include  $\text{ZnS}$ ,  $\text{NaCl}$ , and  $\text{KCl}$  are difficult to fabricate inexpensively since they are either not readily castable or moldable into a variety of sizes and shapes, or they are quite readily attacked by ambient humidity. In oxide glasses, oxygen vibrational modes limit IR transmission to wavelengths shorter than  $4 \mu$ .  $\text{LB}$  and  $\text{RB}$  glasses have enormous potential as low-loss infrared glasses, including all the infrared wavelengths silica glass has in the visible region of the spectrum. The key to maximizing IR transparency and mechanical strength for these glasses lies in eliminating the intrinsic impurities such as  $\text{Al}^{3+}$  and  $\text{Fe}^{2+}$  that enter the glassed glass through hydrolysis during the melting and mixing stage of preparation. This stage of preparation is perhaps the most critical since the highest working temperatures are now used and chemical gradients are large. Yet, other investigators often neglect optimization of materials necessary to achieve maximum purity at this stage by chemical manipulation of the solid phase via the melting and casting stage. We will this chemical manipulation reactive atmospheric processing (PAP), and also show that greater transparency and optimization of a variety of saline materials ranging from  $\text{LiCl}$  to single crystal rare earth sulfides, and  $\text{LB}$  and  $\text{RB}$  glasses, glasses based on the  $\text{LB}$  system will be discussed in terms of their infrared properties at 11. In reference 6, and are the subject of this paper.

The extrinsic domain for both dB and TB systems is virtually the same, and is represented by the area of the triangle shown in Figure 1. RAP gels prepared over the range of this region will yield transparent gels, and extractions of  $10^{-10}$  mole TB will be well within the range of the RAP gel. The two sets of higher scaling rates are employed. The composition of the test buffer is the same as the extrinsic domain, i.e., HEP, 1% SDS, and 1% Triton. Each with dilutions of 10, 100, 1000, and 10000. For all or part of the TLE, with no apparent change in the size of glass formation, it has been suggested that RAP gels can be prepared with 1% SDS and 1% Triton. This is in agreement with the spectral data for this relatively new extrinsic system.

### Experiment 11

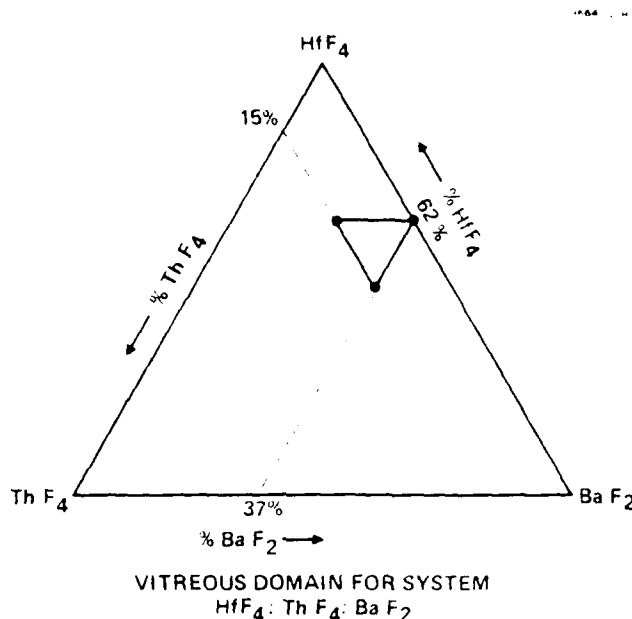
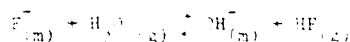


Figure 1. Vitreous domain for system HfF<sub>4</sub>:ThF<sub>4</sub>:BaF<sub>2</sub>.

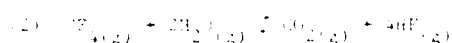
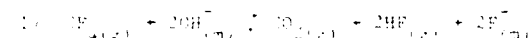
with helium or gaseous HCl (Mallinckrodt AR) diluted with helium. The mixture was heated to 600°C in 1 hr, the resulting melt was cooled for 1 hr and then cooled abruptly to room temperature. The ingot could then be annealed at 250°C to relieve strain.

#### Results and Discussion

It is a well known fact that for fluoride melts, hydroxide contamination readily occurs. It can be written as follows:



where m = melt, g = gas. OH<sup>·</sup> may be considered a pseudo fluoride since it is quite similar to F<sup>·</sup> in both size and electronegativity. F has an electronegativity value of 4.0, OH = 3.1, and ionic radius of 1.33 Å, OH<sup>·</sup> = 1.41 Å. The OH<sup>·</sup> contamination may be removed partially by supplying HF, a primary RAP agent, to crust the melt, and can be removed further by a secondary RAP agent such as HF<sub>2</sub>, which reacts with OH<sup>·</sup>. In it, unlike HF, it can react with OH<sup>·</sup> in the atmosphere surrounding the melt.



In the past, utilization of dual reactive atmospheres HF and F<sub>2</sub> or SF<sub>6</sub> and SF<sub>4</sub> has been attempted in melt with (HF<sub>2</sub>), (HF<sub>2</sub>), F<sup>·</sup>, etc.

Such high purity materials are higher melting, harder, and show better UV transparency than the standard stoichiometric fluoride materials. However, such standard techniques are not appropriate to this system. Some modifications have to be made for the following reasons:

1. HF is not an effective RAP since HfF<sub>4</sub> not HfF<sub>2</sub> is thermodynamically stable in an atmosphere of temperatures greater than 1273°C.
2. glass anneals or soaks with a pure HF atmosphere or with HF-F<sub>2</sub> or HF-SF<sub>6</sub> atmosphere contact small quantities of an opaque black material which is a chlorine deficient fluoride containing a lot of the fluorine compared to the transparent glass.
3. The amount of the black phase increases with HF concentration in the atmosphere.

Although the formation of the black chlorine deficient phase is not understood or clearly understood, it is known to dissociate at 1000°C, i.e., HF<sub>2</sub> → 1/2HF<sub>2</sub> + 1/2Cl<sub>2</sub>. Positional analysis of the melt by XRD shows the evolution of chlorine at 1000°C, i.e., white "HF<sub>2</sub>" phase. The evolution of chlorine is due to the dissociation of HF<sub>2</sub> at 1000°C. The chlorine is extremely effective in the formation of the black phase.

$\text{H}_2$  in the melt and outgassed  $\text{H}_2$  is shown in Figs. 1 and 2 above, but it first tends to decompose at the melting temperature,  $T_m$ , to give nascent chlorine  $\text{Cl}_2$ .  $\text{Cl}_2$ , a strong oxidizing agent, then reacts with the glass absorbing species by the formation of  $\text{HfF}_6-\text{Cl}_2$ ,  $\text{Hf}_x$ , where  $x$  is small. Utilization of the chlorine yields AB glass specimens of remarkably high transparency. The absorption coefficients,  $\alpha$ , made on quartz, Le Verre Fluore glass (a commercial J3 glass) and Hughes Fluorohafnate glass (a 0.60  $\text{ZrF}_4$ :0.10  $\text{ThF}_4$ :0.30  $\text{BaF}_2$  glass) are given in Figure 1. The measurements made with a Cary model 142 spectrophotometer show that the Hughes glass is less absorbing than Le Verre Fluore glass (0.60  $\text{ZrF}_4$ :0.10  $\text{ThF}_4$ :0.30  $\text{BaF}_2$ ) and quartz is the most transparent.

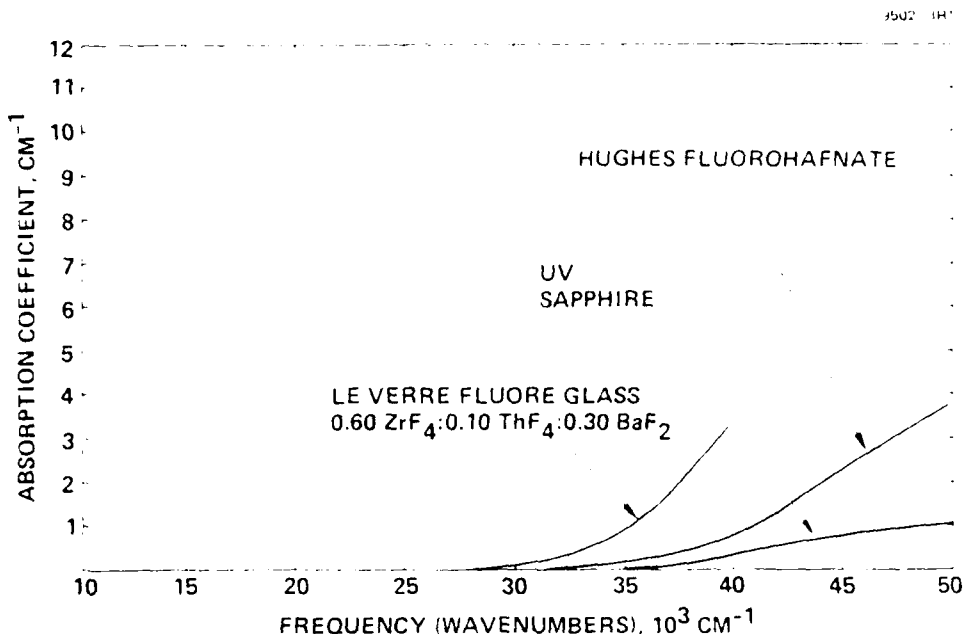


Figure 1. UV absorption coefficient of UV-grade sapphire, Le Verre Fluore and Hughes Fluorohafnate glass (prepared in  $\text{Cl}_2$  atmosphere).

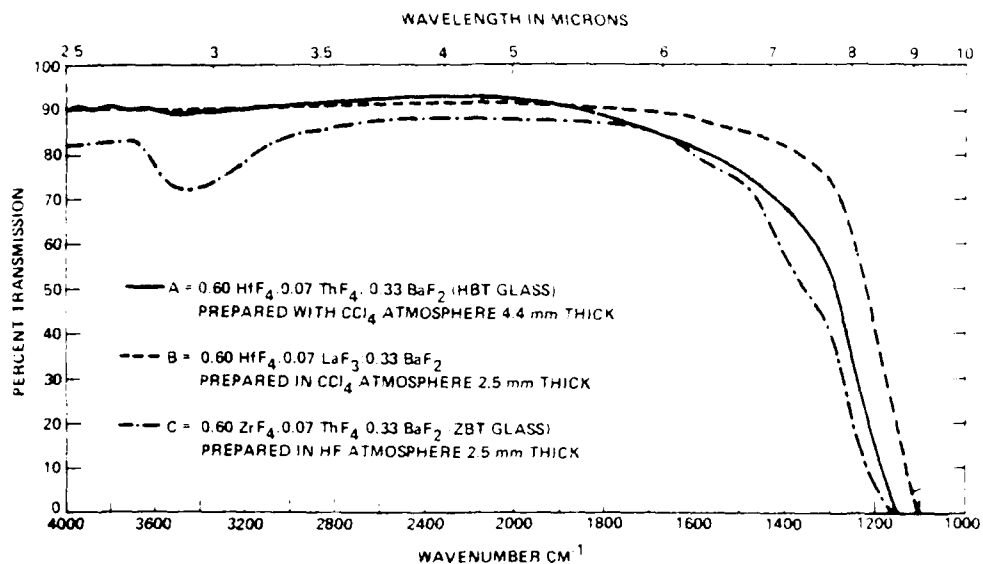
Figure 2 shows the IR transmission curves (Beckman IR 12) of three fluoride glasses. All are 0.60  $\text{ZrF}_4$ :0.10  $\text{ThF}_4$ :0.30  $\text{BaF}_2$  (ABT). This glass was prepared in a  $\text{Cl}_2/\text{H}_2$  atmosphere and allowed to cool from the melting temperature to room temperature in helium. Its transparency extends continuously from the lower limit of 10,000  $\text{cm}^{-1}$  to approximately 4,000  $\text{cm}^{-1}$ . Figure 3 is for the glass 0.60  $\text{HfF}_6$ :0.10  $\text{BaF}_2$  which contains a large proportion of the active component  $\text{HfF}_6$  and shows the same general features as the ABT glass. The absorption coefficient,  $\alpha$ , made on Hughes glass, 0.60  $\text{ZrF}_4$ :0.10  $\text{ThF}_4$ :0.30  $\text{BaF}_2$ , shows absorption curves in a semicircular pattern at 3,000  $\text{cm}^{-1}$  which is caused by a small amount of  $\text{HfF}_6$  contamination. The curves are as expected for  $\text{HfF}_6$ . Simply stated,  $\text{HfF}_6$  is not an effective IR absorber in this glass, but it is in mixed fluoride  $\text{H}_2$  flame mixtures of  $\text{HfF}_6$ - $\text{BaF}_2$ , but at temperatures above 1,700°C and a pressure of 100 atm.  $\text{HfF}_6$  decomposes to form  $\text{HfF}_4$  which is very easily absorbed over  $\text{HfF}_6$ , even in the presence of  $\text{HfF}_6$ . The infrared transmission curves of the ABT glass absorption arises from absorption resulting from absorption of the  $\text{HfF}_6$  component of the surface and is also readily reflected in the Hughes glass. The absorption coefficient in the range 3,000-4,000  $\text{cm}^{-1}$  is higher on some precipitated glass and lower on others.

A comparison of the optical properties of ABT and AB glass is given in Table 1. The longer  $\lambda_m$  and the  $\lambda_m$  to  $\lambda_{1/2}$  integrated ratio  $\lambda_m/\lambda_{1/2}$  has nearly twice the mass in  $\text{HfF}_6$ . Figure 4 shows a thermogravimetric analysis of an ABT thermoinstability. The glass transition,  $T_g$ , crystallization,  $T_c$ , and the softening temperature,  $T_s$ , are 400°, 450°, and 500°, respectively, significantly higher than ABT thermoinstability.

Figure 5 is a photograph of various polished AB and AB glass specimens. The central specimen is a 1.5 mm  $\times$  1.5 mm  $\times$  0.5 mm ABT glass prepared in  $\text{Cl}_2/\text{H}_2$ . The opaque specimen on the left is a 1.5 mm  $\times$  1.5 mm  $\times$  0.5 mm AB glass which is heavily contaminated with the fluorine precipitated glass shown in Figure 3. The irregular shaped sample at the bottom is a 0.5 mm  $\times$  0.5 mm  $\times$  0.5 mm ABT glass specimen which is the first supervisual ABT specimen starting with  $\text{HfF}_6$ . The three rectangular samples on the right are AB glass specimens starting with  $\text{HfF}_6$ .

#### Summary

ABT and AB glass are made from high purity starting materials, which are relatively inexpensive, and are relatively transparent. ABT glass is thermally stable, has a low softening temperature, and is relatively transparent. AB glass is thermally stable, has a low softening temperature, and is relatively transparent. ABT glass is relatively transparent, but AB glass is not. ABT glass is relatively transparent, but AB glass is not.



BOTH FACES POLISHED TO A WINDOW FINISH FOR ALL SAMPLES

Figure 3. Transmission spectra of fluoride glasses  
(Prepared in  $\text{CCl}_4$  atmosphere).

Table 1. Physical Properties of 0.60  $\text{ZrF}_4$ , 0.07  $\text{ThF}_4$ , 0.33  $\text{BaF}_2$  (ZBT) and 0.60  $\text{HfF}_4$ , 0.07  $\text{ThF}_4$ , 0.33  $\text{BaF}_2$  (HBT) Both Prepared in  $\text{CCl}_4$  Atmosphere

Properties	Values	
	ZBT	HBT
Optical transparency	1.0 mm $\text{Hg}^{-1}$ $\text{cm}^{-1}$ mm thick	1.0 mm $\text{Hg}^{-1}$ $\text{cm}^{-1}$ mm thick
Density	4.3 g./cm. <sup>3</sup>	4.3 g./cm. <sup>3</sup>
Glass transition temperature <sup>1</sup>	200°C	200°C
Crystallization temperature <sup>2</sup>	400°C	400°C
Fusion temperature <sup>3</sup>	800°C	800°C
Refractive index $n_{25}$	1.7	1.7
Snoop hardness (Kg-mm) <sup>4</sup>	250	250
Humidity effects	Water insoluble	Water insoluble
Heat capacity (Cal. at 4°C) <sup>5</sup>	1.31 $\text{J} \cdot \text{g}^{-1} \cdot \text{°C}^{-1}$	1.43 $\text{J} \cdot \text{g}^{-1} \cdot \text{°C}^{-1}$
Coefficient of linear expansion <sup>6</sup>		
0 to 200°C	$1.1 \times 10^{-5} \text{ cm/cm}$	$1.1 \times 10^{-5} \text{ cm/cm}$
0 to 250°C	$1.15 \times 10^{-5} \text{ cm}$	$1.15 \times 10^{-5} \text{ cm}$
Capture strength	1.1, 30 psi	1.1, 30 psi
Absorption coefficient at 4F	$6 \times 10^{-3} \text{ cm}^{-1}$	
Laser wavelength 1.06 $\mu\text{m}$		
Absorption coefficient at 4F	$2 \times 10^{-3} \text{ cm}^{-1}$	
Laser wavelength 1.06 $\mu\text{m}$		

<sup>1</sup> Prior art fluoride glass shows a strong absorption at 1.8  $\mu\text{m}$ .

<sup>2</sup> Single crystal zirconium fluoride is 100°.

<sup>3</sup> An isolated previous measurement gave 10,000 psi.

<sup>4</sup> Measured with Brinell thermal analyzer model 1-90.

<sup>5</sup> Indirect samples show surface transmission after 1000 experiments at relative humidity at room temperature.

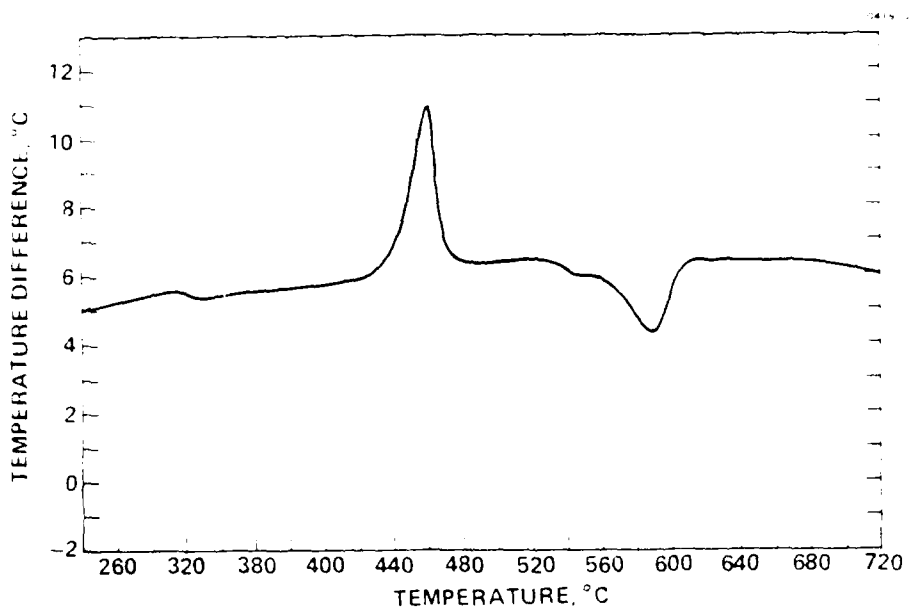


Figure 4. Thermogram of HBT glass (0.50 HF, 0.17 TiF<sub>4</sub>, 0.33 BaF<sub>2</sub>).

INFRARED-TRANSPARENT GLASSES DERIVED FROM  
COMBINATIONS OF ZIRCONIUM, THORIUM, AND BARIUM  
FLUORIDES

M. Pastore, D. R. Pastore, R. Turk, D. L. Devor, M. Braunstein  
and R. A. Huggins  
Research Laboratories, Malibu, California 90265  
R. Braunstein  
Department of Physics  
University of California at Los Angeles, Los Angeles, California 90024

(Received March 24, 1967; Communicated by R. A. Huggins)

TRACT

Glasses consisting solely of high-purity ZrF<sub>4</sub>, TiF<sub>4</sub>, and BaF<sub>2</sub> have been synthesized using reactive atmosphere processing (RAP) techniques. RAP of the individual components and the molten material with anhydrous HF and CCl<sub>4</sub> in a dead bed. The glass molds easily at 312°C and 1900 psi with a high-pressure replication of the die surface. The glass is water insoluble, unusually hard and strong, and continuously transparent from 0.3 to 7 μm.

Introduction

During the past several years, considerable effort has been directed to

glass is quite hard and strong, and shows potential application for a wide variety of optical components, such as lenses, laser windows, laser hosts, and fiber optics.

Acknowledgments

The authors are grateful for the assistance of the following colleagues: J.A. Harrington performed the calorimetric measurements at 10F and 10F laser wavelengths, and K.F. Miller and A. Timmer carried out X-ray measurements on starting materials and final glass products.

References

1. M. Chanchanasarn, "Synthèse de nouveaux verres fluorescents à base de tétrafluorure de zirconium. Caractérisation et études spectroscopiques," doctoral thesis, University of Rennes (France), July 1976.
2. M. Poulian et al., "Nouveaux verres fluorescents," Mat. Res. Bull. 12, 191 (1977).
3. M.G. Drexhage, C.J. Moynihan, M. Salen Boulos, and K.P. Quinlan, "Fluoride glasses for visible to mid-IR guided wave optics," to be published in Proceedings of the Conference on Physics of Fiber optics, American Ceramic Soc., Apr 1980.
4. B. Bendow, M. Drexhage, and H. Lipson, "Infrared absorption in highly transparent fluorozirconate glass," J. Appl. Phys., submitted for publication.
5. M. Robinson, R.C. Bastor, R.R. Turk, M. Braunstein, and R. Braunstein, "Infrared transparent glasses derived from the fluorides of Sr, Th, and Ba," Mat. Res. Bull. 15, 735 (1980).
6. M.G. Drexhage, B. Bendow, and C. Moynihan, "IR-Transmitting fluoride glasses," Laser Focus, Oct. 1980.

Optical Properties of the Surface Plasmon of n+ Silicon\*

P. F. Robusto<sup>+</sup> and R. Braunstein<sup>+</sup>

Department of Physics, University of California, Los Angeles, California 90024

The optical properties of the surface plasmon of n+ silicon were determined by a least squares curve fit of the Drude intra-band model to the ATR reflection spectra. The surface plasmon resonance of n+ silicon is highly damped ( $\omega_p \tau = 2.69$ ), and causes the ATR dispersion curve calculated on the real frequency axis to exhibit backbending for its complex frequency-like solutions; whereas, the theoretical dispersion curve exhibits the standard wavevector divergence at the surface plasmon frequency. This discrepancy is rectified by converting the optical properties of n+ silicon into functions of complex frequency, and using them to calculate the ATR dispersion curve in the complex frequency plane. A comparison of the Drude dielectric function as a function of real and complex frequencies was analyzed. The comparison shows that the difference between their values is small at high frequencies and deviate the largest in the region near the surface plasmon resonance.

# Optische Messungen des Oberflächen-Plasmons von n+Silizium\*

P. F. Robusto<sup>+</sup> und R. Braunstein<sup>+</sup>

Physik-Abteilung, University of California, Los Angeles, California 90024

Die optischen Eigenschaften des Oberflächen-Plasmons von n+Silizium wurden festgelegt, indem für das Drude Intraband-Modell die Methode der kleinsten Quadrate für das Verfahren der stochastischen Kurvenermittlung an die abgeschwächten Totalreflexions-Spektra Anwendung fand. Die Oberflächen-Plasmonresonanz von n+Silizium ist stark gedämpft ( $\omega_p \tau = 2,69$ ), und bewirkt, daß die auf der wirklichen Frequenzachse berechnete, abgeschwächte Totalreflexions-Dispersionskurve Zurückbiegung für deren komplexe frequenzartige Lösungen aufweist, wohingegen die theoretische Dispersionskurve die Standard-Wellenvektor-Divergenz bei der Oberflächen-Plasmonfrequenz aufweist. Diese Unstimmigkeit wird korrigiert, indem die optischen Eigenschaften von n+ Silizium in Funktionen komplexer Frequenz umgewandelt werden, und indem diese benutzt werden, um die Kurve der abgeschwächten Totalreflexion in der Ebene der komplexen Frequenz zu berechnen. Ein Vergleich der dielektrischen Funktion nach Drude in Abhängigkeit von wirklichen und komplexen Frequenzen wurde analysiert. Der Vergleich ergab, daß der Unterschied zwischen den Werten bei hohen Frequenzen niedrig ist und daß die Werte am meisten im Bereich nahe der Oberflächen-Plasmonresonanz abweichen.

## I. INTRODUCTION

The dispersion relationship of surface polaritons of metals<sup>1,2</sup> and semiconductors<sup>3</sup> has been extensively studied for materials where the damping of the surface polariton oscillation is small. It is the aim of this study to investigate the optical properties of the surface plasmon of n+ silicon for which the oscillation is highly damped. The general dispersion relationship for surface plasmons for an air-material interface is<sup>4</sup>

$$k_{||} = \frac{\omega}{c} \left( \frac{\epsilon(\omega)}{\epsilon(\omega) + 1} \right)^{1/2} \quad (1)$$

where  $k_{||}$  is the surface plasmon wavevector which is parallel to the interface,  $\omega$  is the surface plasmon frequency,  $c$  is the speed of light, and  $\epsilon(\omega)$  is the frequency dependent bulk dielectric function of silicon which for this study will be of the form of the Drude free electron model which is

$$\begin{aligned} \epsilon(\omega) &= \epsilon_1(\omega) + i \epsilon_2(\omega) \\ &= \epsilon_\infty \left( 1 - \frac{\omega_p^2 \tau^2}{1 + \omega^2 \tau^2} \right) + i \epsilon_\infty \left[ \frac{\omega_p^2 \tau}{\omega(1 + \omega^2 \tau^2)} \right] \end{aligned} \quad (2)$$

where  $\epsilon_\infty$  is the high frequency dielectric function,  $\omega_p = (4\pi Ne^2/\epsilon_\infty m^*)^{1/2}$  is the bulk plasma frequency,  $m^*$  is the electron effective mass,  $N$  is the electron concentration,  $e$  is the electronic charge, and  $\tau$  is the electronic relaxation time.

For a damped surface oscillation the complex frequency - real wavevector solutions of the dispersion relationship given by Eq. (1) is solved by the methods of Gammon and Palik.<sup>5</sup> The wavevector  $k_{||}$  is assumed real, while the frequency of the excitation is complex and equal to

$$\omega = \omega_1 + i \omega_2 \quad (3)$$

where  $\omega_1$  is the surface plasmon frequency, and  $\omega_2$  is related to the surface plasmon damping. A plot of  $\omega_1$  versus  $k_{\parallel}$  yields the surface plasmon dispersion curve. Briefly, Gammon and Palik<sup>5</sup> methods involve substituting Eqs. (2) and (3) into Eq. (1) and solving for a  $\omega_2$  value for a particular  $\omega_1$  value such that the imaginary part of Eq. (1) is equal to zero. With these values of  $\omega_1$  and  $\omega_2$  the real part of Eq. (1) is solved for the real wavevector  $k_{\parallel}$ . Repeating this produces a set of  $\omega_1$ ,  $\omega_2$  and  $k_{\parallel}$  values are obtained from which the dispersion curve is obtained. The complex wavevector - real frequency solutions of the surface plasmon dispersion relationship [Eq. (1)] will not be discussed in this study.

The Otto ATR technique<sup>1</sup> is a method for coupling incident electromagnetic waves to surface polaritons. By computer curve fitting the ATR spectra to the Drude dielectric function [Eq. (2)] the optical properties of the surface active medium are obtained. Using these optical constants the dispersion relation of the surface plasmon on the real frequency axis is obtained from the computer calculated minima. Each minimum is obtained by fixing the incident angle and varying the frequency, where the reflected intensity of p-polarized light is greater than 90% at the minimum.

Section II contains the experimental details of sample preparation and surface plasmon resonance measurements. Section III gives the results of the optical measurements and discusses the dispersion of the surface plasmon on the real frequency axis. In Section IV we discuss the ATR analysis in the complex frequency plane and the complex frequency optical properties of n+ silicon. In Section V we summarize our results.

## II. EXPERIMENT

### A. Sample Preparation

The n+ silicon samples were obtained by diffusing phosphorous into a 5 N-cm n-type silicon wafer. The initial wafers were two inches in diameter and 18 mils thick and were polished on both sides. The samples were prepared at the Micro-Electronics Production Laboratory at Hughes Aircraft Company in Carlsbad. The wafers were initially prefurnace cleaned in a 50/50 mixture of  $H_2SO_4$  and  $H_2O_2$  to remove any oxide on the surface and to take off any wax left from the polishing. The samples were then diffused at 925°C in phosphine ( $PH_3$ ) gas for 20 minutes with a preheat and post-heat for ten minutes in  $N_2/O_2$ . After the n+ deposition, the samples were heated at 1000°C in pure nitrogen for 180 minutes. The purpose was to both electrically activate the phosphorous ions and to diffuse the phosphorous ions into the bulk of the sample and remove the high concentration of ions left on the surface. The samples were then deglazed in a 10 to 1 solution of  $H_2O$  and HF for five minutes for the purpose of removing any grown oxide on the silicon surface. The final resistance of the diffused layer was 0.1/square.

The initial wafers had a bow of 0.115 mils and a taper of 0.03 mils across the two inch diameter. The processed wafers were scribed and broken into ATR sample sizes of 450 x 300 mils. Aluminum spacers were electron beam evaporated onto two corners of the silicon and nine ~ 10 mil diameter aluminum spots were evaporated between the two corners. The silicon wafers were mounted with double backed tape onto optical flats (~1/2" thick). With the silicon die mounted on the optical flat as they were compressed against the base of the prism bowing of the wafer would take place when only the two corners of the die were coated with aluminum. Consequently, the addition of the ~ 10 mil diameter spots across the center region reduced the bowing.

significantly and allowed a reasonably uniform air gap to exist between the prism base and the silicon.

### B. Experimental Measurements and Data Analysis

Initial investigations of the optical properties of n+ silicon were done by measuring the near normal incidence reflectivity of silicon versus gold. These measurements were not absolute but were done for the purpose of finding the plasma edge and minimum. The minimum appeared to be at  $\sim 4.5 \text{ \AA}$  and consequently ATR spectrum runs were performed in the range of 3  $\text{\AA}$  to 9  $\text{\AA}$ . ATR measurements were performed by measuring the ratio of the reflected intensity of p-polarized light ( $R_p$ ) with the sample pressed against the ATR prism to that with the sample removed. The Otto ATR method of exciting surface plasmon modes was used where the surface plasmon was for an air-Si interface.

A  $\text{CaF}_2$  prism ( $57.1^\circ - 65.6^\circ$  [apex] -  $57.3^\circ$ ) was used for all measurements; it has an average index of 1.45 and it transmits out to 3 microns. The prism base was flat to greater than a tenth of a wave ( $0.5461 \text{ \AA}$ ) and the uniformity of the air gap was determined by viewing Newton interference fringes for angles less than the critical angle and by viewing the surface plasmon resonance of aluminum which appears in the visible spectrum for angles greater than the critical angle, uniformity of this color absorption was adjusted. Good uniformity of the air gap across the whole silicon surface was impossible to obtain due to its natural bow; consequently, the input beam was masked to hit only the approximately uniform section. Due to this bowing problem, uniform air gaps could be obtained only for small spacings between the silicon sample and the prism base. The probable reason for this reduction of bowing at small spacings is that both high points on the silicon and dust particles are present between the prism base and silicon surface which acts as a natural spacer.

The globar light source was focused down (beam divergence = 5°) and optical alignment of the beam could be seen by viewing the output beam of the prism assembly with a mirror. The reflection spectra were taken on a Perkin Elmer model 301 far infrared spectrometer operated in a single beam mode with the addition of appropriate gratings and filters. The 13 cps chopped signal from the thermocouple detector was digitized and then computer averaged. The wire grid polarizer was placed in the p-polarizing position and placed before the input beam to the prism.

C. Optical Constants and ATR Curve Fitting

The ATR reflection spectra were taken at room temperature and displayed in Figs. 1 and 2. The spectra are plotted as normalized reflectivity ratio  $R_p$  versus wavelength where the data points are corrected for the effects of the aluminum spacers. The optical properties of the n+ silicon were determined by doing a least squares curve fit of the Drude parameters  $N/m^2$  and  $\tau$ , and the air gap  $d$ . The high frequency dielectric constant  $\epsilon_\infty$  used in the Drude model Eq. (2) was taken to be equal to  $\epsilon_0 = 11.7$  the dielectric constant of silicon at zero frequency in the absence of free carriers. Since silicon is homopolar, the dielectric constant of silicon is equal to  $\epsilon_0$  in the absence of free carriers from zero frequency up to the first interband transition. The dielectric constant  $\epsilon_0 = 11.7$  was determined by Salzberg and Willa<sup>6</sup> on measuring the refractive index of a prism made of single crystal silicon. This dielectric constant also agrees with the value measured at radio frequencies on intrinsic silicon by Dunlap and Walters.<sup>7</sup>

The parameters  $N/m^2$  and  $\tau$  were varied along with the air gap  $d$  to obtain the best fit least squares parameter  $\chi^2$  defined as

$$\chi^2 = \frac{\sum (R_p^{\text{theory}} - R_p^{\text{exp}})^2}{N}$$

where the sum over  $i$  is for all data points and  $M$  is the total number of data points. The curve fitting program<sup>3</sup> was based on choosing an air gap  $d$  and finding the parameters  $N/m^*$  and  $\tau$  which had a best fit of the measured reflection. The air gap  $d$  is used almost like an independent parameter, that is, for a particular  $d$  the best fit parameters are determined, then  $d$  is varied and a set of new best fit parameters is determined and the total set with the smallest  $f$  is chosen as the best fit. The total percentage area of aluminum covering the silicon was  $7.6 \pm 2.7\%$ . The input beam was masked to hit only the uniform air gap area, and it was impossible to measure exactly the total area of aluminum that was blocking the beam from hitting the silicon. Therefore, the ATR computer calculations were calculated for different percentages of aluminum present within the 2.7% change as given above; and the best fit was determined by the lowest least squares deviation. The best fit Drude reflectivities are plotted on the same graphs as the reflectivity data.

### III. RESULTS AND DISCUSSION

#### A. Optical Properties

The Drude free electron model of the dielectric function fits satisfactorily to the ATR spectra curves as shown in Figs. 1 and 2. The experimental error is relatively large due to the bowing of the silicon chip and the need to add the extra aluminum spacer pads. The deviation in the region of the minimum for the curve fit in Fig. 2 is possibly indicative of the need to include a frequency dependent collision time. A similar deviation was obtained by Kukharskii and Suboshiev<sup>9</sup> when they curve fitted a Drude model to n+ silicon. They corrected this deviation by using a frequency dependent relaxation time. There exists other problems in this part of the spectral region where the Drude model should be corrected. Namely, as shown by Salzberg and Villa,<sup>6</sup>  $\epsilon_{\infty}$  increases from  $\sim 11.7$  at  $6 \text{ \AA}$  to  $\sim 11.82$  at  $2.5 \text{ \AA}$ . This is due to the dispersion of the index of refraction when the band edge is approached. Spitzer and Fan<sup>10</sup> have shown that this is a small absorption band in the range of  $1.5 \text{ \AA}$  to  $5 \text{ \AA}$  which is dependent on carrier concentration. Corrections for these effects were not included due to the relatively large experimental error and in the region  $\lambda > 5 \text{ \AA}$  the region where the surface plasmon exists, the curve fits were good enough and should accurately reproduce the surface plasmon response.

The experimentally determined Drude free carrier parameters are shown in Table I along with the optical mobility  $\mu = e\tau/m^*$  and the electron carrier concentration N. The overall accuracy of this least squares fitting procedure can be seen by viewing Fig. 3 where each parameter is varied by 10% higher values, from the best fit which is also plotted with it. A value of  $N = 7 \times 10^{12} \text{ e/cm}^3$  was determined from a measurement of electrical resistivity

( $1.32 \times 10^{-3}$   $\Omega\text{-cm}$ ) and using the resistivity versus impurity concentration listed in Sze<sup>11</sup>; this agreement is reasonable and the difference is probably due to different sample mobilities. Kukharskii and Suboshiev<sup>9</sup> obtained a relaxation time of  $11.27 \times 10^{-15}$  sec for an n-type silicon of carrier concentration  $5.5 \times 10^{19}$   $\text{e/cm}^3$ . They also obtained a value of  $\omega_p t = 2.69$  which is in agreement with the present results.

### B. Dispersion Analysis

The value of  $\omega_p t = 2.69$  as determined from the Drude optical parameters (Table I) shows that the surface plasmon resonance of n+ silicon is fairly highly damped. The complex frequency - real wavevector solutions of the theoretical dispersion curve Eq. (1) is shown in Figs. 4 and 5. The complex frequency solutions exhibit the standard behavior of the surface plasmon resonance; namely,  $\omega_1 \rightarrow \omega_s$  and  $\omega_2 \rightarrow -1/2\pi$  as the wavevector  $k \rightarrow \infty$ .

The ATR surface plasmon dispersion curve is found by plotting the energy and wavevector at the minimum reflectivity point in the ATR spectrum. The ATR minimum point is taken when the reflectivity of p-polarized light is at 90%. The general computer procedure has been previously explained,<sup>12</sup> and the results of the analysis are shown in Table II. In this table, you can see that as the angle AO (angle with respect to the prism base) is increased, the wavelength at the minimum ( $\lambda$ ), increases to longer wavelengths and smaller experimental wavevectors ( $k$ )<sup>EXPT</sup> are achieved. This analysis shows that as the incident angle is decreased, the ATR dispersion curve approaches the light line, as can be seen by studying the last column which gives the ratio of the wavevector generated by the prism  $k$ <sup>EXPT</sup> to the wavevector of light in air ( $k_0 = 2\pi/\lambda$ ). That is, the experimental ratio  $k/k_0$  approaches 1 as  $\theta$  goes higher in energy. This is equivalent to the complex  $k$  behavior of the surface plasmon resonance where the dispersion relationship starts to set the

light line and then back-bends going into Brewster modes where  $k_z < \omega/c$ .<sup>13</sup> Therefore, the ATR determined dispersion shows no resonance as is achieved by the theoretical dispersion relationship. Since  $\omega_p^T = 1.69$ , there is no physical explanation why there is no resonance present in the ATR dispersion curve obtained using real frequencies. Consequently the only true coupling to the surface plasmon resonance of n+ silicon will occur by probing the complex k response which is experimentally achieved by fixing the excitation frequency and by varying the angle of incidence. The complex  $\omega$  response measurements will only allow moderate coupling which is achieved by riding on the ridges and valleys of the surface plasmon excitation in the real frequency plane.

#### IV. ATR ANALYSIS IN THE COMPLEX FREQUENCY PLANE AND COMPLEX FREQUENCY OPTICAL PROPERTIES OF N+ SILICON

Due to the discrepancy between the theoretical damped surface plasmon dispersion relationship which shows a definite resonance, and the ATR minima dispersion curve which shows back-bending which is calculated using real frequency dependent optical constants, an approach was made to calculate the ATR reflection spectrum in the complex frequency plane. In order to calculate the ATR spectrum in the complex frequency plane, the optical constants of the surface active medium and the Fresnel reflectance coefficient must be redefined to be functions of complex frequency. Since the frequency is complex, then the real [ $\epsilon_1(\omega)$ ] and imaginary [ $\epsilon_2(\omega)$ ] parts of the dielectric functions are themselves complex as given by

$$\epsilon(\omega) = \epsilon_1(\omega) + i \epsilon_2(\omega) \quad (4a)$$

where

$$\epsilon_1(\omega) = \text{Re } \epsilon_1(\omega) + i \text{Im } \epsilon_1(\omega) \quad (4b)$$

$$\epsilon_2(\omega) = \text{Re } \epsilon_2(\omega) + i \text{Im } \epsilon_2(\omega) \quad (4c)$$

where  $\omega$  is the complex frequency defined by  $\omega = \omega_1 + i\omega_2$ . If one substitutes Eqs. (4b) and (4c) into Eq. (4a) and regroup into real and imaginary parts, one obtains

$$\epsilon(\omega) = [\text{Re } \epsilon_1(\omega) - \text{Im } \epsilon_2(\omega)] + i [\text{Re } \epsilon_2(\omega) + \text{Im } \epsilon_1(\omega)] \quad (4d)$$

Now using the standard definition of  $\epsilon_1(\omega)$  and  $\epsilon_2(\omega)$  to be equal to the real and imaginary parts of the dielectric function respectively as given in Eq. (3) we obtain

$$\epsilon_1(\omega) = \epsilon_1(\omega_1, \omega_2) = \text{Re } \epsilon_1(\omega) - \text{Im } \epsilon_2(\omega) \quad (4a)$$

$$\epsilon_2(\omega) = \epsilon_2(\omega_1, \omega_2) = \text{Re } \epsilon_2(\omega) + \text{Im } \epsilon_1(\omega) \quad (4b)$$

By redefining the dielectric function in this way, we show that the effect of the complex frequency is to mix the old relationship of  $\epsilon_1$  and  $\epsilon_2$ . That is, now the real part of the dielectric function is affected by  $\epsilon_2$  through its imaginary part. Also by the definition of the complex frequency that as  $\omega_2 \rightarrow 0$ , the imaginary parts of  $\epsilon_1(\omega)$  and  $\epsilon_2(\omega)$  both go to zero and we have the original relationship in the real frequency plane. With the dielectric function as defined in Eqs. (6a) and (6b), we can use the standard relationships between the optical constants  $n$  and  $k$  and the dielectric function  $\epsilon_1(\omega)$  and  $\epsilon_2(\omega)$  in the complex frequency plane which is

$$n = n(\omega_1, \omega_2) = \left\{ \frac{1}{2} [(\epsilon_1^2 + \epsilon_2^2)^{1/2} - \epsilon_1] \right\}^{1/2} \quad (7a)$$

$$k = k(\omega_1, \omega_2) = \left\{ \frac{1}{2} [(\epsilon_1^2 + \epsilon_2^2)^{1/2} + \epsilon_1] \right\}^{1/2} \quad (7b)$$

$$N = n + ik \quad . \quad (7c)$$

Consequently the complex index of refraction of the medium ( $N$ ) is a function of complex frequency and may be used directly in determining the AIR reflectivity in the complex frequency plane. This is done by redefining the Fresnel reflection coefficient for p-polarized light as:

$$\frac{N_2 \cos\theta_3 - N_3 \cos\theta_2}{N_2 \cos\theta_3 + N_3 \cos\theta_2} = \frac{N_2(\omega_1, \omega_2) \cos\theta_3 - N_3(\omega_1, \omega_2) \cos\theta_2}{N_2(\omega_1, \omega_2) \cos\theta_3 + N_3(\omega_1, \omega_2) \cos\theta_2} \quad (7d)$$

where  $N_3$  is the complex index of refraction of the surface active medium, which in this case is silicon, and  $N_2$  is the complex index of refraction of the material between the prism and the surface active medium, which is air in this case study, and  $\theta_2$  and  $\theta_3$  are the incident angles for medium 2 and 3 respectively.

The complex frequency dependence of the real and imaginary parts of the index of refraction  $N$  can also be obtained using a different procedure. This method is more difficult to solve and involves substituting Eqs. (6a) and (6b) into Eqs. (7a) and (7b) and finally redefining the complex index of refraction is

AD-A100 979

CALIFORNIA UNIV LOS ANGELES DEPT OF PHYSICS  
CHARACTERIZATION OF INFRARED OPTICAL PROPERTIES OF TRANSPARENT --ETC(U)  
MAY 81 R BRAUNSTEIN

F/G 20/6

AFOSR-78-3665

NL

UNCLASSIFIED

AFOSR-TR-81-0545

2 OF 2  
AD A  
-000979

END  
DATE  
FILED  
7-81  
DTIC

$$N = n + ik \quad (9a)$$

where

$$n = n(\omega_1, \omega_2) = \operatorname{Re} n - \operatorname{Im} k \quad (9b)$$

$$k = k(\omega_1, \omega_2) = \operatorname{Re} k + \operatorname{Im} n \quad . \quad (9c)$$

Implementing this procedure, the optical constants of n+ silicon were expressed as functions of complex frequency and used to calculate the ATR dispersion curve. The calculations were done by using a high speed computer program.<sup>8</sup> The general procedure was to first obtain a set of  $\omega_1$  and  $\omega_2$  values as determined from calculating the complex frequency - real wavevector dispersion curve [Eq. (1)]; that is, by solving the imaginary part of the dispersion relationship a value for  $\omega_2$  was obtained for each  $\omega_1$  value. This set of  $\omega_1$  and  $\omega_2$  values was used to calculate the real and imaginary parts of  $\epsilon_1$  and  $\epsilon_2$  from Eqs. (2) and (4); and then using these values in Eqs. (6a) and (6b) to obtain  $\epsilon_1(\omega_1, \omega_2)$  and  $\epsilon_2(\omega_1, \omega_2)$ ; which then are used in Eqs. (7a) and (7b) to obtain the complex frequency dependent optical constants. These complex frequency optical constants and Fresnel reflection coefficients were used to calculate the ATR dispersion curve in the same way as done in the real frequency spectrum; but now the ATR minimum is found by fixing the angle of incidence and by scanning through  $\omega_1$  the real part of the surface plasmon frequency.<sup>4</sup> The ATR dispersion curve minima are plotted in Fig. 6 along with the damped surface plasmon dispersion curve. There is no discrepancy between the ATR dispersion curve calculated in complex frequency plane and the theoretical dispersion curve. The complex frequency ATR analysis shows a definite resonance. The error bars indicate the range of uncertainty that the ATR minima were obtained. The deviation at lower values of wavevector is due to the way that the ATR dispersion curve was generated, that is, with fixing the angle of incidence and varying the frequency of the input light. This type of ATR analysis tends to ride along valleys or ridges of the dispersion at lower

wavevectors.

Using the complex frequency dependent dielectric function<sup>1</sup> the surface plasmon obeys the following resonance condition:

$$\epsilon(\omega_1, \omega_2) = -1$$

where

$$\epsilon_1(\omega_1, \omega_2) = \text{Re } \epsilon_1 - \text{Im } \epsilon_2 = -1$$

$$\epsilon_2(\omega_1, \omega_2) = \text{Re } \epsilon_2 + \text{Im } \epsilon_1 = 0 \quad . \quad (10)$$

The real and imaginary parts of the complex frequency dependent Drude dielectric function is shown in Figs. 7 and 8. As can be readily seen, the deviation of the real and imaginary parts of the dielectric function becomes large near the surface plasmon resonance point. In Table III there is a comparison of the values of the real part of  $\epsilon_1(\omega)$  which is a function of complex frequency and  $\epsilon_1(\omega)$  calculated from Drude model for real frequencies. As can be seen from Table III, the difference in the region close to the surface plasmon resonance ( $\lambda = 6.66 \mu$ ) is quite large. The wavevector solutions of the surface plasmon dispersion relationship [Eq. (1)] in the region between  $\epsilon(\omega) = -1$  and  $\epsilon(\omega) = 0$  are imaginary and are not surface modes in the fact that they are uncoupled modes between the incident light and the surface active medium. The complex frequency dielectric functions shown in Figs. 7 and 8 have extrapolated lines covering this region. Also in the region close to  $\epsilon(\omega) = -1$  the complex  $\omega$  solutions are very difficult to obtain due to the nature of the resonance, that is, the solutions occur in a very narrow valley with a step fall-off on both sides of the valley and can be easily missed by the computer procedure.<sup>8</sup> The surface plasmon resonance point was determined and is marked by an X on the dielectric function plots.

In Table IV a comparison is made of the dielectric functions obtained for real and complex frequency. The dielectric functions approach one another

at high frequencies and deviate the largest in the area of the surface plasmon resonance. Solutions are shown in the regions where  $\epsilon(\omega) > 0$  and  $\epsilon(\omega) < -1$ ; where for  $\epsilon(\omega) > 0$  the dispersion analysis yields solutions for Brewster<sup>13</sup> modes, and for  $\epsilon(\omega) < -1$  solutions are surface polariton modes (Fano modes).<sup>13</sup> The surface plasmon resonance occurs when  $\omega_1 = \omega_s$  and  $\omega_2 = -1/2\tau$  where  $\tau$  is the electron relaxation time. Solutions for the Brewster modes<sup>13</sup> show that the bulk plasmon frequency is also complex and occurs at  $\omega_1 = \omega_p$  and  $\omega_2 = -1/2\tau$ .

## V. CONCLUSIONS

It can be concluded from analyzing the surface plasmon of n+ silicon that the dispersion relationship obtained from plotting the ATR minima obtained in the real frequency plane does not exhibit the surface plasma resonance; whereas the theoretical dispersion relationship yields the resonance.

Consequently, for this n+ silicon material which has a relatively high damping the surface plasmon will not exhibit a resonance in the real frequency spectrum when coupling is performed using the ATR experimental technique of fixing incident angle and varying frequency. By using the complex frequency analysis either through the theoretical dispersion relationship or using our developed complex frequency dependent optical constants and analyzing the ATR minima in the complex frequency plane the location of the complex frequency resonance can be obtained.

A comparison of the real and imaginary parts of the Drude dielectric function for n+ silicon for both real and complex frequencies shows that they numerically deviate the largest in the area of the surface plasmon and approach one another in value at high frequencies.

References

- \* Based in part upon a dissertation submitted by P. F. Robusto to the University of California at Los Angeles, in partial fulfillment of the requirements for the degree of Ph.D. in Physics.
- + Work performed with a Howard Hughes Doctoral Fellowship. Present address: Hughes Aircraft Co., 6155 El Camino Real, Carlsbad, CA 92008.
- ‡ Work supported in part by U. S. Army Research Office, Durham, North Carolina, and by the Air Force Office of Scientific Research.
- 1. A. Otto, *Z. Physik* 219, 227 (1969).
- 2. A. Otto, *Z. Physik* 216, 398 (1968).
- 3. N. Marschall and B. Fischer, *Phys. Rev. Lett.* 28, 13, 811 (1972).
- 4. R. A. Ferrell, *Phys. Rev.* 111, 1214 (1958).
- 5. R. W. Gammon and E. D. Palik, *J. Opt. Soc. Am.* 64, 3, 350 (1974).
- 6. C. O. Salzberg and J. J. Villa, *J. Opt. Soc. Am.* 48, 579 (1957).
- 7. W. C. Dunlap and R. L. Walters, *Phys. Rev.* 92, 116 (1953).
- 8. P. F. Robusto, Ph.D. Thesis (UCLA, 1978).
- 9. A. A. Kukharskii and V. K. Suboshiev, *Sov. Phys.-SemiCond.* 4, 234 (1970).
- 10. W. G. Spitzer and H. Y. Fan, *Phys. Rev.* 108, 2, 268 (1957).
- 11. S. M. Sze, Physics of Semiconductor Devices (John Wiley & Sons, N.Y., 1969).
- 12. P. F. Robusto and R. Braunstein, "Optical Measurements of the Surface Plasmon of Copper," to be published in *Physica Status Solidi*.
- 13. E. Burstein and F. DeMartini, Proceedings of the First Taormina Research Conference on the Structure of Matter (Pergamon Press, N.Y., 1972).

Figure Captions

Fig. 1. Normalized ATR reflection spectrum of n+ silicon plotted as normalized p-polarized reflectivity versus wavelength. Solid points are the data points corrected for effects of the aluminum spacers. Solid curve is the best fit least squares curve with the best fit parameters shown in the blocked region. Shown in the insert is the ATR geometry used with the angle of incidence of the input beam is 5 degrees.

Fig. 2. Normalized ATR reflection spectrum of n+ silicon plotted as normalized p-polarized reflectivity versus wavelength. Solid points are the data points corrected for effects of the aluminum spacers. Solid curve is the best fit least squares curve with the best fit parameters shown in the blocked region. Shown in the insert is the ATR geometry used with the angle of incidence of the input beam is 0 degrees.

Fig. 3. ATR reflectivity spectrum of n+ silicon where each of the best fit parameters  $\tau$ ,  $N/m^*$ , and  $d$  are changed to 15% higher values.

Fig. 4. Theoretical dispersion curve [Eq. (1)] of the surface plasmon of n+ silicon plotted as the real part of the complex energy  $\Re\omega_1$  versus real wavevector  $k_{\parallel 1}$ . Also shown is the light line ( $k = \omega/c$ ) along with the energy wavevector light line (dashed line) generated by the ATR configuration shown in Fig. 2. The theoretical dispersion curve is plotted from the parameters given in Table I.

Fig. 5. Imaginary part of the complex energy ( $\Im\omega_1$ ) versus real wavevector for the surface plasmon of n+ silicon.

Fig. 6. Same diagram as in Fig. 4 with the inclusion of the ATR minima points calculated using the complex frequency dependent dielectric functions as defined in Eq. (4). Error bars show the range within which the minima were determined.

Fig. 7. Real and imaginary parts of complex frequency dependent  $\epsilon_1$  versus wavelength for n+ silicon; where  $\epsilon_1(\omega_1, \omega_2) = \text{Re } \epsilon_1 + i \text{ Im } \epsilon_1$  and is not redefined as in Eq. (4) and where  $L_1 = 2\pi c/\omega_1$ .

Fig. 8. Real and imaginary parts of complex frequency dependent  $\epsilon_2$  versus wavelengths for n+ silicon; where  $\epsilon_2(\omega_1, \omega_2) = \text{Re } \epsilon_2 + i \text{ Im } \epsilon_2$  and is not redefined as in Eq. (4) and where  $L_1 = 2\pi c/\omega_1$ .

TABLE I. Experimentally Determined Drude Free Carrier Parameters for n+  
Silicon

$\epsilon_{\infty}^{(1)}$	$N/m^*$ ( $\times 10^{20}$ e/cm <sup>3</sup> )	$\tau$ ( $\times 10^{-15}$ sec)	$m^*^{(2)}$	$N$ ( $\times 10^{19}$ e/cm <sup>3</sup> )	$\mu_{opt.}$ (cm <sup>2</sup> /V-sec)
11.7	3.58	8.62	0.26	9.31	58.3

(1) Input parameter for calculation

(2) Fraction of electron rest mass obtained from Spitzer and Fan.<sup>10</sup>

TABLE II. Analysis of ATR Calculated Dispersion Curve for n+ Silicon<sup>(1)</sup>

$A_0$ <sup>(2)</sup> (degrees)	$L_o$ <sup>(3)</sup> (microns)	$D_o$ <sup>(3)</sup> (microns)	$k_{  }^{\text{exp}}$ <sup>(4)</sup> ( $\times 10^{-4}$ cm $^{-1}$ )	$k_{  }^{\text{exp}}/k_o$ <sup>(5)</sup>
23.8	468.9	400.9	$1.35 \times 10^{-2}$	1.00886
47.4	1074.4	11.4	$1.08 \times 10^{-2}$	1.839
49.2	1164.6	10.97	$1.02 \times 10^{-2}$	1.894
53.1	1376.7	10.34	$9.126 \times 10^{-3}$	1.9997
57.1	1685.4	10.11	$7.825 \times 10^{-3}$	2.099
61.08	2117.5	10.24	$6.493 \times 10^{-3}$	2.188
66.88	3195.7	11.182	$4.519 \times 10^{-3}$	2.279

(1) Input Drude parameters:  $\epsilon_{\infty} = 11.7$ ,  $\tau = 5.62 \times 10^{-15}$  sec,  $N/m^* = 3.58 \times 10^{20}$ .

(2) Angle of incidence with respect to the prism base where  $n_p = 2.5$ .

(3)  $L_o$  and  $D_o$  are the wavelength at the minimum and the air gap respectively to obtain a p-polarized reflectivity of 90%.

(4) This is the experimental wavevector at the minimum where  $k_{||}^{\text{exp}} = \frac{2\pi}{L_o} n_p \sin(A_0)$ .

(5) This is the ratio of the experimental wavevector to the wavevector of light ( $k_o = \omega/c = 2\pi/L_o$ ).

TABLE III. Comparison of the Real Part of the Complex  $\omega$  Dielectric Functions $\epsilon_1(\omega)$  and  $\epsilon_2(\omega)$  versus the Dielectric Function for Real Frequency  $\omega'$ 

$L(\mu)$ <sup>(1)</sup>	$\text{Re } \epsilon_1$ <sup>(2)</sup>	$\epsilon_1(\omega')$ <sup>(3)</sup>	$\Delta \epsilon_1$ <sup>(3)</sup>	$\text{Re } \epsilon_2$ <sup>(4)</sup>	$\epsilon_2(\omega')$	$\Delta \epsilon_2$ <sup>(5)</sup>
2	10.4351	10.4351	0	0.155894	0.155894	0
3	8.90629	8.90623	0.00006	0.516462	0.516484	0.00002
4	6.85904	6.85776	0.001	1.19291	1.19358	0.0007
5	4.39286	4.37016	0.023	2.2433	2.25844	0.015
5.5	3.09752	2.98949	0.108	2.87194	2.95223	0.080
5.9	2.31265	1.82975	0.419	3.20381	3.5886	0.385
6.66	0.229251	-0.486703	0.716	4.34137	5.00156	0.660
6.7	0.0409945	-0.612146	0.653	4.4751	5.08339	0.608
6.8	-0.43728	-0.927106	0.4898	4.8232	5.29124	0.468
7	-1.28267	-1.56256	0.2799	5.44094	5.72098	0.280
7.5	-3.06521	-3.1795	0.114	6.75068	6.87692	0.126
8.5	-6.46159	-6.50066	0.039	9.48172	9.53347	0.052
9	-8.15995	-8.18639	0.026	10.990	11.0292	0.039
10	-11.5531	-11.5672	0.014	14.3139	14.338	0.024
11	-16.5556	-16.5623	0.007	20.0136	20.0286	0.015

(1) Wavelength of the incident light in microns and for the complex frequencies is  $L = 2\pi c/\omega_1$ .

(2) Real part of the complex dielectric function  $\epsilon_1(\omega) = \epsilon_1(\omega_1 + i\omega_2) = \epsilon_1(\omega_1, \omega_2) = \text{Re } \epsilon_1 + i \text{Im } \epsilon_1$ .

(3)  $\Delta \epsilon_1 = |\text{Re } \epsilon_1(\omega_1, \omega_2) - \epsilon_1(\omega')|$  where  $\omega_1$  and  $\omega_2$  are the real and imaginary parts of the complex frequency  $\omega$ , and  $\omega'$  is the real frequency.

(4) Imaginary part of the complex dielectric function  $\epsilon_2(\omega) = \epsilon_2(\omega_1 + i\omega_2) = \epsilon_2(\omega_1, \omega_2) = \text{Re } \epsilon_2 + i \text{Im } \epsilon_2$ .

(5)  $\Delta \epsilon_2 = |\text{Re } \epsilon_2(\omega_1, \omega_2) - \epsilon_2(\omega')|$ .

TABLE IV. Comparison of the Drude Dielectric Function as a Function of Real and Complex Frequencies

$L(\mu)$ <sup>(1)</sup>	$\epsilon_1(\omega')$ <sup>(2)</sup>	$\epsilon_1(\omega)$ <sup>(3)</sup>	$\epsilon_2(\omega')$ <sup>(4)</sup>	$\epsilon_2(\omega)$ <sup>(5)</sup>
2	10.4351	10.4343	0.155894	0.154283
3	8.9062	8.90199	0.516484	0.501147
4	6.85776	6.82434	1.19358	1.10091
5	4.37016	4.16524	2.25844	1.76509
5.5	2.98949	2.50169	2.95223	1.73513
5.9	1.82975	0.91369	3.5686	0.67388
6.66	-0.486703	-1.91911	5.00156	0.90968
6.7	-0.612146	-2.04816	5.08339	1.17191
6.8	-0.927106	-2.32911	5.29124	1.90725
7	-1.56256	-2.82691	5.72098	3.16219
7.5	-3.1795	-4.216	6.87692	5.19277
8.5	-6.50066	-7.33573	9.53347	8.46068
9	-8.18639	-8.96977	11.0292	10.1071
10	-11.5672	-12.2899	14.338	13.606
11	-16.5623	-15.6069	20.0286	17.4264

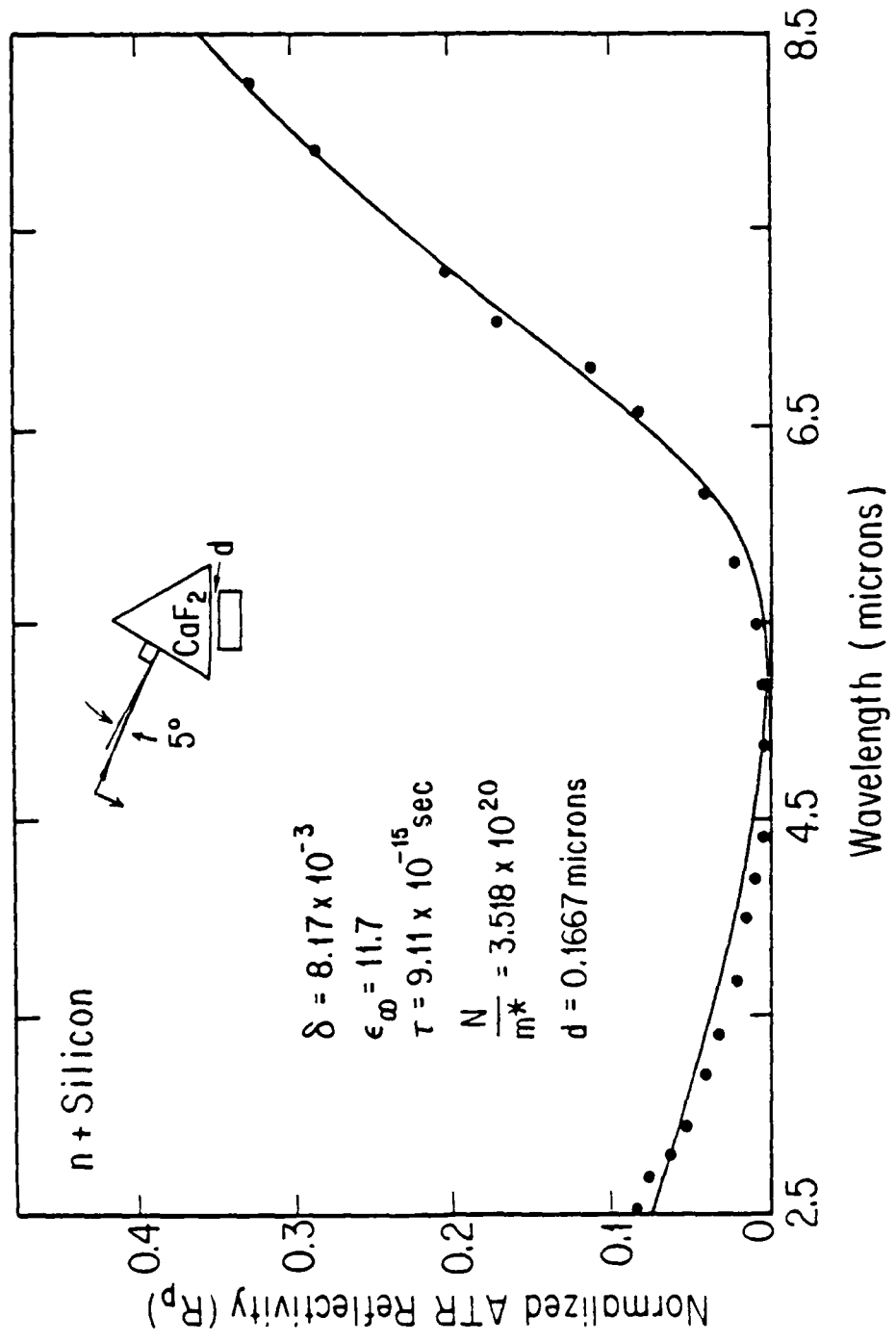
(1) Wavelength in microns for the real frequency  $\omega'$  and for complex frequency  $L = 2\pi c/\omega_1$ .

(2) Real part of dielectric function as a function of real frequency  $\omega'$ .

(3) Real part of dielectric function as a function of complex frequency  $\omega = \omega_1 + i\omega_2$  as defined in Eq. (4), that is,  $\epsilon_1(\omega) = \epsilon_1(\omega_1, \omega_2)$ .

(4) Imaginary part of dielectric function as a function of real frequency  $\omega'$ .

(5) Imaginary part of dielectric function as a function of complex frequency  $\omega = \omega_1 + i\omega_2$  as defined in Eq. (4), that is,  $\epsilon_2(\omega) = \epsilon_2(\omega_1, \omega_2)$ .



卷之二

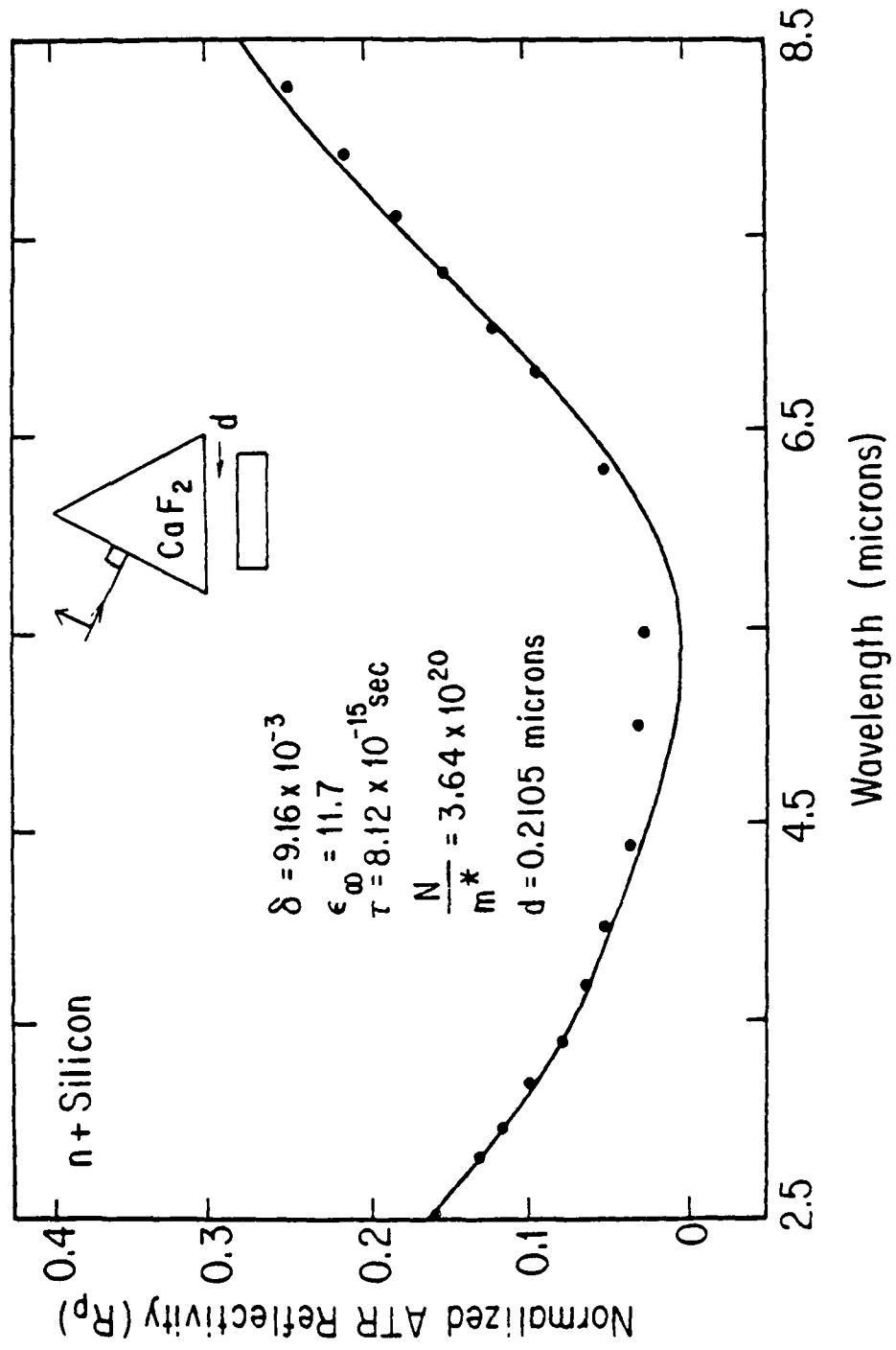


Fig. 2

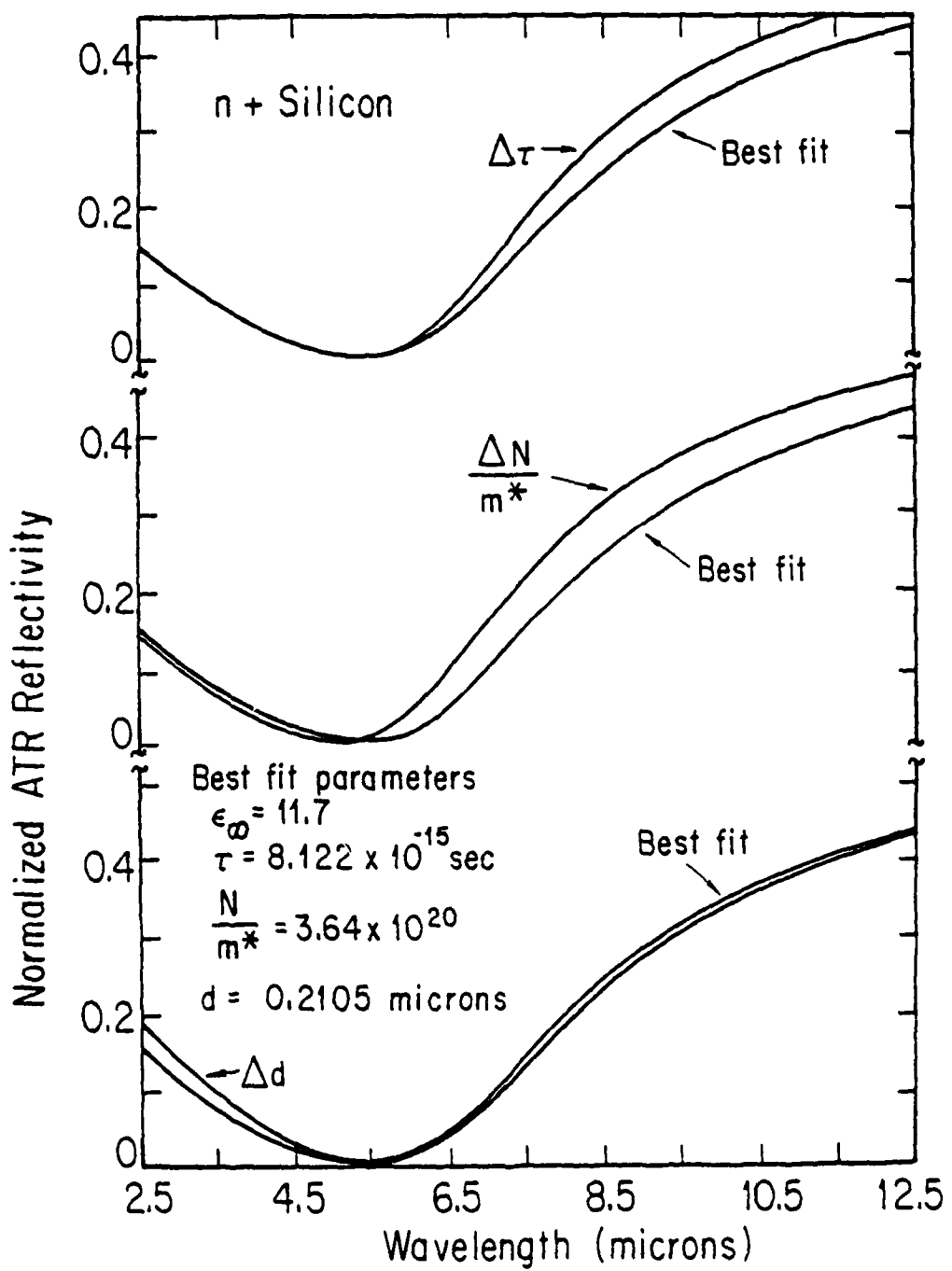


Fig. 3

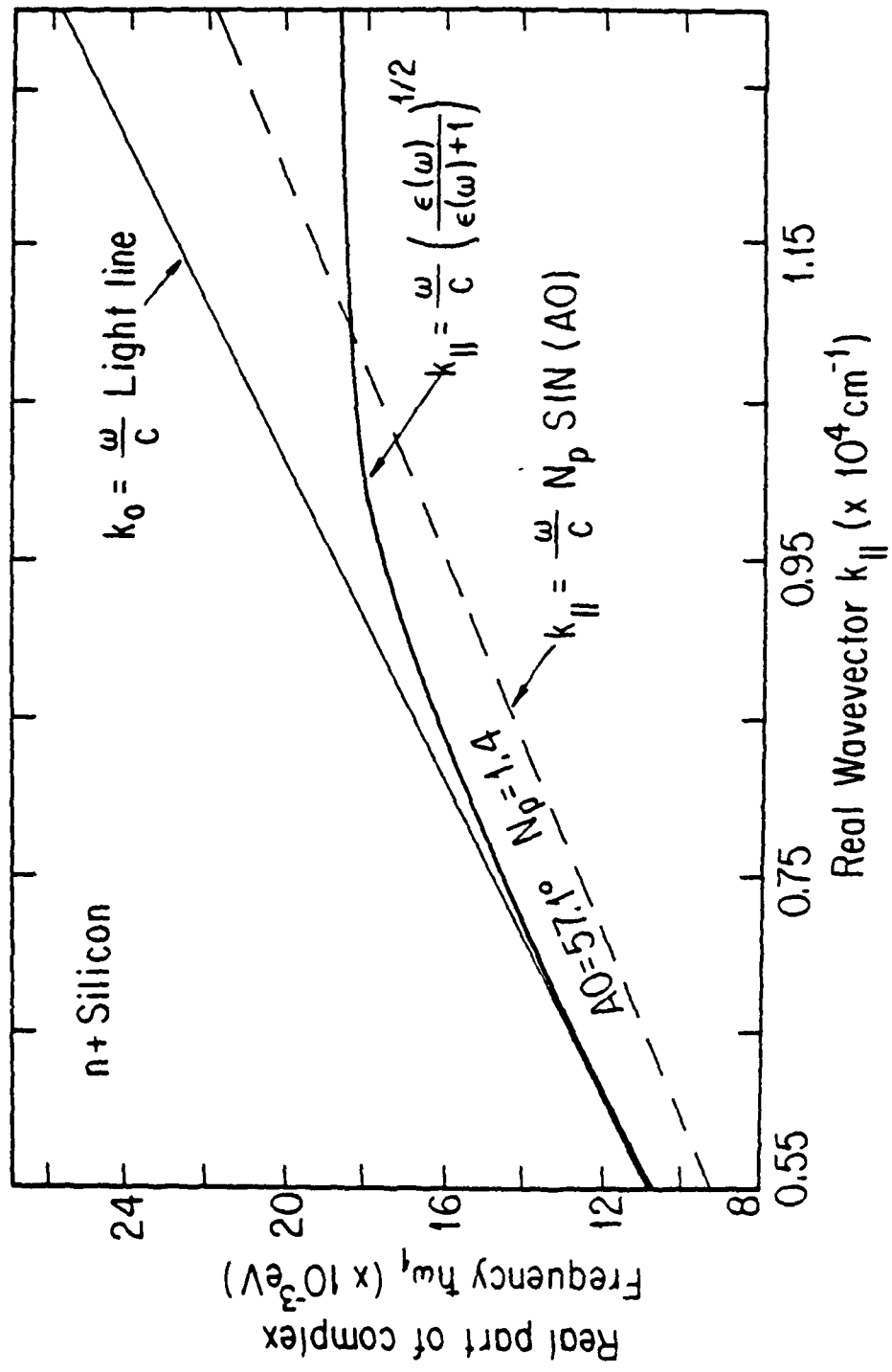


Fig. 4

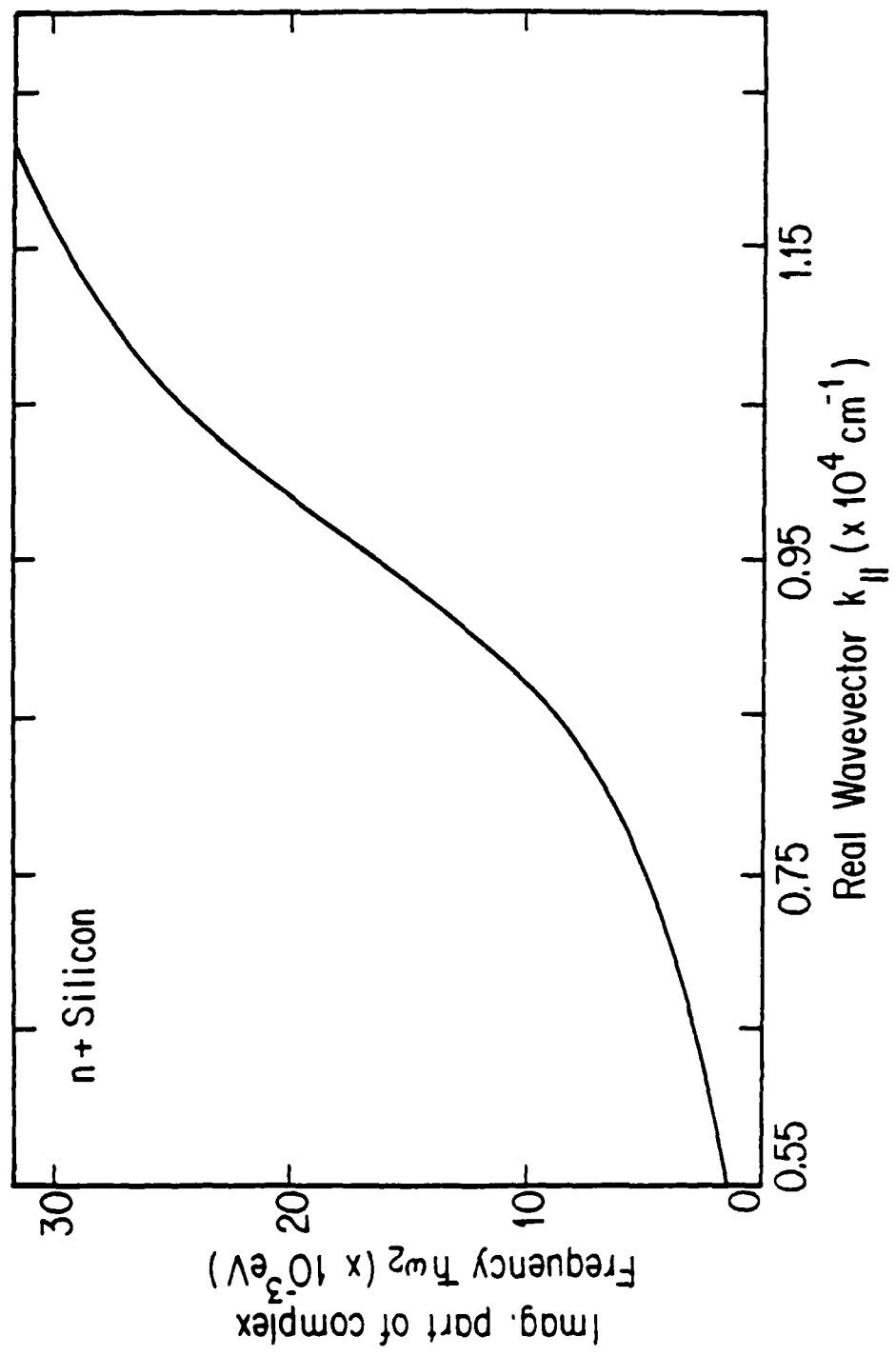


Fig. 5

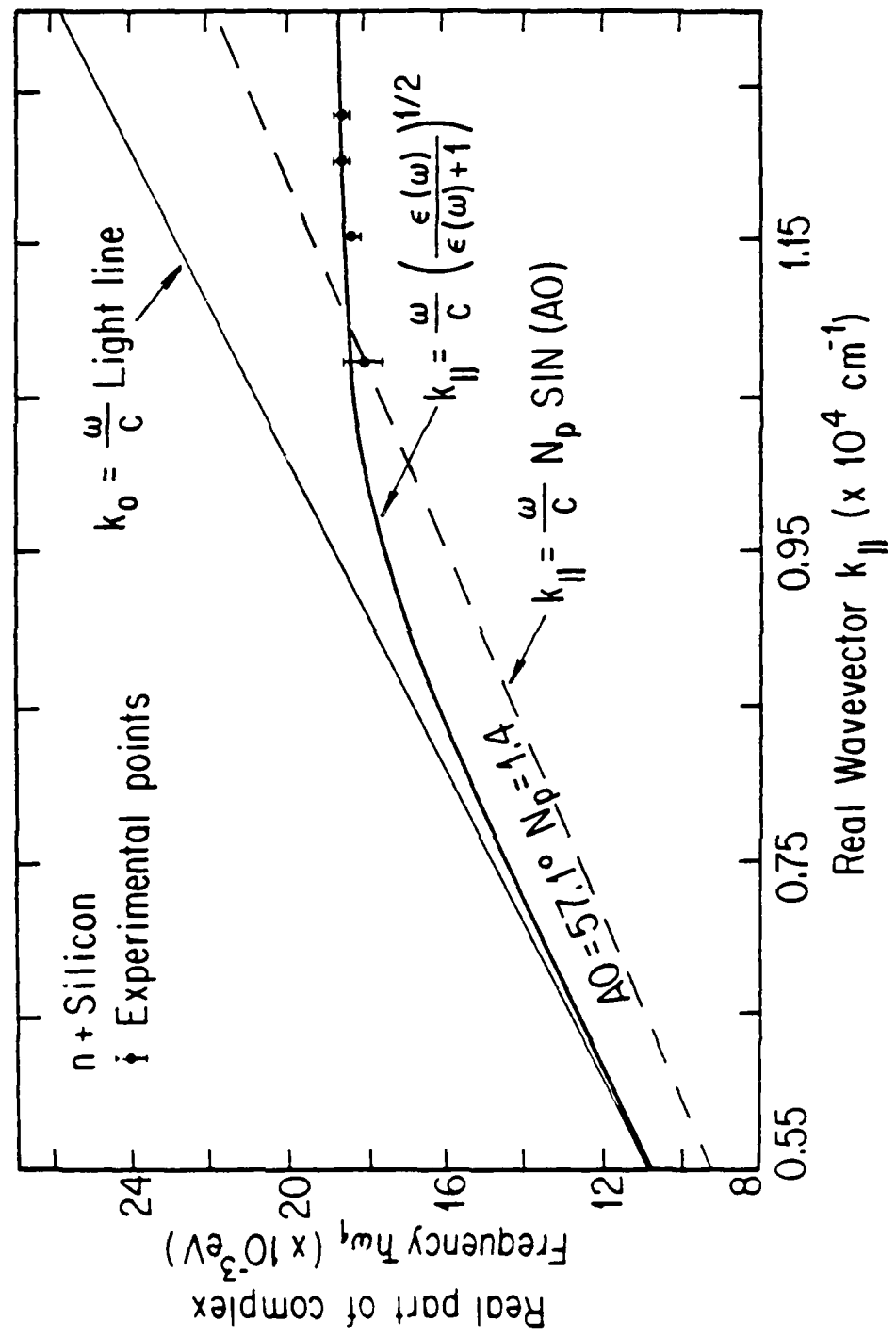


Fig. 6

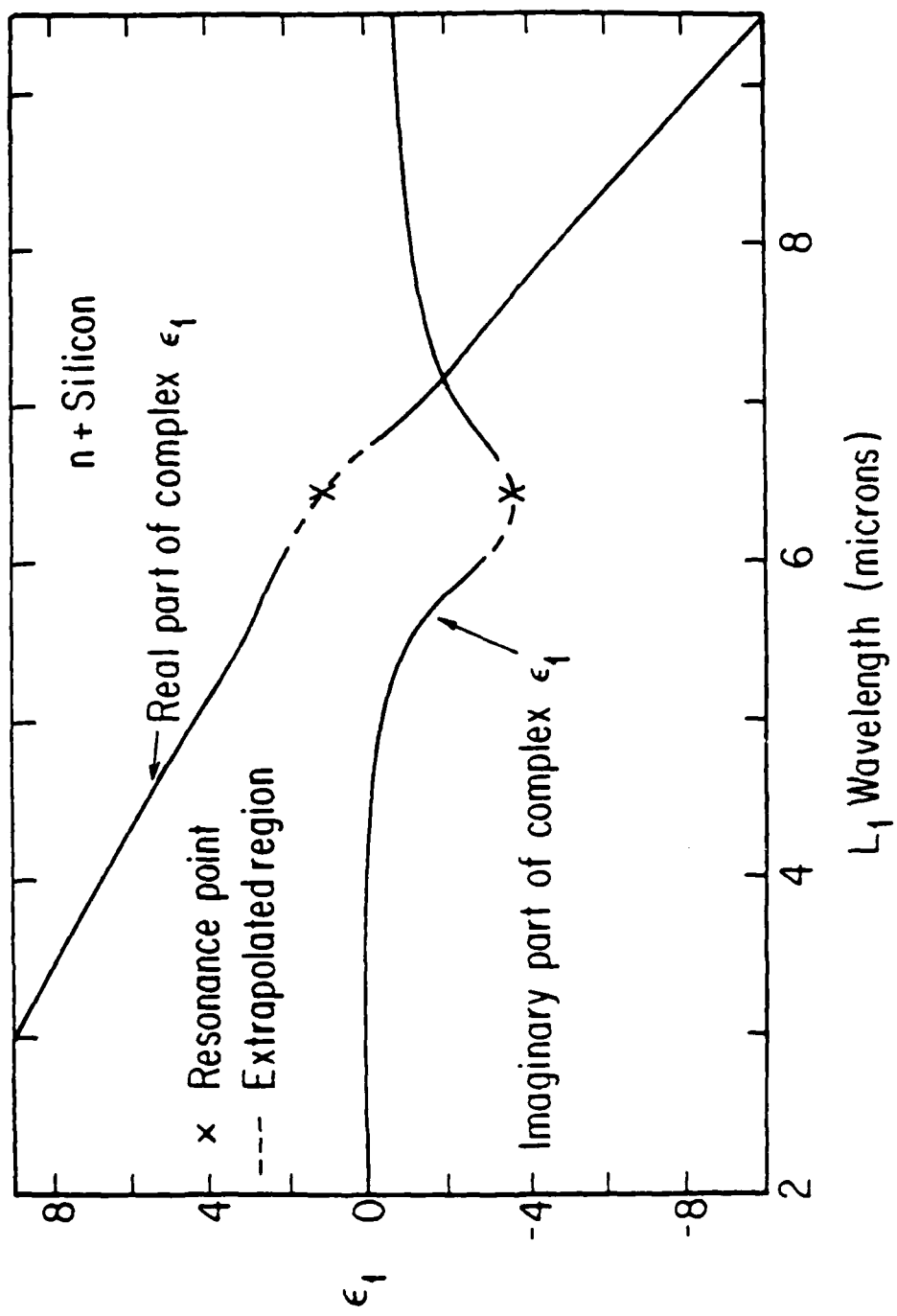
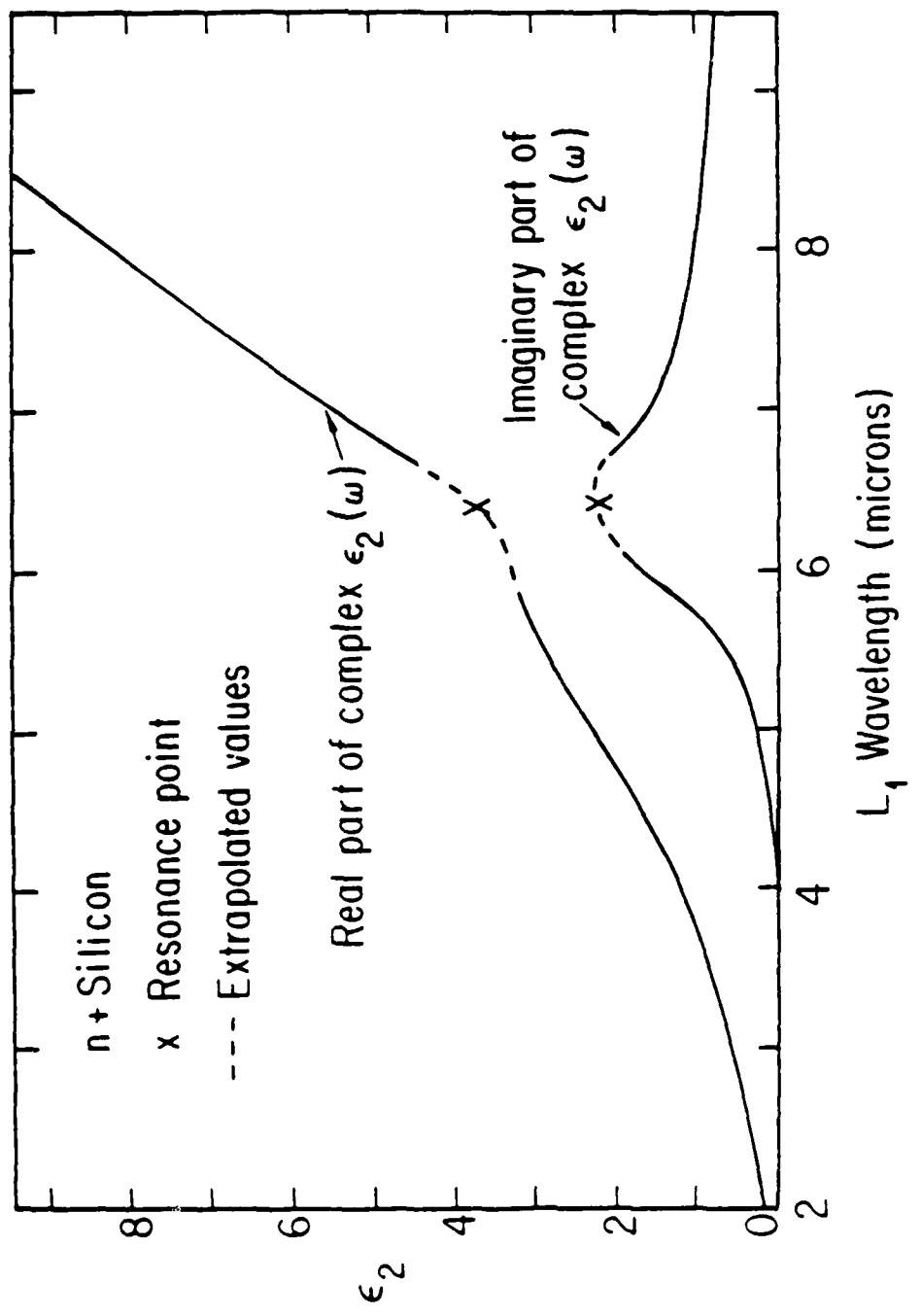


Fig. 7



Optical Measurements of the Surface Plasmon of Copper<sup>\*</sup>

P. F. Robusto<sup>†</sup> and R. Braunstein<sup>‡</sup>

Department of Physics, University of California, Los Angeles, California 90024

The optical properties of the noble metal copper were determined by computer fitting the experimentally obtained attenuated total internal reflection (ATR) spectra of its surface plasmon in the visible spectral region (0.42  $\mu$  to 0.63  $\mu$ ). The dispersion curves of the surface plasmon resonance of copper were determined; they show that the resonance exists on the steep absorption edge of  $\epsilon_2$  at 2.16 eV. This absorption edge, which is due to the d-band to Fermi level transition, causes the large shift in the location of the surface plasmon excitation from  $\epsilon_1(\omega_s) = -1$  to  $\epsilon_1(\omega_s) = -4.7$  and causes the true resonance to occur in the complex frequency plane.

Optische Messungen des Oberflächen-Plasmons von Kupfer\*

P.F. Robusto<sup>†</sup> und R. Braunstein<sup>‡</sup>

Physik-Abteilung, University of California, Los Angeles, California 90024

Die optischen Eigenschaften des Edelmetalls Kupfer wurden festgelegt, indem die experimentell erhaltenen, abgeschwächten inneren Totalreflexions-Spektra (ATR, abgeschwächte Totalreflexion) dessen Oberflächen-Plasmons durch Computer in den sichtbaren Spektralbereich angepaßt (0,42  $\mu$  bis 0,63  $\mu$ ) wurden. Die Dispersionskurven der Oberflächen-Plasmonresonanz von Kupfer wurden bestimmt; sie zeigen, daß an der steilen Absorptionskante von  $\epsilon_2$  Resonanz bei 2,16 eV vorhanden ist. Diese Absorptionskante, die auf den Übergang vom d-Band zum Fermi-Niveau zurückzuführen ist, bewirkt die große Verschiebung in der Lage der Oberflächen-Plasmonanregung von  $\epsilon_1(\omega_s) = -1$  auf  $\epsilon_1(\omega_s) = -4,7$  und bewirkt, daß die echte Resonanz in der komplexen Frequenzebene auftritt.

## I. INTRODUCTION

The optical constants of copper have been measured since the time of Drude. Copper is known to exhibit interband transitions throughout the visible region of the spectrum starting with a d-band to Fermi level transition at  $\sim 2.1$  eV. However, copper is known not to exhibit a bulk plasma resonance. The general explanation of this is that due to the d-states the positive contribution of the bound part of the dielectric function  $\epsilon_1^b$  comes in a frequency region where the negative contribution of the free electron part of the dielectric function  $\epsilon_1^f$  is of too large a magnitude for  $\epsilon_1$  to reach zero. It is the aim of this study to determine the optical properties of copper using attenuated total internal reflection (ATR) techniques<sup>1,2</sup> and to determine if a surface plasmon resonance exists in the visible region.

Section II contains the experimental details of sample preparation and surface plasmon resonance measurements and analysis. In Section III we give the results of the optical measurements, namely the optical properties of copper and the dispersion of its surface plasmon. This study is concluded with a summary in Section IV.

## II. EXPERIMENT

### A. Sample Preparation

The copper films were prepared by thermal evaporation in a high vacuum deposition system. All films were prepared on the same day that the experimental measurements were performed, so as to reduce the effects of oxide forming on the surface. The deposition was done from an  $\text{Al}_2\text{O}_3$  coated evaporation boat with 99.999% pure copper. The evaporation was performed in a diffusion pumped liquid nitrogen trapped deposition system with the pressure prior to growth approximately  $2 \times 10^{-6}$  torr. The substrates were fused silica front surface mirror substrates (7.75 mm diameter  $\times$  4.00 mm) polished to better than 1/10 wave flatness at 0.5461  $\mu$  over the center 6 mm portion. The deposition rate was 150 Angstroms/minute and was monitored during evaporation with a Sloan Omni 11A rate and thickness monitor. The total thickness of the Cu films was 3000 Angstroms as measured by a Sloan Angstrometer<sup>TM</sup>. The prepared films had a bright metallic luster and visually appeared to be optically smooth and homogeneous.

### B. Experimental Measurements

The Otto ATR method<sup>1,2</sup> of exciting surface plasmons was used where the surface plasmon was for an air-Cu interface. The ATR measurements were performed by measuring the ratio of the intensities of p-polarized light ( $R_p$ ) to that of s-polarized light ( $R_s$ ) with the sample pressed against the base of the ATR prism and normalized to the reflectivity with the sample removed. The prism used for optical measurements was a (45.0° - 89.9° [apex] - 45.1°) light flint prism which was flat to greater than a tenth of a wave at 0.5461  $\mu$ . The air gap was obtained by using either evaporated spacers or natural dust particles. The uniformity of the air gap was adjusted by observing the

uniformity of the surface plasmon resonance of copper at angles greater than the critical angle of total internal reflection. Beautiful colors of red, green, and blue could be visually seen for p-polarized light depending on the viewing angle and the air gap thickness. These colors could be seen for the largest viewing angle possible, therefore indicating the wave-vector divergence of the resonance condition. At angles less than the critical angle, Newton interference colors were not visible due to the smallness of the air gap used ( $d \sim 1000 \text{ \AA}$ ). The reflection spectra were taken on a Perkin Elmer model 301 far infrared spectrometer modified to operate in the single beam mode in the visible with the addition of 1440 lines/mm grating, appropriate filters, and use of tungsten light source and E.M.I. photomultiplier no. 9592B. The data collection system consisted of locking in on the 13 cps chopped signal with a PAR model 124A Lock-In Amplifier. The data were digitized and punched on paper tape and a PDP 11/20 computer averaged the data and generated a plot of normalized reflectivity versus wavelength. A digital controller was used to sequence stepping motor changes for both polarizations and for stepping the wavelength drive through the visible spectrum.<sup>3</sup> All experimental data were obtained by fixing the angle of incidence of the input light and by varying its frequency; that is, the complex frequency behavior of the surface plasma resonance was analyzed.

#### C. Optical Constant Determination

The ATR experiments were performed with a constant air gap and incident angle; the reflectivity ratio ( $R_p/R_s$ ) was measured as a function of wavelength. All optical measurements were taken at room temperature and are plotted as normalized reflectivity ratio ( $R_p/R_s$ ) versus wavelength, as shown in Figs. 1 and 2.

To theoretical curve fit an experimental ATR curve the wavelength dependent optical constants  $n$  and  $k$  need to be determined along with the wavelength independent air gap  $i$ . For each ATR spectrum the wavelength

wavelength dependent normalized reflectivity ratio ( $R_p/R_s$ ) was measured giving us one set of values for two unknown wavelength dependent values ( $n$  and  $k$ ) and wavelength independent value of  $d$ . Consequently, it is impossible to determine the optical constants and the air gap directly from the experimentally obtained data. The method that was chosen was to use the experimentally determined optical constant  $k$  obtained in the spectral region of  $0.44 \mu$  to  $0.55 \mu$  by L. G. Schultz.<sup>4</sup> He obtained accurate values of  $k$  from normal incidence transmission measurements, which is more sensitive for determining  $k$  values than reflectance measurements. The spectral region of  $0.44 \mu$  to  $0.55 \mu$  was chosen for two reasons, the first being that the relative change of  $k$  is nearly flat on the low energy side and slopes off slightly on the high energy side; the second being that this region is at higher energy than the surface plasmon minimum and therefore will have a small effect on the optical constants determined in this region.

The optical constants in the  $0.44 \mu$  to  $0.55 \mu$  region were determined by using Schultz's<sup>4</sup>  $k$  values and the experimentally obtained  $R_p/R_s$  values for two experimental curves. The procedure used was to pick an arbitrary air value  $d_1$  for experimental curve 1 and then to calculate from the  $R_p/R_s$  values and  $k$  values a set of  $n$  values. With this set of  $n$  and  $k$  values, curve 1 was computed and compared to the experimental curve. The air gap for the second curve  $d_2$  was varied until an optimum fit was obtained. This procedure was performed several times by varying the air gap  $d_1$  until the best fit for curve 1 was obtained. The  $k$  values of Schultz<sup>4</sup> were accurate to  $\pm 1\%$  and therefore they were varied within this range to optimize the fit. Once this procedure was completed, a set of  $n$  and  $k$  values was determined for the spectral range  $0.44 \mu$  to  $0.55 \mu$ , and the best fit air gaps  $d_1$  and  $d_2$  were determined. The final stepping interval for  $d$  was  $\pm 5$  Angstroms whereas the  $n$  values were determined to 0.0002 for each curve. Once the air gaps  $d_1$  and  $d_2$  were determined,

the experimental reflectance data could be used directly to obtain both  $n$  and  $k$  in the surface plasmon region. The procedure for this region was to pick a  $k$  value and to find the set of  $n$  values which would fit the experimental curves. The constraint used in this part of the spectral range was that the  $k$  values should vary smoothly in this interval and that the error be displayed in the  $n$  values. The reason for this will be explained in the results section. Computer programs<sup>3</sup> were written using the Fresnel reflection coefficients and the three medium multilayer reflectance formula to theoretically computer fit the experimental data. The computer fits are shown by x's on the same graphs as the reflectivity data in Figs. 1 and 2.

### III. RESULTS OF THE OPTICAL MEASUREMENTS OF THE SURFACE PLASMON OF COPPER

#### A. Optical Properties

The ATR determined optical constants  $n$  and  $k$  are shown in Figs. 3 and 4, while the dielectric functions  $\epsilon_1(\omega)$  and  $\epsilon_2(\omega)$  are shown in Figs. 5 and 6 along with the calculated normal incidence reflectivity in Fig. 7. The error in determining the optical constants is difficult to estimate. The average percentage error in the determined index of refraction as shown in Fig. 3 was 1.38%. The average experimental error was  $\leq 1\%$  which gives an error of  $\sim \pm 2\%$  for the index of refraction values, while an error of 2% in the  $k$  values yields an  $\sim 3.5\%$  error in  $n$ . Combining all the error producing terms yields an approximate error of 8% for the  $n$  values and 4% for the  $k$  values. The determined optical constants are quite adequate for determining the optical properties of the surface plasmon dispersion which is the main purpose of this investigation. By evaluating the imaginary part of the dielectric function  $\epsilon_2$ , we obtain a strong absorption edge at 2.15 eV which is attributed to the d-band to Fermi surface transitions  $L_5 \rightarrow L_1 (E_F)$  and  $L_3(Q+) \rightarrow E_F(L_2)$ ; the band nomenclature is due to Mueller and Phillips.<sup>5</sup> The rapid rise in  $\epsilon_2$  is due to the flatness of the  $L_3$  d-band, which permits a large number of interband transitions to the Fermi surface within a narrow energy range. The first peak in  $\epsilon_2$  is seen at  $\sim 2.48$  eV and corresponds to the transition  $L_3(Q-) \rightarrow E_F(L_2^1)$ . These values agree well with those obtained by Welkowsky and Braunstein<sup>6</sup> which were 2.18 eV and 2.53 eV.

#### B. Dispersion Analysis

The experimental dispersion of the surface plasmon resonance can be seen by noting the shift of the minimum for two different incidence angles in Figs. 1 and 2. The ATR experimental minima must be corrected for the

effects of the prism. These effects are essentially eliminated by using only the minima obtained when the minimum reflectivity for p-polarized light is greater than  $\sim 90\%$ . The dispersion curve for the ATR analysis is accomplished by plotting the value of the energy at the minimum of each ATR curve obtained for different incident angles (different wavevectors  $k_{||}$ ) for continuous changes in the frequency of the incident light. The ATR computed<sup>3</sup> dispersion curve is shown in Fig. 8 where the error bars signify that minima were determined within  $\pm 10$  Angstroms at low values of wavevector and  $\pm 1$  Angstrom at high wavevector points. The dispersion curve shows the characteristic surface plasmon resonance, that is,  $k_{||} \rightarrow \infty$  at  $\omega = \omega_s$ . The computed and experimental ATR spectra had less than 10% absorption for s-polarized light as expected theoretically. The resonance value for the plotted wave vectors is at 2.163 eV. The energy wavevector light line generated by the prism for the experimental runs of Figs. 1 and 2 are shown on the dispersion curve plot in Fig. 8.

The experimental ATR minima shown in Figs. 1 and 2 occur at lower energy due to the prism and the large amount of overcoupling ( $\sim 75\%$  absorption of incident light); the minimum is partly governed by the resonance condition  $\epsilon_1(\omega) = -n_p^2$  which causes the resonance to shift to a frequency where  $\epsilon_1(\omega)$  is more negative. The location of the surface plasmon resonance is shown in the plots of the optical constants  $n$  and  $k$  in Figs. 3 and 4 and on the dielectric function plots of  $\epsilon_1$  and  $\epsilon_2$  in Figs. 5 and 6. In the region of the surface plasmon resonance, the error bars for determining the index of refraction is large, as shown in Fig. 3. This error is mainly due to the effects of very thin oxide layers on the copper surface which cause the resonance condition to shift. This is the reason why the arbitrary criteria of fixing the values of  $k$  to lie on a smooth curve was chosen as explained in the previous section for determining the optical constants. As seen from Fig. 5, the surface plasmon

resonance occurs at  $\epsilon_1(\omega) = -4.7$  which is a large deviation from the normal condition  $\epsilon_1(\omega) = -1$ . This deviation is due to the relatively large value of  $\epsilon_2(\omega) = 4.4$  which causes the resonance to be damped and the true resonance to occur in the complex frequency plane at  $\epsilon(\omega=\omega_s) = -1$ . It should also be noticed that the resonance occurs on the steep absorption edge of the d-band to Fermi level transitions.

Shown in Fig. 7 is the location of the surface plasmon resonance ( $\epsilon_s$ ) on the normal incidence reflectivity curve. This resonance should be barely visible in high resolution normal incidence reflectivity spectra on copper which has a rough surface. The rough surface acts as a grating coupler and permits coupling between the incident transverse light and longitudinal surface plasmon resonance.<sup>7</sup>

Steel<sup>8</sup> has done a study on the characteristics of the energy loss function (L) for Au and Ag. He used a Drude-Lorentz model for characterizing the dielectric functions of Au and Ag and varied the free electron plasma frequency and relaxation time and studied their relationship to peaks in the energy loss function. He determined that "the presence of the absorption band causes the structure in (L) to change from the single free-electron peak to two peaks: a comparatively weak low-energy peak (LEP) below the absorption band and also a strong high-energy peak (HEP) above  $\omega_{po}$ "; where  $\omega_{po}$  is the bulk plasma frequency. The surface plasmon resonance of copper as obtained in this study is equivalent to the surface plasmon resonance associated with the (LEP) as discussed by Steel<sup>3</sup>: but there is no peak in the energy loss function at these low energies where the energy loss function for the surface plasmon resonance is defined at  $L = -\text{Im}[1/(\epsilon-1)]$ . The probable reason for this is that the damping is larger in Cu than it is for both Ag and Au and that the resonance is truly a function of complex frequency. It can be easily seen that the location of the surface plasmon resonance in Fig. 7 is in the region of the

steep drop in normal incidence reflectivity. This reflectivity drop is normally attributed to copper's interband transition but from this study we can see that reflectivity drop may also be partially caused by the normal decrease in reflectivity as the frequency  $\omega$  goes through the surface plasmon frequency and approaches the bulk plasmon frequency. The existence of the bulk plasma frequency is still questionable and, if it exists, it will occur in the complex frequency plane.

It was of interest to see if back-bending of the complex  $k$  dispersion curve occurred. The results of the analysis are shown in Fig. 9 where the real part of the complex wavevector ( $k_1$ ) is plotted versus energy. The plot of the complex- $\omega$  behavior is also shown. It can be seen that the back-bending of the complex  $k$  dispersion curve occurs when the complex- $\omega$  curve diverges, therefore having the desired characteristics of the surface plasmon resonance.

IV. SUMMARY

Experimental results show that the surface plasmon resonance of copper exists in the visible spectral region at 2.163 eV. The optical properties of copper have been experimentally determined by ATR methods and used to calculate the complex frequency dispersion curve which shows the characteristic wavevector divergence of the surface plasmon resonance, while the complex  $k$  dispersion curve exhibits the characteristic back-bending. The location of the resonance is on the steep absorption edges of  $\epsilon_2$  which is due to the d-band to Fermi level transitions. These transitions cause the large shift in the location of the real frequency excitations and for the true resonance to occur in the complex frequency plane. The color of the noble metal of copper may be partially attributed to the steep decrease in reflectivity which is caused by the normal decrease in reflectivity as the excitation frequency  $\omega$  goes through the surface plasmon frequency and approaches the bulk plasmon frequency and to copper's numerous interband transitions. The existence of the bulk plasma frequency is still questionable and if it exists it will occur in the complex frequency plane.

References

- \* Based in part upon a dissertation submitted by P. F. Robusto to the University of California at Los Angeles in partial fulfillment of the requirements for the degree of Ph.D. in Physics.
- Work performed with a Howard Hughes Doctoral Fellowship. Present address: Hughes Aircraft Co., 6155 El Camino Real, Carlsbad, Calif. 92008.
- ± Work supported in part by U. S. Army Research Office, Durham, North Carolina, and by the Air Force Office of Scientific Research.
- 1. A. Otto, Z. Physik 219, 227 (1969).
- 2. A. Otto, Z. Physik 216, 398 (1968).
- 3. P. F. Robusto, Ph.D. thesis (UCLA, 1978).
- 4. L. G. Schultz, J. Opt. Soc. Am. 44, 5, 357 (1954).
- 5. F. M. Mueller and J. C. Phillips, Phys. Rev. 157, 600 (1967).
- 6. M. Weikowsky and R. Braunstein, Sol. State Comm. 1, 1139 (1971).
- 7. N. Marschall, B. Fischer, and H. J. Queisser, Phys. Rev. Lett. 27, 95 (1971).
- 8. M. R. Steel, J. Opt. Soc. Am. 63, 1, 69 (1973).

Figure Captions

Fig. 1. Attenuated total internal reflection spectrum of copper plotted as the normalized value of the reflectivity ratio ( $R_p/R_s$ ) versus wavelength. Solid points denote the experimental data with a solid line drawn through them for clarity. The x's are the computer fitted values. Shown in the lower left is the best fit air gap value (d) and the angle of incidence of the incoming light with respect to the input side of the prism as shown in the ATR diagram in the insert.

Fig. 2. Attenuated total internal reflection spectrum of copper plotted as the normalized value of the reflectivity ratio ( $R_p/R_s$ ) versus wavelength. Solid points denote the experimental data with a solid line drawn through them for clarity. The x's are the computer fitted values. Shown in the lower left is the best fit air gap value (i) and the angle of incidence of the incoming light with respect to the input side of the prism as shown in the ATR diagram in the insert.

Fig. 3. Plot of the real part of the refractive index of copper versus wavelength for the computer fitted data of Figs. 1 and 2. Also shown is the location of the surface plasmon resonance ( $\lambda_s$ ).

Fig. 4. Plot of the imaginary part of the refractive index of copper versus wavelength for the computer fitted data of Figs. 1 and 2. Also shown is the location of the surface plasmon resonance ( $\lambda_s$ ).

Fig. 5. Plot of the real part of the dielectric function of copper versus wavelength for the computer fitted data of Figs. 1 and 2. Also shown is the location of the surface plasmon resonance ( $\lambda_s$ ).

Fig. 6. Plot of the imaginary part of the dielectric function of copper versus wavelength for the computer fitted data of Figs. 1 and 2. Also shown is the location of the surface plasmon resonance ( $\lambda_s$ ).

Fig. 7. Plot of the calculated normal incidence reflectivity of copper using the average optical constants obtained from the computer fitting of Figs. 1 and 2. Also shown is the location of its surface plasmon resonance ( $\lambda_s$ ) on the steep reflectivity edge.

Fig. 8. Dispersion curve of the surface plasmon of copper (solid line) for wavevector  $k_{\perp}$ . Range bars indicate that the minima were determined within  $\pm 10$  Å for low wavevector and  $\pm 1$  Å for high values of wavevector. Also shown is the energy-wavevector light line generated by the prism for the experimental spectra of Figs. 1 and 2 where the low wavevector line corresponds to Fig. 1 and the high wavevector line to Fig. 2. The angle (AO) is with respect to normal to the prism base.

Fig. 9. Complex- $\omega$  and complex- $k$  dispersion curves of the surface plasmon of copper along with a plot of the energy-wavevector relation for light in air.

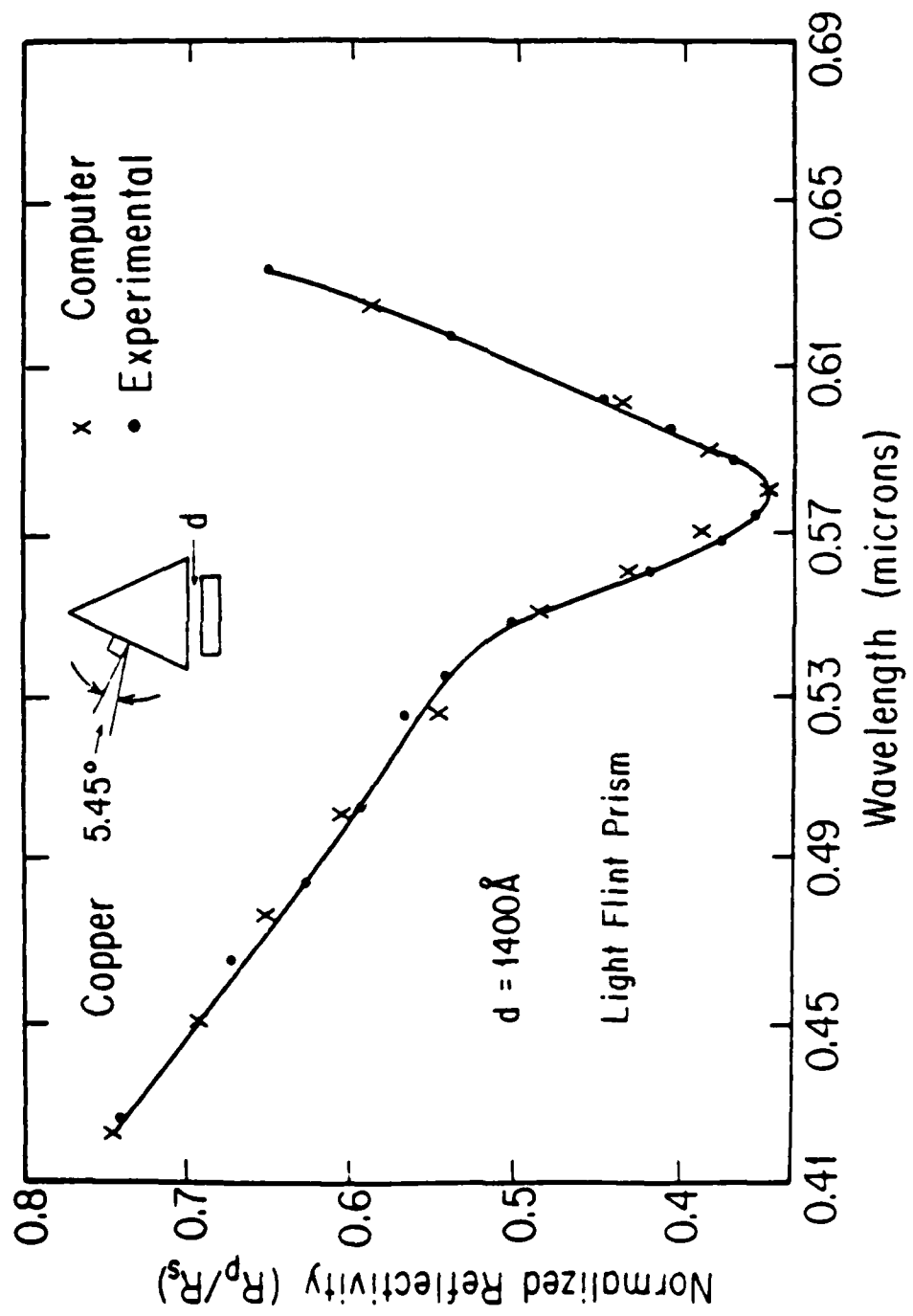


Fig. 1

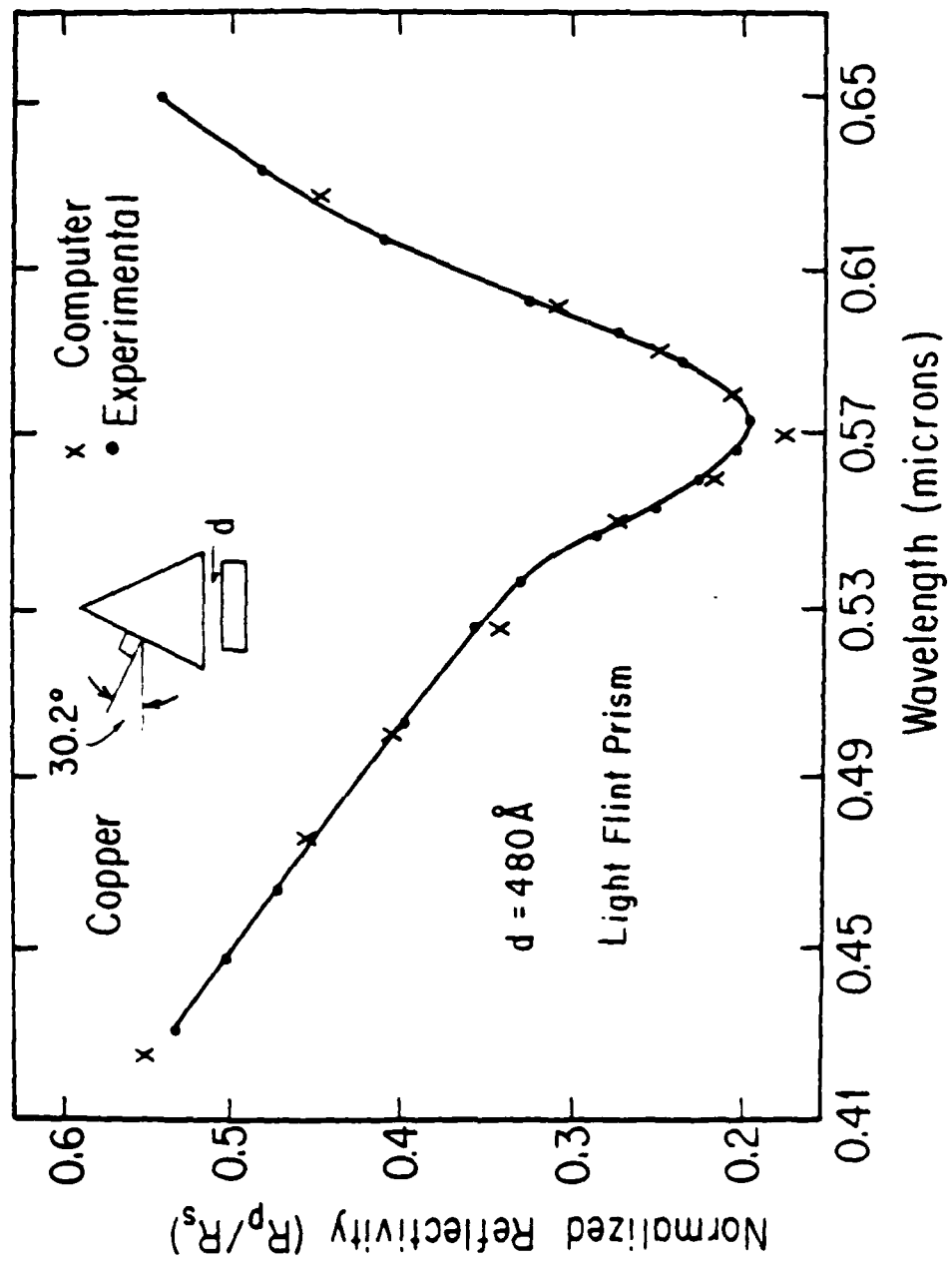


Fig. 2

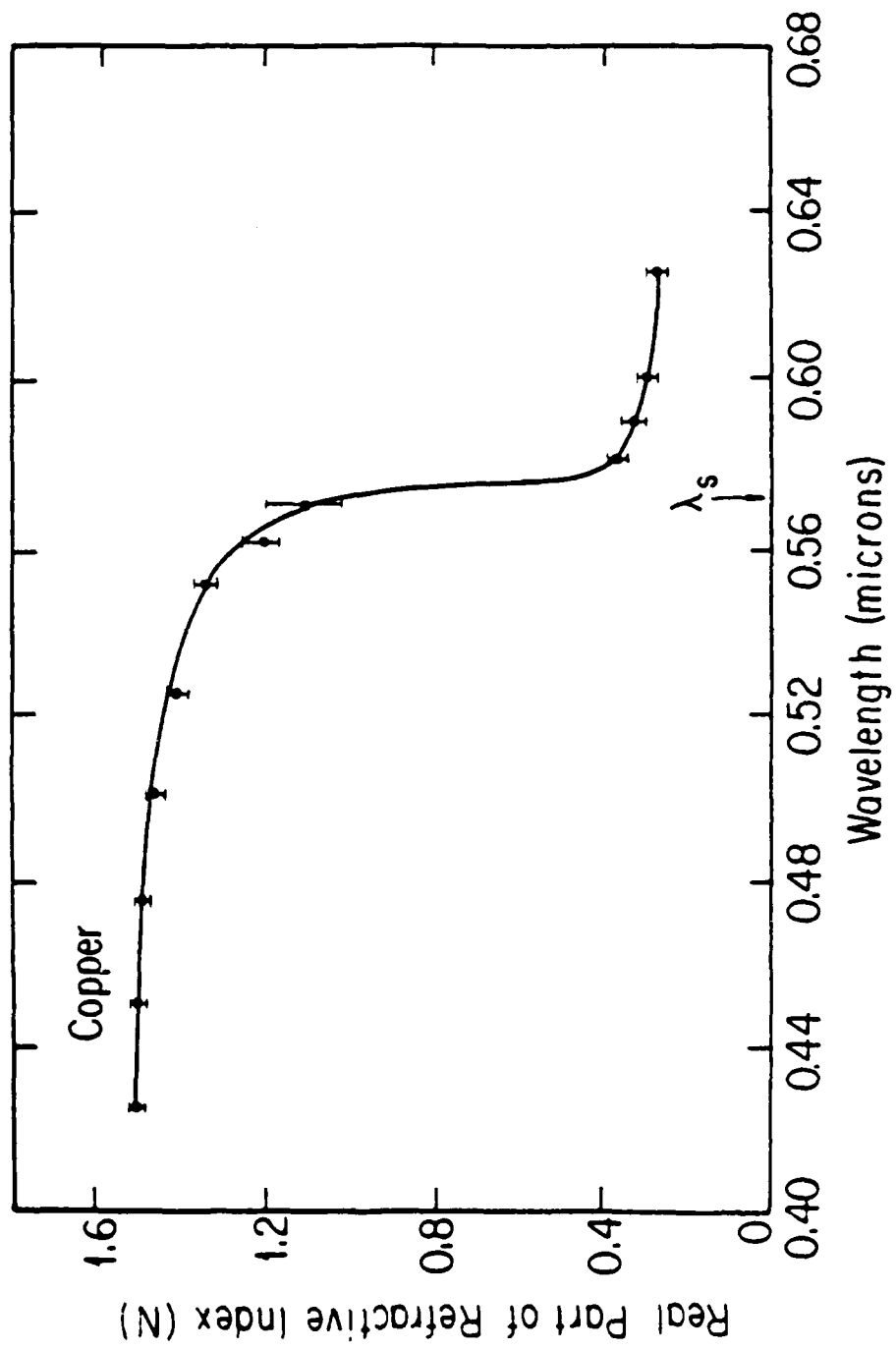


Fig. 3

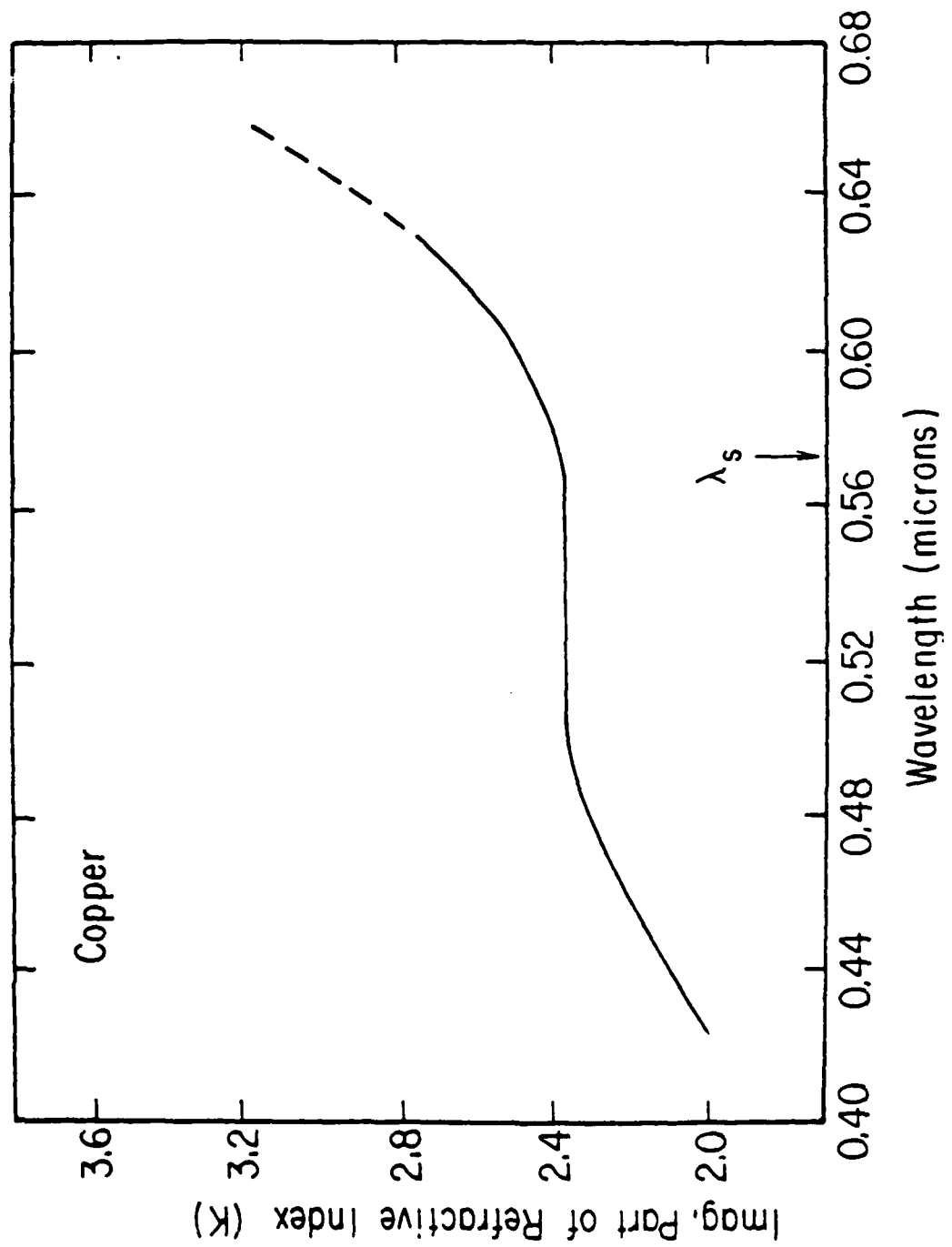


Fig. 4

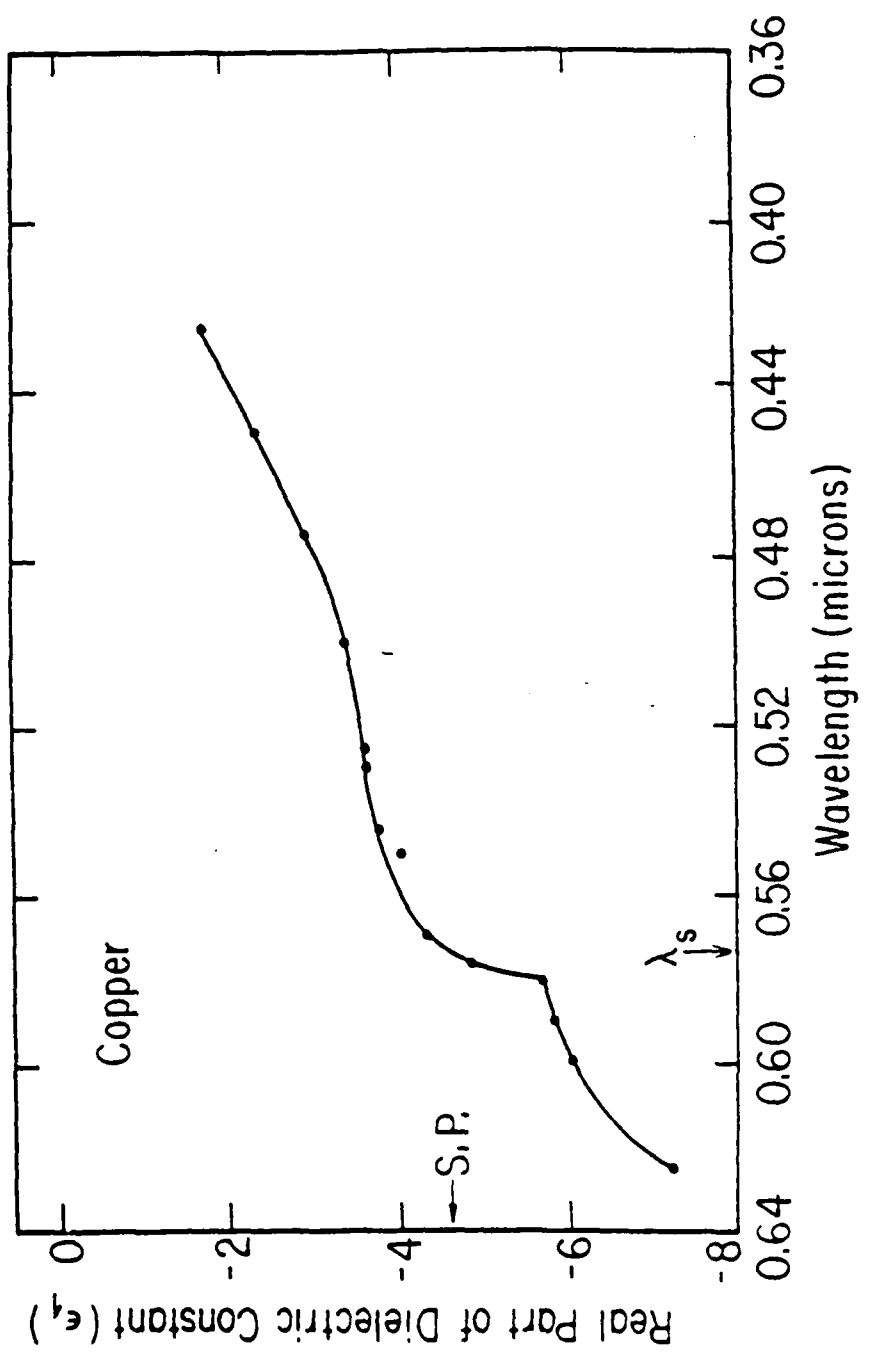


Fig. 5

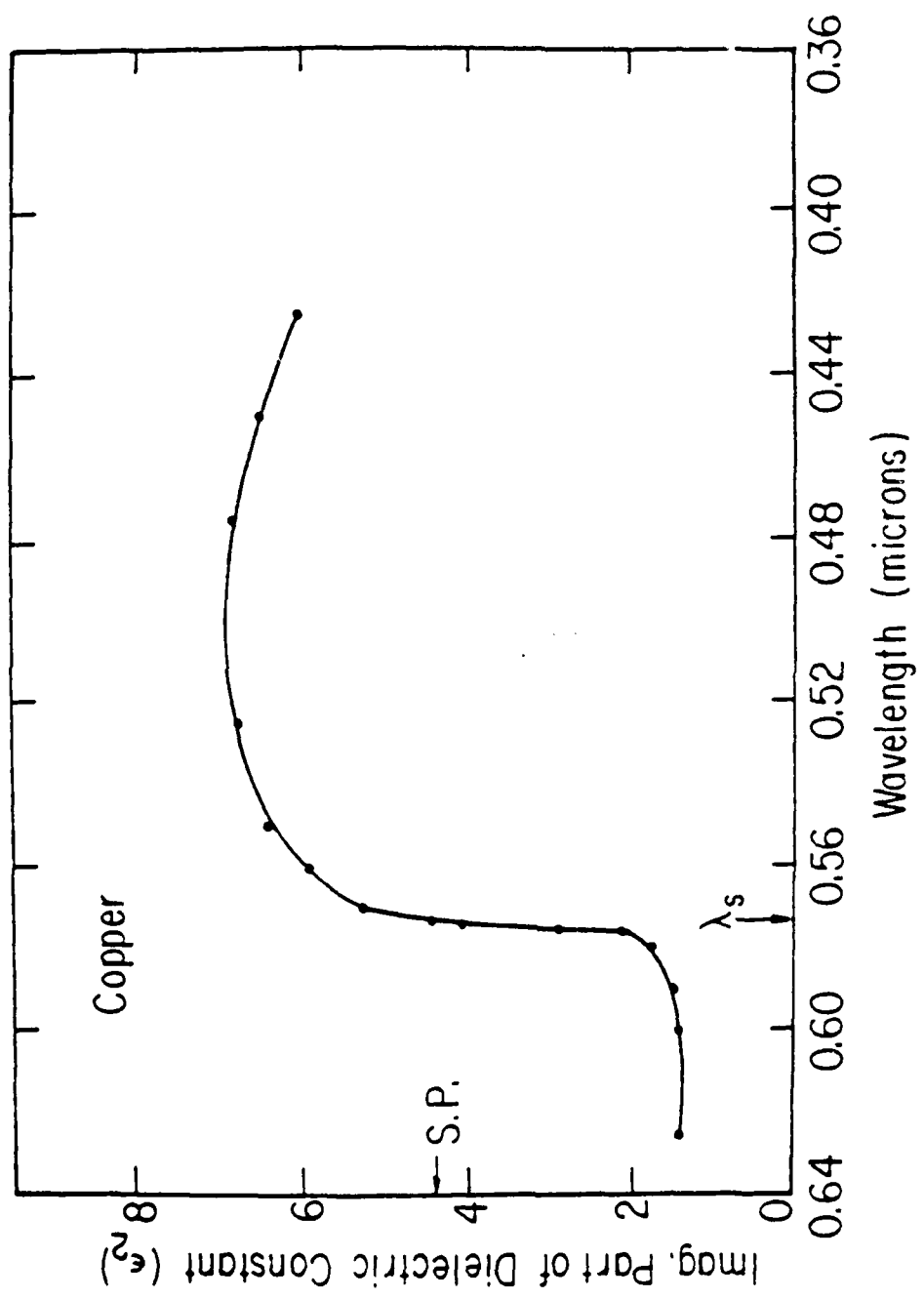


Fig. 5

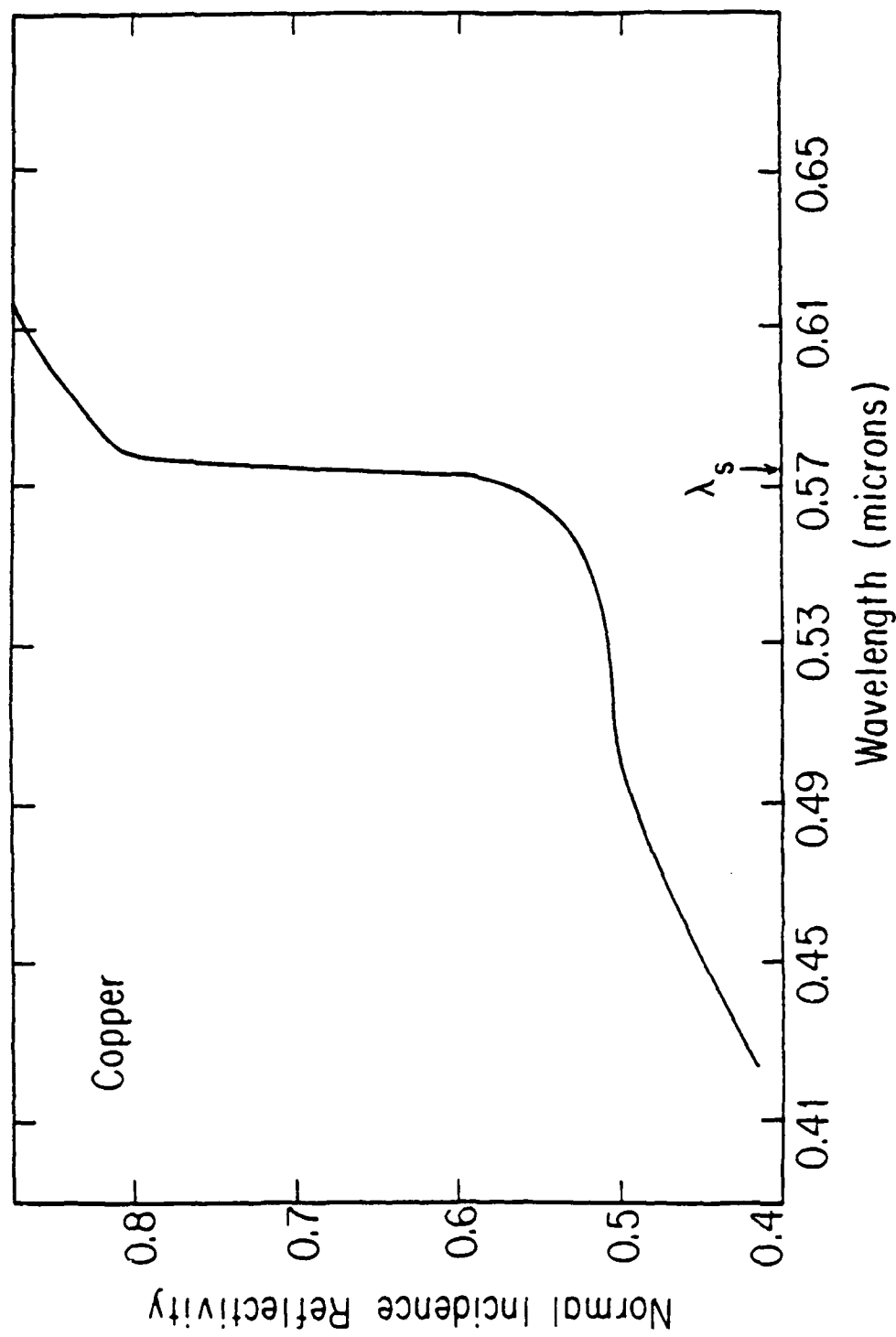


Fig. 7

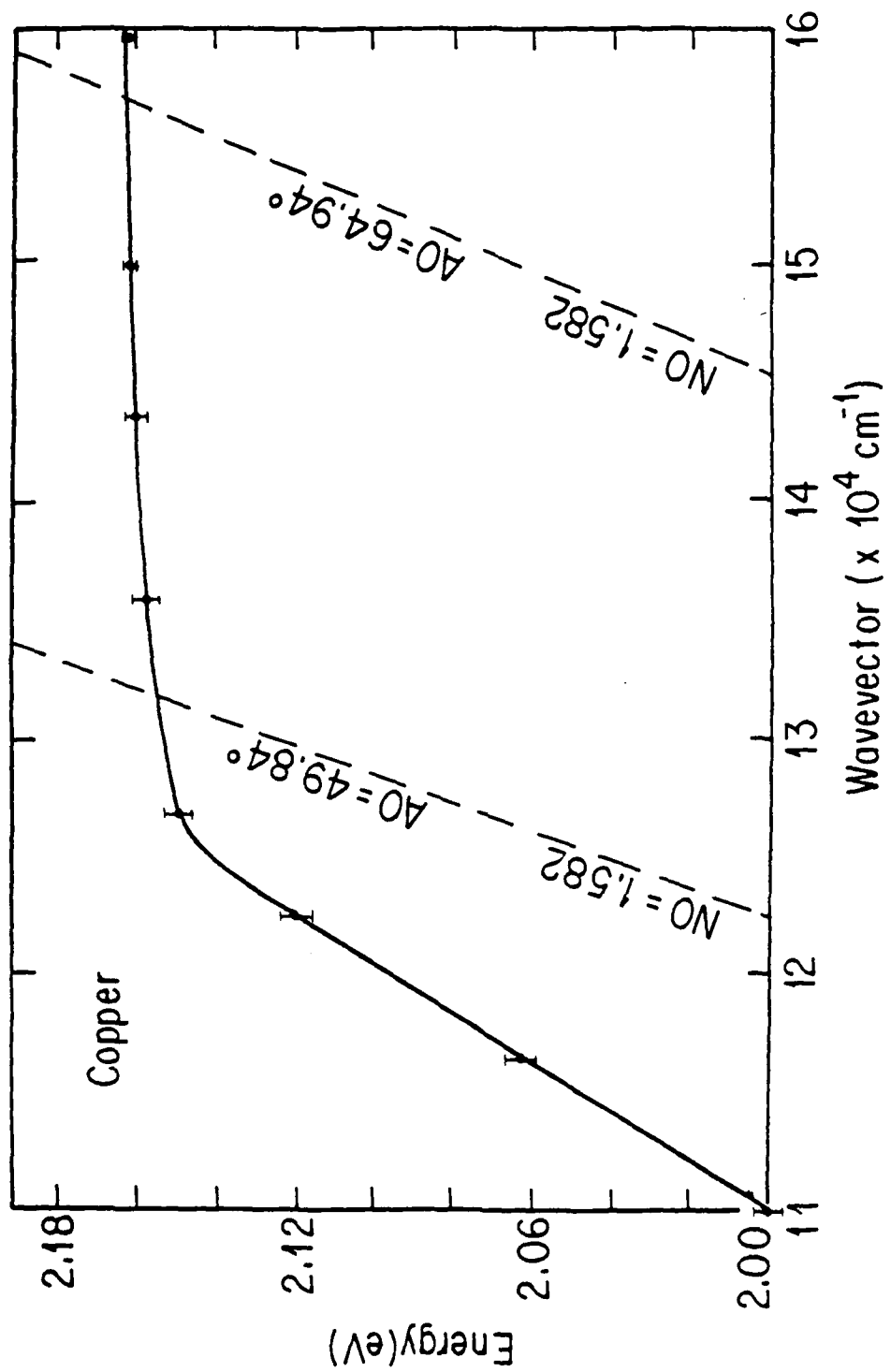


Fig. 3

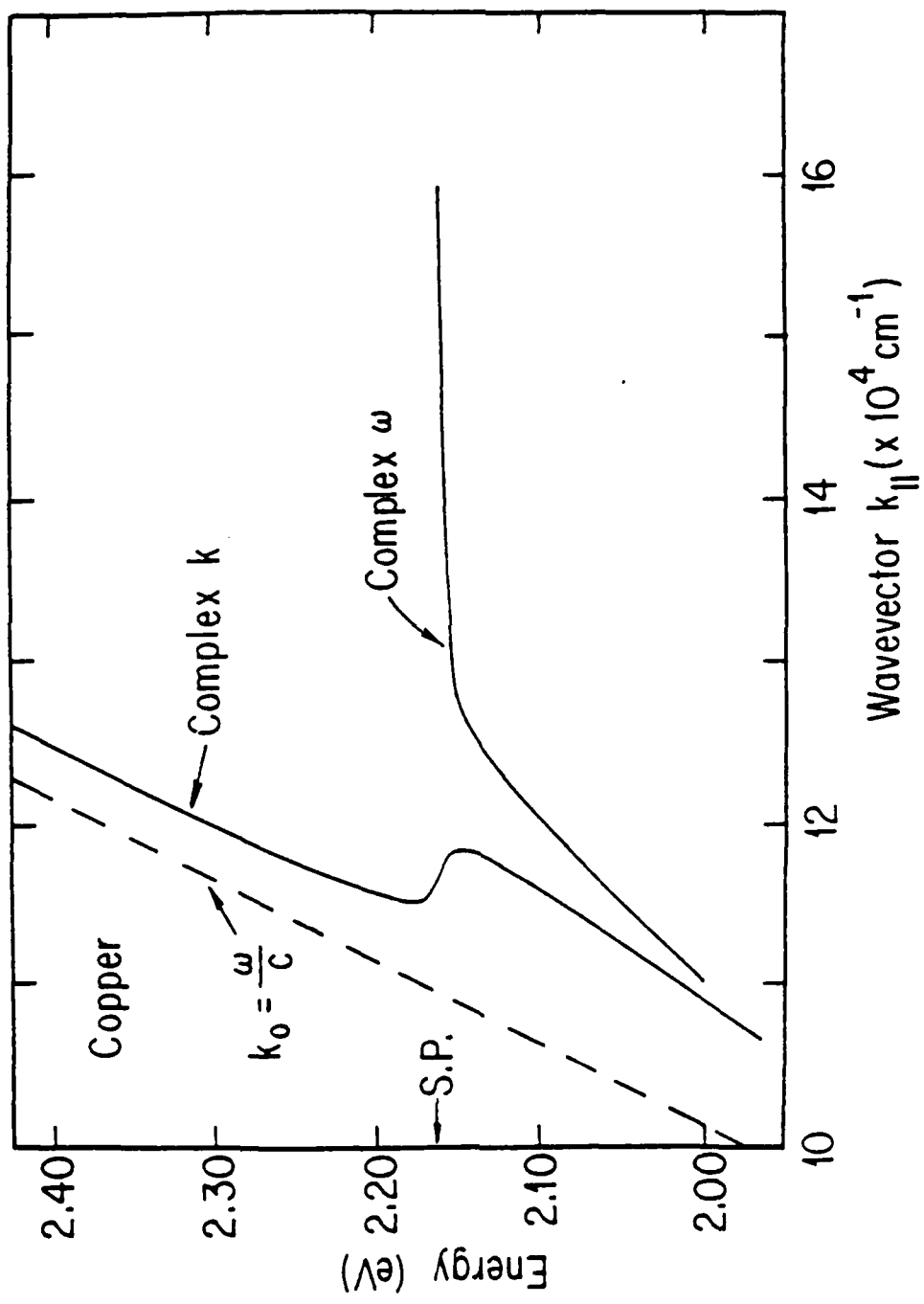


Fig. 9

